



NAVAL POSTGRADUATE SCHOOL

MONTEREY, CALIFORNIA

THESIS

**A SMART CLIMATOLOGY OF EVAPORATION DUCT
HEIGHT AND SURFACE RADAR PROPAGATION IN THE
INDIAN OCEAN**

by

Katherine L. Twigg

September 2007

Thesis Advisor:

J. T. Murphree

Thesis Co-Advisor:

P. A. Frederickson

Approved for public release; distribution is unlimited

THIS PAGE INTENTIONALLY LEFT BLANK

REPORT DOCUMENTATION PAGE			Form Approved OMB No. 0704-0188	
Public reporting burden for this collection of information is estimated to average 1 hour per response, including the time for reviewing instruction, searching existing data sources, gathering and maintaining the data needed, and completing and reviewing the collection of information. Send comments regarding this burden estimate or any other aspect of this collection of information, including suggestions for reducing this burden, to Washington headquarters Services, Directorate for Information Operations and Reports, 1215 Jefferson Davis Highway, Suite 1204, Arlington, VA 22202-4302, and to the Office of Management and Budget, Paperwork Reduction Project (0704-0188) Washington DC 20503.				
1. AGENCY USE ONLY (Leave blank)		2. REPORT DATE September 2007	3. REPORT TYPE AND DATES COVERED Master's Thesis	
4. TITLE AND SUBTITLE A Smart Climatology of Evaporation Duct Height and Surface Radar Propagation in the Indian Ocean			5. FUNDING NUMBERS	
6. AUTHOR(S) Katherine L. Twigg				
7. PERFORMING ORGANIZATION NAME(S) AND ADDRESS(ES) Naval Postgraduate School Monterey, CA 93943-5000			8. PERFORMING ORGANIZATION REPORT NUMBER	
9. SPONSORING /MONITORING AGENCY NAME(S) AND ADDRESS(ES) N/A			10. SPONSORING/MONITORING AGENCY REPORT NUMBER	
11. SUPPLEMENTARY NOTES The views expressed in this thesis are those of the author and do not reflect the official policy or position of the Department of Defense or the U.S. Government.				
12a. DISTRIBUTION / AVAILABILITY STATEMENT Approved for public release; distribution is unlimited			12b. DISTRIBUTION CODE	
<p>13. ABSTRACT (maximum 200 words)</p> <p>Surface electromagnetic propagation over the ocean is highly sensitive to near-surface atmospheric variability, particularly the height of the evaporation duct. Seasonal variation in near-surface meteorological factors and sea surface temperatures impact the evaporation duct height (EDH). Present U.S. Navy EDH climatology is based on sparse ship observations over a relatively short time period and an outdated evaporation duct (ED) model. This EDH climatology does not utilize smart, or modern, climatology datasets or methods and provides only long term mean (LTM) values of EDH. We have used existing, civilian, dynamically balanced reanalysis data, for 1970 to 2006, and a state-of-the-art ED model, to produce a spatially and temporally refined EDH climatology for the Indian Ocean (IO) and nearby seas. Comparisons of the present U.S. Navy EDH climatology with our climatology show a number of differences. These differences, and the differences in the methods used to generate the two climatologies, indicate that the EDH climatology we have generated provides a more accurate depiction of EDH.</p> <p>The EDH climatology we have produced provides LTM EDH values. But the data and methods we used to create this climatology also allowed us to examine the impacts of climate variations on EDH. Climate variations can have major impacts on the upper ocean and overlying lower troposphere. These impacts can lead to major fluctuations in the factors that determine EDH, and can thereby alter the propagation of EM signals through the atmosphere. The IO and nearby seas are strongly affected by a number of climate variations (e.g., El Niño-La Niña (ENLN), Indian Ocean Zonal Mode (IOZM)). These climate variations are known to lead to large anomalies in sea surface temperature, air temperature, winds, humidity, and other variables in the IO; however, the associated impacts on EDH and EM propagation have not been identified. To assess these impacts, reanalysis data composited by season and climate variation were processed using: (1) the NPS ED model to assess the impacts of the climate variations on EDH; and (2) the Advanced Refraction Effects Prediction System (AREPS) to assess the impacts of the variations on radar propagation. Our results show significant variations in EDH and AREPS ranges associated with the climate variations that affect the IO and nearby regions. These climate variations are predictable on weekly and longer time scales. In addition, for several seasons, EDH is significantly correlated with the climate variation when EDH lags by zero, one, and two months. Thus, there appears to be potential for climate scale forecasting of EDH and radar propagation at weekly to monthly lead times.</p> <p>For areas of operational interest, we conducted correlation analyses of EDH with its associated factors to further our understanding of the processes that cause spatial and temporal variations of EDH. These correlation results provide insights into the spatial and temporal sensitivity of EDH to the factors. Thus, they provide guidance on how to focus research, development, and operational efforts aimed at improving analyses and forecasts of EDH.</p> <p>We used the EDH climatology created in this study to generate climatological sensor performance surfaces for radar propagation. These surfaces are maps of climatological surface radar propagation over the IO and nearby seas under different climatological conditions (e.g., different months, locations, climate variations, and regimes). The performance surfaces are prototypes of operational climatological products, and examples of the improved climatological products that can be developed using smart climatology data and methods.</p> <p>These results indicate that climatological support for military planners could be substantially improved by using a smart climatology approach (i.e., applying state-of-the-art climate datasets, analysis, and forecasting methods).</p>				
14. SUBJECT TERMS Climatology, Smart Climatology, Evaporation Duct Height, Radar Propagation, Radar Detection Range, Sensor Performance, Performance Surface, Indian Ocean, Climate Variations, El Nino, La Nina, Indian Ocean Zonal Mode, North Atlantic Oscillation, U.S. Navy, Royal Navy			15. NUMBER OF PAGES 159	
16. PRICE CODE				
17. SECURITY CLASSIFICATION OF REPORT Unclassified	18. SECURITY CLASSIFICATION OF THIS PAGE Unclassified	19. SECURITY CLASSIFICATION OF ABSTRACT Unclassified	20. LIMITATION OF ABSTRACT UU	

THIS PAGE INTENTIONALLY LEFT BLANK

Approved for public release; distribution is unlimited

**A SMART CLIMATOLOGY OF EVAPORATION DUCT HEIGHT AND
SURFACE RADAR PROPAGATION IN THE INDIAN OCEAN**

Katherine L. Twigg
Lieutenant, Royal Navy
MSci., University of Durham, 1997

Submitted in partial fulfillment of the
requirements for the degree of

MASTER OF SCIENCE IN METEOROLOGY

from the

**NAVAL POSTGRADUATE SCHOOL
September 2007**

Author: Katherine L. Twigg

Approved by: Dr. James T. Murphree
Thesis Advisor

Mr. Paul A. Frederickson
Co-Advisor

Dr. Philip A. Durkee
Chairman, Department of Meteorology

THIS PAGE INTENTIONALLY LEFT BLANK

ABSTRACT

Surface electromagnetic propagation over the ocean is highly sensitive to near-surface atmospheric variability, particularly the height of the evaporation duct. Seasonal variation in near-surface metrological factors and sea surface temperatures impact the evaporation duct height (EDH). Present U.S. Navy EDH climatology is based on sparse ship observations over a relatively short time period and an outdated evaporation duct (ED) model. This EDH climatology does not utilize smart, or modern, climatology datasets or methods and provides only long term mean (LTM) values of EDH. We have used existing, civilian, dynamically balanced reanalysis data, for 1970 to 2006, and a state-of-the-art ED model, to produce a spatially and temporally refined EDH climatology for the Indian Ocean (IO) and nearby seas. Comparisons of the present U.S. Navy EDH climatology with our climatology show a number of differences. These differences, and the differences in the methods used to generate the two climatologies, indicate that the EDH climatology we have generated provides a more accurate depiction of EDH.

The EDH climatology we have produced provides LTM EDH values. But the data and methods we used to create this climatology also allowed us to examine the impacts of climate variations on EDH. Climate variations can have major impacts on the upper ocean and overlying lower troposphere. These impacts can lead to major fluctuations in the factors that determine EDH, and can thereby alter the propagation of EM signals through the atmosphere. The IO and nearby seas are strongly affected by a number of climate variations (e.g., El Niño-La Niña (ENLN), Indian Ocean Zonal Mode (IOZM)). These climate variations are known to lead to large anomalies in sea surface temperature, air temperature, winds, humidity, and other variables in the IO; however, the associated impacts on EDH and EM propagation have not been identified. To assess these impacts, reanalysis data composited by season and climate variation were processed using: (1) the NPS ED model to assess the impacts of

the climate variations on EDH; and (2) the Advanced Refraction Effects Prediction System (AREPS) to assess the impacts of the variations on radar propagation. Our results show significant variations in EDH and AREPS ranges associated with the climate variations that affect the IO and nearby regions. These climate variations are predictable on weekly and longer time scales. In addition, for several seasons, EDH is significantly correlated with the climate variation when EDH lags by zero, one, and two months. Thus, there appears to be potential for climate scale forecasting of EDH and radar propagation at weekly to monthly lead times.

For areas of operational interest, we conducted correlation analyses of EDH with its associated factors to further our understanding of the processes that cause spatial and temporal variations of EDH. These correlation results provide insights into the spatial and temporal sensitivity of EDH to the factors. Thus, they provide guidance on how to focus research, development, and operational efforts aimed at improving analyses and forecasts of EDH.

We used the EDH climatology created in this study to generate climatological sensor performance surfaces for radar propagation. These surfaces are maps of climatological surface radar propagation over the IO and nearby seas under different climatological conditions (e.g., different months, locations, climate variations, and regimes). The performance surfaces are prototypes of operational climatological products, and examples of the improved climatological products that can be developed using smart climatology data and methods.

These results indicate that climatological support for military planners could be substantially improved by using a smart climatology approach (i.e., applying state-of-the-art climate datasets, analysis, and forecasting methods).

TABLE OF CONTENTS

I.	INTRODUCTION.....	1
	A. BACKGROUND	1
	B. EVAPORATION DUCT AND ELECTROMAGNETIC PROPAGATION.....	2
	1. Modified Refractivity and Ducting Layers	3
	2. The Effect of Atmospheric Factors on EDH	5
	3. EM Propagation and Detection Range	8
	C. SMART CLIMATOLOGY	10
	1. Concept	10
	2. Design of Study	12
	D. AREA OF STUDY: INDIAN OCEAN.....	13
	1. Long Term Mean of Climate and Seasonal Cycle in SW Asia	14
	E. LARGE SCALE CLIMATE VARIATIONS.....	17
	1. El Nino – La Nina	17
	2. Indian Ocean Zonal Mode	21
	3. North Atlantic Oscillation.....	24
	F. EXISTING EVAPORATION DUCT HEIGHT CLIMATE PRODUCTS.....	26
	G. MOTIVATION AND DESIGN OF THIS STUDY	28
II.	DATA AND METHODS.....	31
	A. DATA	31
	1. NCEP Reanalysis Dataset	31
	B. CLIMATE INDICES	34
	1. Multivariate ENSO Index (MEI).....	34
	2. Dipole Mode Index (DMI)	35
	3. North Atlantic Oscillation Index (NAOI)	36
	C. METHODS	36
	1. EDH Computation	36
	2. Understanding EDH and its Associated Factors	37
	3. Investigating the Effects of Climate Variations on EDH	38
	D. SUMMARY	39
III.	RESULTS	41
	A. EDH LTM	41
	1. Equatorial Region	44
	2. Arabian Sea	45
	3. Gulf of Aden	45
	4. Gulf of Oman and South Arabian Gulf	46
	B. LTM FACTORS.....	46
	1. LTM Factors which Affect EDH.....	46
	a. <i>Surface Wind</i>	46

	b.	Sea Surface Temperature.....	48
	c.	Surface Air Temperature and Air-Sea Temperature Difference	50
	d.	Relative Humidity.....	50
C.		INFLUENCE OF FACTORS ON EDH IN SPECIFIC AREAS.	54
	1.	Equatorial Region	54
	2.	Arabian Sea	58
	a.	Omani Coast Correlations.....	60
	3.	Gulf of Oman.....	62
	4.	South Arabian Gulf	65
	5.	Gulf of Aden	69
D.		AREPS CLIMATOLOGY AND BUOY COMPARISON	72
	1.	Comparison to Present U.S. Navy EDH Climatology	72
	2.	Comparison to Woods Hole Oceanographic Institute (WHOI) Buoy Data	75
E.		CLIMATE VARIATIONS OF THE FACTORS WHICH AFFECT EDH.....	78
	1.	Composite Analyses	83
	a.	DMI	83
	b.	Composite Analysis Results.....	84
	c.	Positive IOZM Composite Analysis Example	85
	2.	Extent of EDH Change due to Climate Variations.....	90
F.		CORRELATION TO CLIMATE VARIATION INDICES	92
G.		SENSOR PERFORMANCE IMPACTS	94
	1.	Introduction.....	94
	a.	Smart Climatology Environmental Assessment Surfaces.....	94
	b.	Vertical Coverage Diagrams	95
	2.	Smart Climatology Performance Surfaces	96
	a.	Surface Detection Range.....	96
	b.	Cut Off Frequency.....	99
	c.	Limitations.....	99
	d.	Summary.....	101
IV.		CONCLUSIONS AND RECOMMENDATIONS.....	103
	A.	SUMMARY	103
	B.	AREAS FOR FURTHER RESEARCH	105
		APPENDIX A.....	111
		APPENDIX B.....	115
		APPENDIX C.....	127
		LIST OF REFERENCES.....	129
		INITIAL DISTRIBUTION LIST	135

LIST OF FIGURES

Figure 1.	A vertical M profile for a surface duct and its associated height versus range ray trace plot of X-band waves emitted from an antenna at 25 m height propagating through an atmosphere with an EDH of 20 m (After: Frederickson et al., 2000).....	4
Figure 2.	Plots of modified refractivity (M) versus altitude: (a) sub-refractive layer denoted by dashed line; (b) normal refraction; (c) elevated duct denoted by dashed line; (d) surface duct denoted by dashed line; (e) surface-based duct denoted by dashed line, (due to an elevated layer with a strongly negative vertical M gradient); (f) ED denoted by dashed line. (From: Babin et al., 1997).....	4
Figure 3.	EDH computed by the NPS ED model versus ASTD for different relative humidity, as indicated. (From: Frederickson, 2007).	6
Figure 4.	EDH computed by the NPS ED model versus ASTD for different wind speed values, as indicated. (From: Frederickson, 2007).....	6
Figure 5.	Propagation loss versus range of C-band radar for a refractive profile with different EDH values. Dotted line indicates the propagation loss threshold. (After: Frederickson et al., 2004)	9
Figure 6.	Smart Climatology: Flow diagram of Development and Applications (After: Murphree, 2007a)	11
Figure 7.	The Indian Ocean region examined in our study and located within 35°N-15°S; 025°E-120°E. Abbreviations: GOO Gulf of Oman, GOA Gulf of Aden.	13
Figure 8.	Schematic illustration of the major lower atmospheric and upper oceanic circulation features during the January peak of the Asian winter monsoon. (From: Lutgens and Tarbuck (2001), available online from http://www.ux1.eiu.edu/~cfjps/1400/circulation.html). Accessed September 2007.	15
Figure 9.	Schematic illustration of the major lower atmospheric and upper oceanic circulation features during the July peak of the Asian summer monsoon. (From: Lutgens and Tarbuck (2001), available online from http://www.ux1.eiu.edu/~cfjps/1400/circulation.html). Accessed September 2007.	15
Figure 10.	A schematic representation of identified current branches during (a) January (northeast monsoon) and (b) July (southwest monsoon). (From: Sean Chamberlin and Dickey, 2007)	16

Figure 11.	Schematic representation of the equatorial zonal component of the Hadley-Walker circulation (HWC): a) long term mean (LTM) zonal equatorial HWC, b) anomalous zonal equatorial HWC during EN, and c) anomalous zonal equatorial HWC during LN. After: Peixoto and Oort (1992). Note the LTM zonal overturning circulations in the tropical Atlantic, African, IO, and Pacific regions. These are the Walker circulation components of the HWC. Note that the IO and Pacific Walker circulations are weakened (strengthened) during EN and LN events.	19
Figure 12.	Schematic of tropical Pacific atmosphere and ocean during a) normal, b) El Nino, and c) La Nina periods. (From: Pacific Marine Environmental Laboratory (PMEL), available online from http://www.pmel.noaa.gov/tao/elnino/nino-home.html# . Accessed September 2007).....	20
Figure 13.	Correlation of SST with El Nino-La Nina Index (using Multivariate El Nino Southern Oscillation Index) for October-November. Figure created using NCEP reanalysis data and CDC web site. (From: http://www.cdc.noaa.gov/Correlation/ , accessed September 2007). ..	20
Figure 14.	Schematic of the Rossby-Kelvin wave response to anomalous equatorial tropospheric (a) warming and (b) cooling. Contours show perturbation isobars. To the east of the forcing region, there is a ridge in (a) and a trough in (b) associated with the Kelvin wave response. To the west of the forcing region, there is a trough in (a) and a ridge in (b) associated with the Kelvin wave response. To the northwest and southwest of the forcing region, there are paired anticyclones in (a) and cyclones in (b) associated with the Rossby wave response. From: Ford (2000).	21
Figure 15.	Schematic diagrams of characteristic IOZM anomalies. SST anomalies (positive (negative SSTA in red (blue)) during (a) positive IOZM phase and (b) negative IOZM phase. White patches indicate anomalously strong convective activity. Anomalous wind directions are indicated by arrows. (From: http://www.jamstec.go.jp/frsgc/research/d1/iod/IOD1.html accessed September 2007).....	22
Figure 16.	Ocean-atmosphere feedbacks in the eastern Indian Ocean controlling the growth of the positive phase IOZM. (After: Meyers et al., 2007).....	23
Figure 17.	Schematic depiction of the NAO phases: (a) positive and (b) negative. (From: http://eesc.columbia.edu/NAO/ , accessed September 2007).....	25

Figure 18.	Distribution of 10x10 degree boxes (Marsden squares) for which long term mean climatological EDH values are available, one EDH value per square per month, from the existing EDH climatology used the U.S. Navy and Royal Navy. The dark blue (magenta) boxes indicate the locations for which values are (are not) available. The green box indicates the central Arabian Sea box for which the EDH values are shown in Figure 19. (From: AREPS, Space and Naval Warfare Systems Center: http://areps.spawar.navy.mil/ , accessed September 2007).	27
Figure 19.	Histogram of EDH versus percent occurrence for October in central Arabian Sea box indicated in Figure 18, an example of the existing EDH climatology. (From AREPS, Space and Naval Warfare Systems Center: http://areps.spawar.navy.mil/ , accessed September 2007).....	28
Figure 20.	Indian Ocean study area with an overlay of the NCEP Gaussian grid. Areas of interest for this study are shaded blue and existing climatology boxes are shaded yellow.	32
Figure 21.	Masking of land: EDH calculated only for blue shaded grid boxes.	37
Figure 22.	Seasonal LTM EDH(m) for the tropical and northern IO for: (a) November-December-January (NDJ); (b) February-March-April (FMA); (c) May-June-July (MJJ); and (d) August-September-October (ASO). Coastal values should be used with caution (see Chapter III, section A).....	42
Figure 23.	Seasonal LTM EDH(m) for the NW IO for: (a) NDJ; (b) FMA; (c) MJJ; and (d) ASO. Coastal values should be used with caution (see Chapter III, section A).....	43
Figure 24.	Mapping of sea grid points land-sea grid points. Compare to Figure 21. The blue arrows indicate the direction from which EDH values from seaward grid boxes are mapped to coastal sea areas containing both land and sea, and for which EDH is not directly calculated due to the influence of land (see Chapter II, section C1)...	44
Figure 25.	LTM wind speed (ms^{-1}) and direction for: (a) NDJ; (b) FMA; (c) MJJ; and (d) ASO.	47
Figure 26.	LTM SST ($^{\circ}\text{C}$) for: (a) NDJ; (b) FMA; (c) MJJ; and (d) ASO.	49
Figure 27.	LTM air temperature ($^{\circ}\text{C}$) for: (a) NDJ; (b) FMA; (c) MJJ; and (d) ASO.....	51
Figure 28.	LTM ASTD ($^{\circ}\text{C}$) for: (a) NDJ; (b) FMA; (c) MJJ; and (d) ASO	52
Figure 29.	LTM RH (%) for: (a) NDJ; (b) FMA (c) MJJ; and (d) ASO.....	53

Figure 30.	Seasonal cycle of monthly LTM EDH and EDH factor values (panels a-e) and correlations of EDH with EDH factors (panel f) for Diego Garcia region (see Figure 20). (a) EDH and EDH standard deviation; (b) wind speed, u and v components of wind; (c) SST and Ta; (d) ASTD; (e) RH; (f) zero lag correlation for each month of EDH (panel a) with each of the factors (panels b-e), with the color of the correlation curves indicating the factor for which the correlation was calculated (see color code).....	56
Figure 31.	Seasonal cycle of monthly LTM EDH and EDH factor values (panels a-e) and correlations of EDH with EDH factors (panel f) for Omani coast region (see Figure 20). (a) EDH and EDH standard deviation; (b) wind speed, u and v components of wind; (c) SST and Ta; (d) ASTD; (e) RH; (f) zero lag correlation for each month of EDH (panel a) with each of the factors (panels b-e), with the color of the correlation curves indicating the factor for which the correlation was calculated (see color code).....	59
Figure 32.	Seasonal cycle of monthly LTM EDH and EDH factor values (panels a-e) and correlations of EDH with EDH factors (panel f) for the Gulf of Oman (see Figure 20). (a) EDH and EDH standard deviation; (b) wind speed, u and v components of wind; (c) SST and Ta; (d) ASTD; (e) RH; (f) zero lag correlation for each month of EDH (panel a) with each of the factors (panels b-e), with the color of the correlation curves indicating the factor for which the correlation was calculated (see color code).....	64
Figure 33.	Seasonal cycle of monthly LTM EDH and EDH factor values (panels a-e) and correlations of EDH with EDH factors (panel f) for the Southern Arabian Gulf (see Figure 20). (a) EDH and EDH standard deviation; (b) wind speed, u and v components of wind; (c) SST and Ta; (d) ASTD; (e) RH; (f) zero lag correlation for each month of EDH (panel a) with each of the factors (panels b-e), with the color of the correlation curves indicating the factor for which the correlation was calculated (see color code).....	68
Figure 34.	Seasonal cycle of monthly LTM EDH and EDH factor values (panels a-e) and correlations of EDH with EDH factors (panel f) for the Gulf of Aden (see Figure 20). (a) EDH and EDH standard deviation; (b) wind speed, u and v components of wind; (c) SST and Ta; (d) ASTD; (e) RH; (f) zero lag correlation for each month of EDH (panel a) with each of the factors (panels b-e), with the color of the correlation curves indicating the factor for which the correlation was calculated (see color code).....	71

Figure 35.	Comparison of monthly EDH from existing Navy climatology based on observations from 1970-1984 and the PJ ED model (blue), smart EDH climatology based on 1970-2006 reanalysis data and the NPS ED model (purple), and EDH climatology based on reanalysis data from 1970-1984 and the NPS ED model (dashed purple) for Marsden square 066 in the Arabian Sea (see Figure 20)..	73
Figure 36.	Comparison of monthly EDH from existing Navy climatology based on observations from 1970-1984 and the PJ ED model (blue), smart EDH climatology based on 1970-2006 reanalysis data and the NPS ED model (purple), and EDH climatology based on reanalysis data from 1970-1984 and the NPS ED model (dashed purple) for Marsden square 030 in the tropical NW IO (see Figure 20).	73
Figure 37.	LTM EDH (m) values for September from (a) smart EDH climatology based on reanalysis data for 1970-2006 and the NPS ED model; and (b) existing Navy climatology based on observations from 1970-1984 and the PJ ED model.	75
Figure 38.	Location of WHOI buoy (dark blue dot), nearest NCEP reanalysis grid points (light blue dots), and closest Marsden square. (Marsden square 066, dark blue box).	76
Figure 39.	Comparison of monthly EDH from: WHOI buoy in Arabian Sea for October 1994–October 1995 (white); existing Navy climatology from Marsden square 066 and based on observations from 1970-1984 and the PJ ED model (blue), smart EDH climatology from closest reanalysis grid point and based on 1970-2006 reanalysis data and the NPS ED model (purple), and EDH climatology from closest reanalysis grid point based on reanalysis data from 1994-1995 and the NPS ED model (dashed purple). See Figure 38 for locations.	77
Figure 40.	Correlation of our smart climatology EDH for the Diego Garcia region with SST across the IO. Black square marks the location of Diego Garcia. Image produced using NCEP reanalysis data and the NOAA/ESRL Physical Sciences Division web site at http://www.cdc.noaa.gov/ using NCEP reanalysis data, (Kalnay et al., 1996) (accessed September 2007).	79
Figure 41.	Correlation of our smart climatology EDH for the Diego Garcia region with SST across the IO and western-central Pacific. Image produced using NCEP reanalysis data and the NOAA/ESRL Physical Sciences Division web site at http://www.cdc.noaa.gov/ , using NCEP reanalysis data, (Kalnay et al., 1996) accessed September 2007.	80

Figure 42.	Correlation of our smart climatology EDH for the Diego Garcia region with 850 hPa geopotential height across the IO. Image produced using NCEP reanalysis data and the NOAA/ESRL Physical Sciences Division web site at http://www.cdc.noaa.gov/ , using NCEP reanalysis data, (Kalnay et al., 1996) accessed September 2007.....	81
Figure 43.	Correlation of our smart climatology EDH for the Somali coast region with OLR across the IO. Image produced using NCEP reanalysis data and the NOAA/ESRL Physical Sciences Division web site at http://www.cdc.noaa.gov/ , using data referenced at (Liebmann et al., 1996), accessed September 2007.....	81
Figure 44.	Correlation of our smart climatology EDH for the Somali coast region with surface zonal wind (u component of the wind) across the IO. Image produced using NCEP reanalysis data and the NOAA/ESRL Physical Sciences Division web site at http://www.cdc.noaa.gov/ , using NCEP reanalysis data, (Kalnay et al., 1996) accessed September 2007.....	83
Figure 45.	DMI created using NCEP reanalysis SST data and MEI (From: the CDC MEI web site http://www.cdc.noaa.gov/people/klaus.wolter/MEI/mei.html , accessed September 2007).....	84
Figure 46.	WS anomalies (ms^{-1}) for positive IOZM composite.....	86
Figure 47.	Anomalies for positive IOZM composite: (a) vector wind (ms^{-1}); (b) SST $^{\circ}\text{C}$; (c) RH (%); and (d) ASTD ($^{\circ}\text{C}$).	88
Figure 48.	EDH anomalies (m) for positive IOZM composite.....	89
Figure 49.	EDH anomaly (m) for September 1997.	90
Figure 50.	EDH anomaly (m) for September 1996.	91
Figure 51.	Vertical coverage diagrams of propagation loss for: (a) standard atmosphere with no ED; (b) atmosphere with ED. From Davidson (2006).....	96
Figure 52.	Estimated surface radar detection ranges (km) based on September LTM EDH from our smart EDH climatology, for a C-band radar at 30 ft and detection threshold of 150 dB.....	97
Figure 53.	Estimated surface radar detection ranges (km) based on September 1997 EDH, for a C-band radar at 30 ft and detection threshold of 150 dB. Compare to Figure 52.....	98
Figure 54.	Estimated surface radar detection ranges (km) anomalies for September 1997 EDH, for a C-band radar at 30 ft and detection threshold of 150 dB. Compare to Figures 52-53.....	98
Figure 55.	Estimated CoF (GHz) based on September LTM EDH from our smart EDH climatology.....	99
Figure 56.	Vertical coverage diagrams of propagation loss (a) standard atmosphere with no ED, (b) atmosphere with ED. From Davidson (2006).....	100

Figure 57.	Flow diagram of results and of recommendations for future work within the BonD concept.....	106
Figure 58.	EDH computed by the NPS model versus ASTD for six different relative humidity values (six colored curves in each panel) and four different wind speed values (four panels). (From: Frederickson (2007))......	111
Figure 59.	EDH computed by the NPS model versus ASTD for six different SST values (six colored curves in each panel) and four different relative humidity values (four panels). (From: Frederickson (2007)).	112
Figure 60.	EDH computed by the NPS model versus ASTD for six different wind speed values (six colored curves in each panel) and four different relative humidity values (four panels). (From: Frederickson (2007))......	113
Figure 61.	LTM EDH (m) for January. Note coastal caution (Chapter III, section A).	115
Figure 62.	LTM EDH (m) for January for NW IO. Note coastal caution (Chapter III, section A).....	115
Figure 63.	LTM EDH (m) for February. Note coastal caution (Chapter III, section A).	116
Figure 64.	LTM EDH (m) for February for NW IO Note coastal caution (Chapter III, section A).....	116
Figure 65.	LTM EDH (m) for March. Note coastal caution (Chapter III, section A).....	117
Figure 66.	LTM EDH (m) for March for NW IO Note coastal caution (Chapter III, section A).	117
Figure 67.	LTM EDH (m) for April. Note coastal caution (Chapter III, section A).....	118
Figure 68.	LTM EDH (m) for April for NW IO. Note coastal caution (Chapter III, section A).	118
Figure 69.	LTM EDH (m) for May. Note coastal caution (Chapter III, section A).....	119
Figure 70.	LTM EDH (m) for May for NW IO. Note coastal caution (Chapter III, section A).	119
Figure 71.	LTM EDH (m) for June. Note coastal caution (Chapter III, section A).....	120
Figure 72.	LTM EDH (m) for June for NW IO. Note coastal caution (Chapter III, section A).	120
Figure 73.	LTM EDH (m) for July. Note coastal caution (Chapter III, section A).....	121
Figure 74.	LTM EDH (m) for July for NW IO. Note coastal caution (Chapter III, section A).	121
Figure 75.	LTM EDH (m) for August. Note coastal caution (Chapter III, section A).....	122
Figure 76.	LTM EDH (m) for August for NW IO. Note coastal caution (Chapter III, section A).	122

Figure 77.	LTM EDH (m) for September. Note coastal caution (Chapter III, section A).	123
Figure 78.	LTM EDH (m) for September for NW IO. Note coastal caution (Chapter III, section A).....	123
Figure 79.	LTM EDH (m) for October. Note coastal caution (Chapter III, section A).	124
Figure 80.	LTM EDH (m) for October for NW IO. Note coastal caution (Chapter III, section A).....	124
Figure 81.	LTM EDH (m) for November. Note coastal caution (Chapter III, section A).	125
Figure 82.	LTM EDH (m) for November for NW IO. Note coastal caution (Chapter III, section A).....	125
Figure 83.	LTM EDH (m) for December. Note coastal caution (Chapter III, section A).	126
Figure 84.	LTM EDH (m) for December for NW IO Note coastal caution (Chapter III, section A).....	126
Figure 85.	Seasonal cycle of monthly LTM EDH and EDH factor values (panels a-e) and correlations of EDH with EDH factors (panel f) for Somali Coast region (see Figure 20). (a) EDH and EDH standard deviation; (b) wind speed, u and v components of wind; (c) SST and Ta; (d) ASTD; (e) RH; (f) zero lag correlation for each month of EDH (panel a) with each of the factors (panels b-e), with the color of the correlation curves indicating the factor for which the correlation was calculated (see color code).....	127

LIST OF TABLES

Table 1.	Primary factors used in this study and key factors calculated in this study. The primary factors were obtained from the NCEP reanalysis 1 data set.....	33
Table 2.	Significance of correlation values for a 37 year climatology. Information from http://www.cdc.noaa.gov/Correlation/significance.html , accessed August 2007.	55
Table 3.	IOZM and ENLN events selected based on DMI and MEI, respectively. Note that there is some overlap in the positive IOZM and EN years, and in the negative IOZM and LN years (see Chapter I, section E).....	85
Table 4.	Correlations of EDH with MEI, DMI and NAOI for EDH lagging the climate indices by 0, 1, and 2 month lags, grouped by lag period. Significant correlations are indicated by colored cells (see color key). The absence of a significant correlation is indicated by white cells.	92
Table 5.	Correlations of EDH with MEI, DMI and NAOI for EDH lagging the climate indices by 0, 1, and 2 month lags, grouped by focus region. Significant correlations are indicated by colored cells (see color key). The absence of a significant correlation is indicated by white cells.	93

THIS PAGE INTENTIONALLY LEFT BLANK

LIST OF ACRONYMS

ACMES	Advanced Climate Modeling and Environmental Simulations
APM	Advanced Propagation Model
AREPS	Advanced Refraction Effects Prediction System
ASTD	Air-Sea Temperature Difference
BonD	Battlespace on Demand
CDC	Climate Diagnostics Center
CoF	Cut Off Frequency
CPC	Climate Prediction Center
DJF	Decemeber-January-February
DoD	Department of Defense
DMI	Dipole Model Index
DMI+	Positive phase of the DMI
DMI-	Negative phase of the DMI
ED	Evaporation Duct
EDH	Evaporation Duct Height
EN	El Nino
ENLN	El Nino-La Nina
ESRL	Earth System Research Laboratory
FMA	February-March-April
GISST	Global Sea and Ice SST Database
GOA	Gulf of Aden
GOO	Gulf of Oman
HWC	Hadley-Walker Cell
ICOADS	International Comprehensive Ocean-Atmosphere Data Set
IO	Indian Ocean
IOZM	Indian Ocean Zonal Mode
ITCZ	Inter-tropical Convergence Zone
LN	La Nina
LTM	Long-Term Mean
MC	Maritime Continent
MEI	Multi-variate El Nino Index

MJJ	May-Jun-Jul
MOS	Monin-Obukhov similarity theory
NAO	North Atlantic Oscillation
NAOI	North Atlantic Oscillation Index
NCAR	National Center for Atmospheric Research
NCEP	National Centers for Environmental Prediction
NOAA	National Oceanographic and Atmospheric Association
NPS	Naval Postgraduate School
OND	October-November-December
OLR	Outgoing Longwave Radiation
PJ	Paulus-Jeske
REP	Recognized Environmental Picture
RH	Relative Humidity
SAG	Southern Arabian Gulf
SH	Specific Humidity
SLP	Sea-Level Pressure
SON	September-October-November
SST	Sea Surface Temperature
SSTA	Sea Surface Temperature Anomaly
Ta	Air Temperature
U.S.	United States
VCD	Vertical Coverage Diagram
WS	Wind Speed

ACKNOWLEDGMENTS

Firstly, I would like to thank my advisors, Dr. Tom Murphree and Mr. Paul Frederickson, for their guidance, tutelage and patience in preparing this study.

Many thanks and appreciation also go to those persons who extended their time and professional expertise as I produced this thesis, especially Bob Creasey, Mary Jordan, Arlene Guest and Bill Little.

Lastly and most importantly I would like to thank my parents, back in the UK, and friends, in Monterey, for their encouragement and support throughout this educational adventure.

THIS PAGE INTENTIONALLY LEFT BLANK

I. INTRODUCTION

A. BACKGROUND

British Maritime Doctrine states that ‘a tactically exploitable knowledge of the environment based on superior technology is essential for both joint and maritime commanders’ and that ‘seasonal fluctuations in weather can have strategic significance’ (Great Britain. Ministry of Defence, 2004). Relevant, timely and accurate climate and weather assessments and their likely impacts on sensor performance must be incorporated into the operational planning cycle if this mandate is to be met.

The northern Indian Ocean (IO) is an important area for maritime security operations, and as such the ability to predict communication, radar and electronic support ranges enhances military planning and operations. Naval operations, in this area and worldwide, are particularly concerned with the prediction of radar detection ranges for small surface and low-altitude airborne targets, such as anti-ship cruise missiles, low-flying aircraft, submarine periscopes and boats which could be associated with an asymmetric threat. Naval war fighters are also wary of their vulnerability to detection by hostile or neutral radars. Surface electromagnetic propagation over the ocean is highly sensitive to near-surface atmospheric variability, particularly the height of the evaporation duct, which is a shallow refractivity feature that forms just above the ocean surface. Due to its importance in quantifying atmospheric impacts on microwave-frequency propagation over the ocean, the evaporation duct height (EDH) and its climatic variations, was the focus of this study.

United States (U.S.) Joint Publication 3-59 emphasizes that ‘state-of-the-art long-range forecasting techniques’ are required for commanders to exploit the environment and reduce its adverse effects. Representative climate long term mean (LTM) values form the basis for tactical evaluation of current weather conditions, and thus climatology feeds into the operational planning cycle. The

existing U.S. Navy EDH climatology is based on sparse ship observations over a relatively short time period and an outdated evaporation duct (ED) model. Furthermore this climatological dataset does not utilize recent advances in the development and uses of modern, or smart, climatologies to support military operations.

This research examined the use of modern climate reanalysis data to provide improved EDH LTM values across the equatorial and northern IO. It also used smart climatology methods to investigate the sensitivities of EDH to environmental variability, including the impacts of climatic trends and variations, such as El Nino-La Nina (ENLN) and the Indian Ocean Zonal Mode (IOZM). Smart climatology geographic plots were developed for EDH and its resulting impact on sensor performance, akin to U.S. Navy environmental assessment surfaces or NATO additional military layers.

B. EVAPORATION DUCT AND ELECTROMAGNETIC PROPAGATION

An evaporation duct is an atmospheric refractivity feature which forms just above the ocean surface, due to a rapid decrease in humidity with height over open water. The EDH is the height in the surface layer where the vertical gradient in modified refractivity changes from negative to positive. The trapping layer below the EDH behaves like a waveguide, and can lead to decreased propagation loss at microwave frequencies and extended radar detection ranges. Due to their shallow nature EDHs are generally on the order of 10 m, evaporation ducts begin to significantly impact electromagnetic (EM) propagation only at microwave frequencies greater than roughly 0.5 GHz. EDH is the best parameter for quantifying this near-surface microwave propagation feature, which can be highly variable in space and time. Throughout this thesis the term *surface* is used for surface boundary layer conditions (e.g., SST) and near-surface factors (e.g., wind speed (WS) at 10 m, detection ranges).

1. Modified Refractivity and Ducting Layers

The propagation of EM radiation is dependent upon the horizontal and vertical gradient of refractivity. Modified refractivity (M), which takes Earth's curvature into consideration, is defined as:

$$M = 77.6 \frac{p}{T} - 5.6 \frac{e}{T} + 375000 \frac{e}{T^2} + 0.157z$$

where T (K) is atmospheric temperature, p (hPa) is total atmospheric pressure, e (hPa) is water vapor pressure at height z (m), and the constants have been empirically determined. See (Babin et al., 1997) for further background information on refractivity.

The vertical gradient of M determines the type of refraction conditions: normal, super-refraction or sub-refraction. Super-refraction occurs when the M gradient is negative and causes propagating EM waves to bend downward. Sub-refraction occurs when the M gradient is positive and causes propagating waves to bend upward. A surface duct occurs when waves are bent towards and then reflect off the sea surface in a repeating process, as illustrated in Figure 1. The height of the surface duct is at the lowest point above a super-refractive layer where there is a local minimum in M .

From the equation for modified refractivity (M) we see that super-refraction occurs when vapor pressure (e) rapidly decreases with height and/or air temperature (T_a) increases with height. Over the ocean, humidity generally decreases rapidly with height, from near saturation at the surface to the ambient air humidity conditions at a given level; thus, the ED is a persistent feature over the oceans.

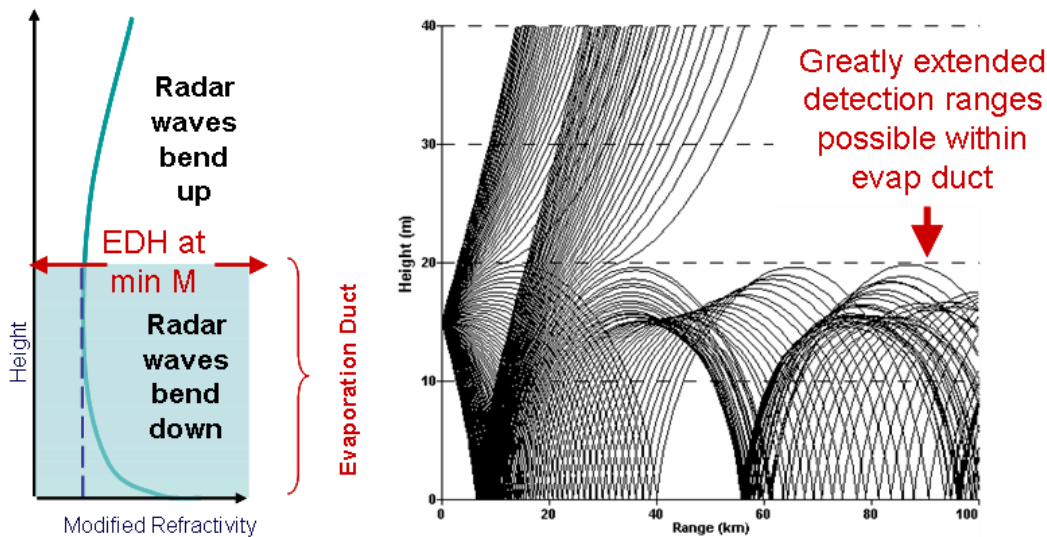


Figure 1. A vertical M profile for a surface duct and its associated height versus range ray trace plot of X-band waves emitted from an antenna at 25 m height propagating through an atmosphere with an EDH of 20 m (After: Frederickson et al., 2000)

Due to changing atmospheric conditions, the vertical profile of M will vary in space and time, thus producing different types of trapping features, both adjacent to the surface and elevated above the surface. Figure 2 shows a series of different plots of M versus altitude and identifies the resulting different types of ducts.

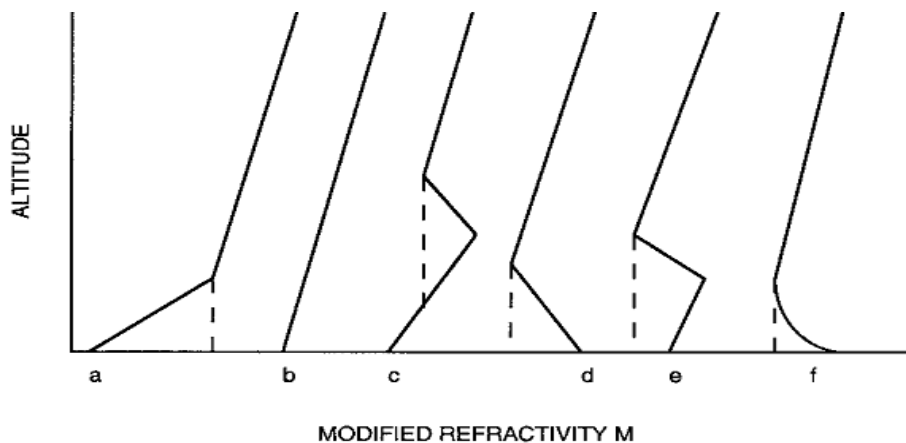


Figure 2. Plots of modified refractivity (M) versus altitude: (a) sub-refractive layer denoted by dashed line; (b) normal refraction; (c) elevated duct denoted by dashed line; (d) surface duct denoted by dashed line; (e) surface-based duct denoted by dashed line, (due to an elevated layer with a strongly negative vertical M gradient); (f) ED denoted by dashed line. (From: Babin et al., 1997)

Figure 2 (d-f) depicts different types of surface ducts, all of which if present, will have an impact on surface propagation. For this thesis, however, we focus on evaporation duct variation alone.

Ideally EDH would be determined by measuring the vertical profile of M near the surface. However, it is not feasible to routinely measure refractivity close to the ocean surface, and thus EDH is determined from an evaporation duct model using bulk measurements. A number of bulk evaporation duct models have been developed (e.g., Babin et al., 1997, Frederickson et al., 2000) and most utilize Monin-Obukhov similarity (MOS) theory. MOS theory assumes that conditions are horizontally homogeneous and stationary, and that turbulent fluxes are nearly constant within the surface layer. The Naval Postgraduate School (NPS) bulk evaporation duct (ED) model was used throughout this study. A description of this model and how MOS theory is used in its formulation can be found in Frederickson (2000).

2. The Effect of Atmospheric Factors on EDH

The vertical distribution of humidity, which to a great extent determines the EDH, is dependant upon sea surface temperature (SST) and turbulent mixing near the surface. Thus, the main factors which determine EDH are SST, wind speed, T_a and humidity. Figures 3 and 4, show different EDH curves as a function of the stability, defined in terms of the air-sea temperature difference (ASTD), as the relative humidity (RH) and wind speed (WS) vary. Near-surface conditions are considered stable (unstable) if T_a is greater (less) than SST. From these Figures it is evident that EDH can increase dramatically if conditions become stable, assuming no other factors are altered. Figure 3 indicates that as RH decreases EDH increases and Figure 4 shows that EDH generally increases (decreases) with increasing wind speed when ASTD is negative (positive). This is due to the fact that increasing WS leads to enhanced vertical mixing, which causes near-surface conditions to become more neutral. Further plots of EDH versus ASTD for various changing conditions are available at Appendix A.

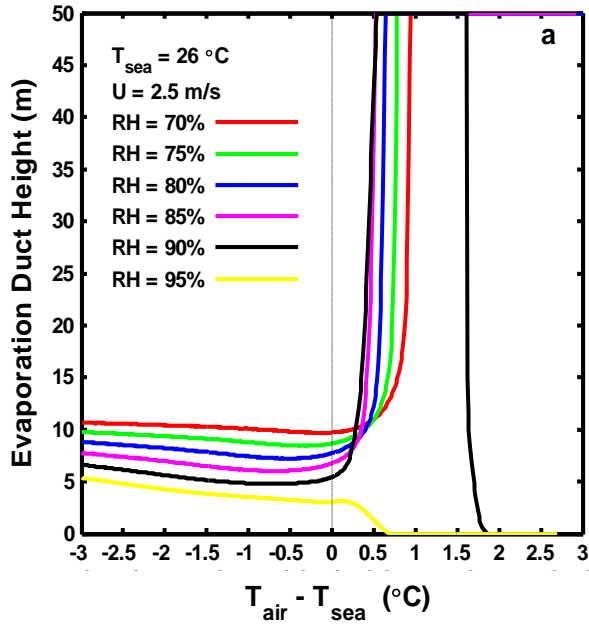


Figure 3. EDH computed by the NPS ED model versus ASTD for different relative humidity, as indicated. (From: Frederickson, 2007).

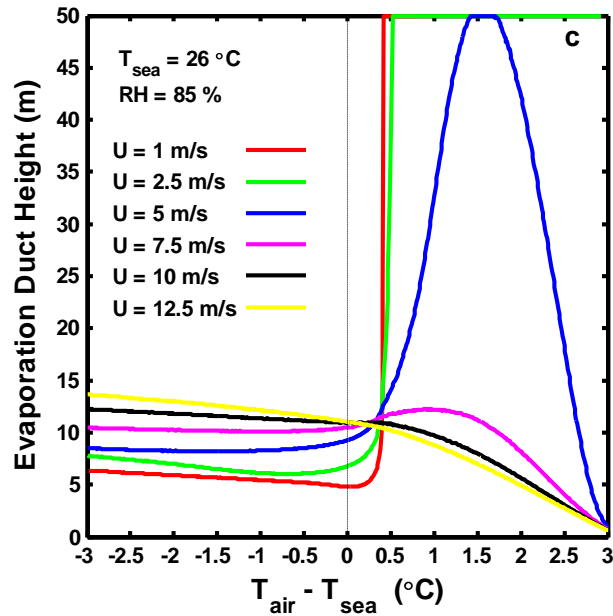


Figure 4. EDH computed by the NPS ED model versus ASTD for different wind speed values, as indicated. (From: Frederickson, 2007)

From these plots it is evident that EDH varies due to changing local near-surface atmospheric and ocean surface factors; however, these factors are not independent of each other. The larger scale dynamic system dictates how near-surface and SST conditions change. Thus we expect some correlation of EDH to varying weather patterns and large scale, persistent atmosphere-ocean climate variations.

Whilst the NPS ED model computes EDH for most atmospheric conditions, there is some variability in the expected accuracy of the output values. These errors occur due to measurement errors and the subsequent model sensitivity to the errors, and because the atmosphere seldom adheres to all the assumptions required by MOS theory. Full details of the NPS ED model accuracy are found at Frederickson (2000). The total EDH errors can be summarized for different stability conditions as follows:

- In unstable regimes where ASTD is less than -0.5°C , errors are generally less than 2 m.
- For near neutral conditions where ASTD is greater than -0.5°C and less than 1°C , errors are dominated by errors in the environmental surface factors and increase if the wind speed is low. In these conditions it is especially important to acquire precise and accurate input factor values.
- In stable conditions, with ASTD greater than 1°C , overall errors can easily exceed 4 m especially in low wind and humidity regimes.

Departures from MOS theory are most likely to occur in coastal regions with off-shore breezes. Here, due to advection effects, there are likely to be internal boundary layers, and conditions are less likely to be stationary or horizontally homogeneous. This littoral region is of high operational importance and, whilst EDH calculations will reveal some aspects of the surface duct complexity, the full extent of refractive variability cannot be described by bulk surface measurements alone. The reader is referred to (Geernaert, 2007) for generic notes on non-homogeneity in coastal regions and to (Atkinson and Zhu, 2005; Atkinson and Zhu, 2006) for detailed investigations of coastal refractive conditions in the Arabian Gulf.

3. EM Propagation and Detection Range

Microwave propagation models such as the Advanced Propagation Model (APM) which drives the Advanced Refractive Effects Prediction System (AREPS) used by the U.S. Navy and Royal Navy, are used to predict radar and communications system performance. These models require a vertical profile of refractivity to describe the propagation environment. Due to the difficulties of measuring refractivity near the surface, operational models often incorporate a bulk ED model. Both the NPS and the Paulus-Jeske ED models can be used within AREPS, and the ED is blended with higher altitude refractivity data. As the NPS ED model is a state-of-the art model which provides a better estimation of EDH (Frederickson et al., 2001, Frederickson et al., 2003) it is the model used throughout this study.

EDH is the most critical single factor in determining near surface refractivity conditions, and is thus the best parameter for quantifying near-surface microwave propagation. Higher EDHs often lead to increased signal strength and radar detection ranges, depending upon the frequency, and the height of the radar and target.

Propagation loss is the ratio of transmitted power to the received power at a given height and range. Radar detection range is estimated from the computed propagation loss by determining the maximum distance where the propagation loss at the target height is equal to the propagation loss detection threshold assumed for that target. The propagation loss detection threshold is based on a complex combination of target radar cross section, signal to noise ratio, sea clutter and other factors, (Frederickson et al., 2000). Figure 5 illustrates the estimation of radar detection range from computed propagation loss data. This Figure shows propagation loss at the target height (5 m in this example) versus range for various EDHs indicated by the different colored curves. Assuming that the current EDH is 10 m (shown by the red curve) and the target detection threshold is 130 dB (indicated by the dashed horizontal line), the estimated

detection range is found at the intersection of the red propagation loss curve with the 130 dB threshold line, which is about 17 km in this example.

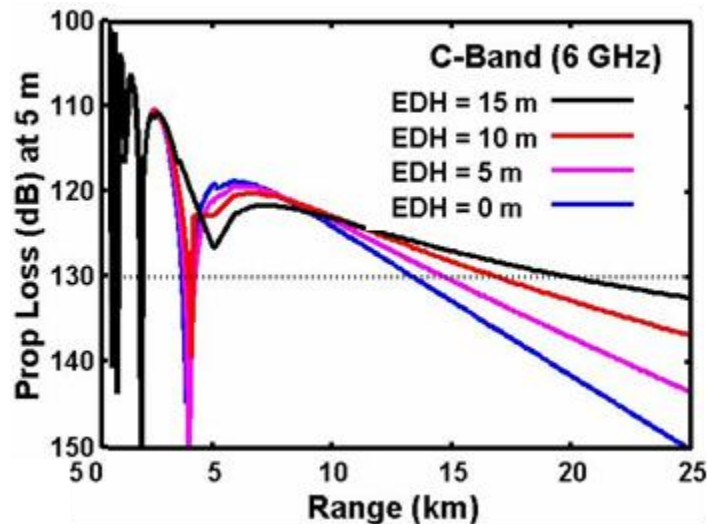


Figure 5. Propagation loss versus range of C-band radar for a refractive profile with different EDH values. Dotted line indicates the propagation loss threshold. (After: Frederickson et al., 2004)

The ED forms an imperfect, or leaky, waveguide for electromagnetic energy (Frederickson et al., 2000) thus if the emitter and target are within the duct, then propagation loss will decrease less with range and the detection range will increase. Even if the transmitter and target are not located within the duct, there will be some coupling of energy into it, and the detection range is likely to increase. The decrease in propagation loss is particularly evident for frequencies above a given frequency threshold, known as the cut off frequency (CoF), which is given by the following empirical expression from Davidson (2006):

$$\text{CoF (GHz)} = 3.6 \times 10^{11} \times \text{EDH(m)}^{-3/2}$$

It should be noted that, although its name alludes to a definite frequency, due to the leaky nature of the duct and surface inhomogeneities, the CoF gives only an indication of the lower frequency limit at which microwaves will be significantly impacted by the presence of an ED of the defined height.

Surface radar detection ranges are highly dependant on EDH. Thus, a comprehensive understanding of spatial and temporal EDH variation provides an improved assessment of likely detection ranges. This in turn leads to improved knowledge of the environmental effects on sensor performance, thus improving tactical awareness and strategic planning.

C. SMART CLIMATOLOGY

1. Concept

Military climatology products are often based solely upon long term means of observational data and generally fail to utilize recent advances in the development and uses of modern climatology. In fact, recent assessments have shown (Murphree and Ford 2007) that the U.S. Department of Defense (DoD), and particularly U.S. Navy, climatology lags significantly behind the state of the science used by the civilian sector, and that the gap is widening. Smart climatology can be defined as 'state-of-the-art basic and applied climatology that directly supports DoD operations' (Murphree 2007a). An outline of the smart climatology process is at Figure 6.

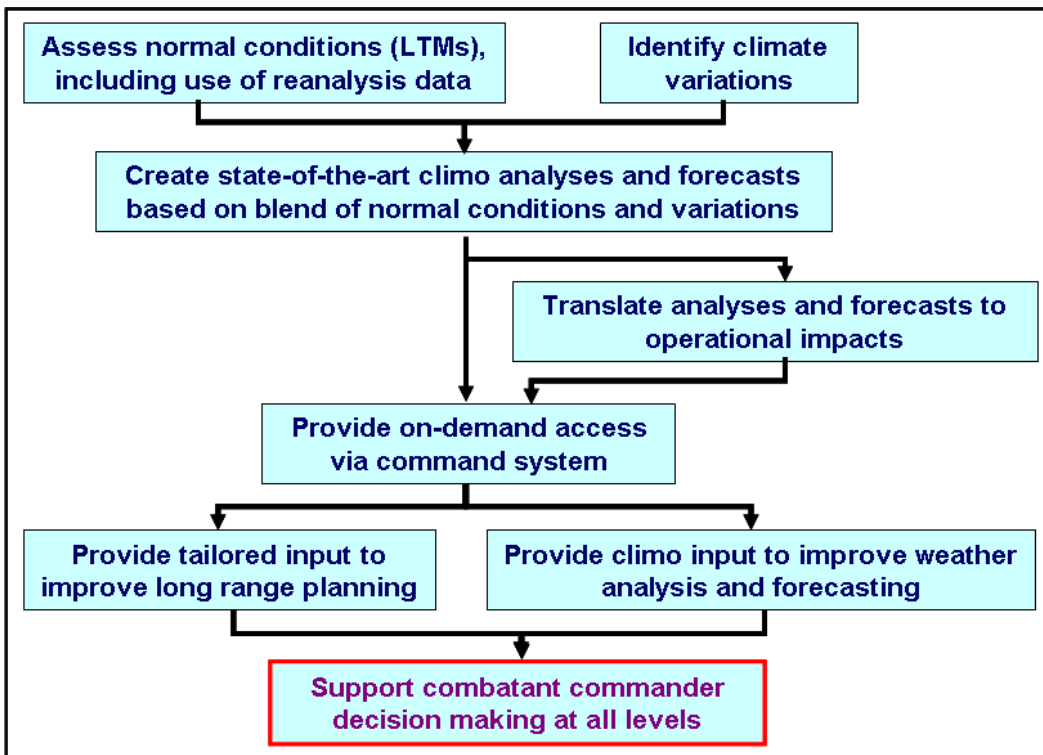


Figure 6. Smart Climatology: Flow diagram of Development and Applications (After: Murphree, 2007a)

During the smart climatology process, numerous elements of modern climatology can be used, such as:

- Full suite of in-situ and remote observational data sets
- Reanalysis
- Downscaling
- Data access, mining, processing, and display tools
- Modern statistical and dynamical analysis methods
- Long term means and higher order statistics
- Climate variations (e.g., regimes, trends, oscillations)
- Climate system monitoring
- Climate system modeling
- Statistical and dynamical climate forecasting
- Online, real-time, user-driven, data access, analysis, and display

2. Design of Study

Existing EDH climatology is based upon an observational dataset, which computes EDH from available observations of the factors that determine EDH for a given region and time of year. In data sparse regions (e.g., vast areas of the IO) there will be major spatial and temporal gaps in the available observations. In this study we use a civilian reanalysis dataset which uses all available observations assimilated into a dynamical model to produce analyses of atmospheric variables and SST. This is a method used to produce many state-of-the-art civilian operational climatologies, and can be defined as: (Murphree and Ford 2007)

(Reanalysis is:) 'The analysis of climate system components using modern analysis processes to analyze past and present states of the climate system. Reanalysis is the same as standard atmospheric or oceanic analysis, except that it applies a consistent set of analysis procedures to all times in the reanalysis period. Oceanic and atmospheric reanalyses yield gridded data sets that are temporally and spatially continuous (i.e., no temporal or spatial gaps). For many reanalyses, the reanalysis period is several decades long, and the reanalysis region is the global ocean or atmosphere. Reanalyses can have relatively high temporal and spatial resolution (e.g., mesoscale reanalyses: hourly and 10 km; global reanalyses: six hourly and one degree). Reanalysis data include many derived fields (momentum, energy, and mass fluxes; sea surface heights; currents; precipitation; soil moisture, etc.) for which direct observations may be difficult to obtain.'

This study uses modern climatological statistical analysis methods, (e.g., compositing and correlations) to further our understanding of the relationship of EDH to its component factors and how it is affected by climate variations. We display EDH in an 'operationally friendly' manner and provide military forecasters with a clear framework to predict how EDH varies on medium to long timescales. Finally, we investigate the use of our results for performance assessment and 'operationally useful' displays.

D. AREA OF STUDY: INDIAN OCEAN

The Indian Ocean (IO) was chosen as our area of study as this region has been the focus of much recent research and it contains many areas of operational interest. Although the evaporation duct is a phenomenon occurring over large water surfaces, we extended our studies of atmospheric factors to include a significant portion of the surrounding land, expecting that large scale weather patterns could help explain the intricacies of EDH variation over the ocean.

Our data area covers latitudes 35°N to 15°S and longitudes 025° to 120°E, and thus includes the Somali Peninsula, Ethiopian Highlands, Arabian Peninsula, some of the Tibetan plateau, India, Indo-China Peninsula, and Maritime Continent (MC). The southern limit of the data area captures the top of Madagascar and excludes much of the southern IO. These limits were selected so we could focus on the NW IO and equatorial region, whilst encompassing some of the regions that drive the climate system in this area. A map of our study area is shown in Figure 7.

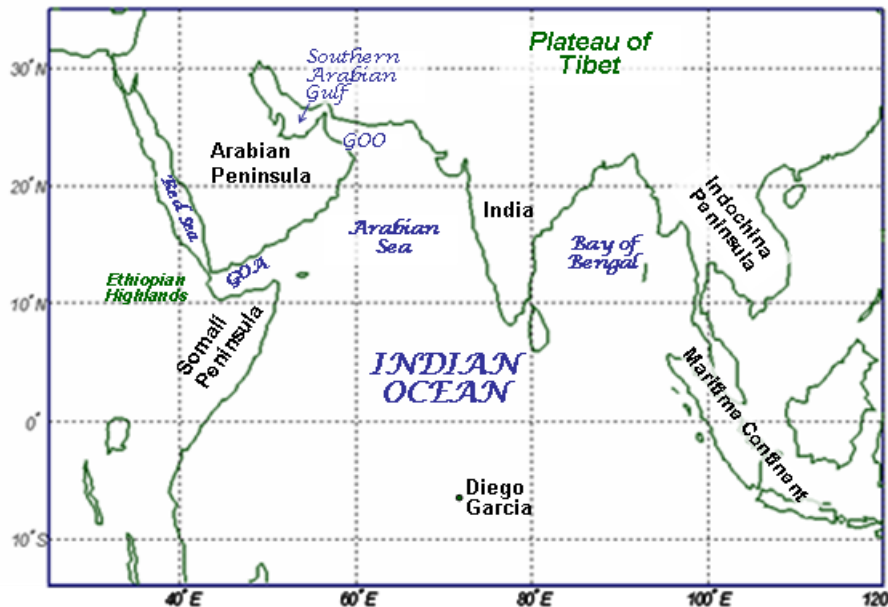


Figure 7. The Indian Ocean region examined in our study and located within 35°N-15°S; 025°E-120°E. Abbreviations: GOO Gulf of Oman, GOA Gulf of Aden.

For this study our focus regions are three areas of current operational interest: the Arabian Gulf, Gulf of Oman (GOO), and sea areas around the Horn of Africa and, in addition, an area of upwelling off the coast of Oman and an equatorial example, namely the waters surrounding Diego Garcia.

1. Long Term Mean of Climate and Seasonal Cycle in SW Asia

The climate system of SW Asia is dominated by the Asian-Australian monsoon, a coupled ocean-atmosphere-land phenomenon. Figures 8 and 9 illustrate the mean flow for January and July. During the boreal winter, differential heating between land and ocean result in higher pressure over cool continental Asia than over the warmer ocean. This creates a flow of surface winds from Asia to the equator; initially cool and dry the air gains moisture with increasing sea track. This northeast monsoon season lasts from October-November to March-April, after which there is a short transition season before the southwest wind regime sets up. From May-June until August-September low pressure over Asia draws the southern hemisphere trade winds across the Arabian Sea and Bay of Bengal. For further information on the Asian monsoon the reader is referred to (Webster et al., 1998) and (Loschnigg et al., 2003).

The Somali Jet is a particularly intense and persistent component of the southwest monsoon flow. It is a low level jet situated off the coast of Somalia that flows towards the Arabian Sea, and has maximum core wind speeds of up to 50 ms^{-1} during July-August. The core height is usually centered at an elevation of 1500 m; however, surface winds are also affected reaching $\sim 15 \text{ ms}^{-1}$. During the southwest monsoon along western boundary coastlines (e.g., Somali and Omani coastlines), net offshore Ekman transport results in upwelling of relatively cool subsurface water. This causes relatively low SSTs, marine boundary layer saturation and frequent development of fog and stratus; these conditions may extend some 200 nm off shore.

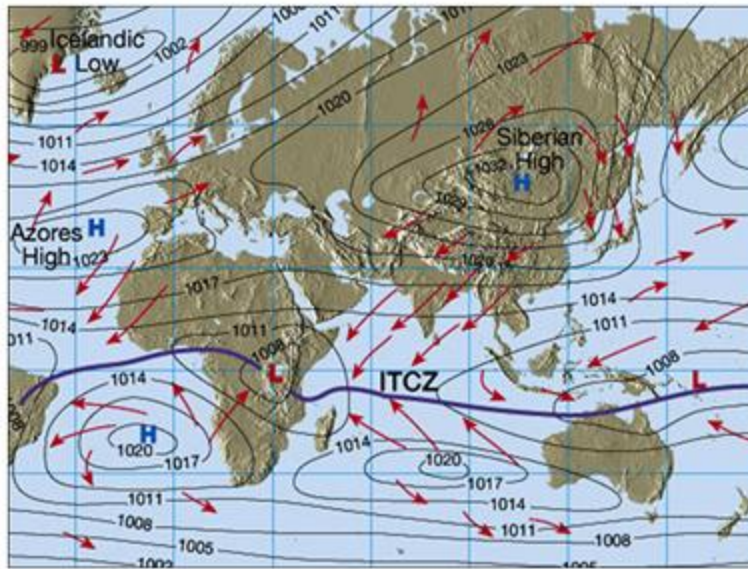


Figure 8. Schematic illustration of the major lower atmospheric and upper oceanic circulation features during the January peak of the Asian winter monsoon. (From: Lutgens and Tarbuck (2001), available online from <http://www.ux1.eiu.edu/~cfjps/1400/circulation.html>). Accessed September 2007.

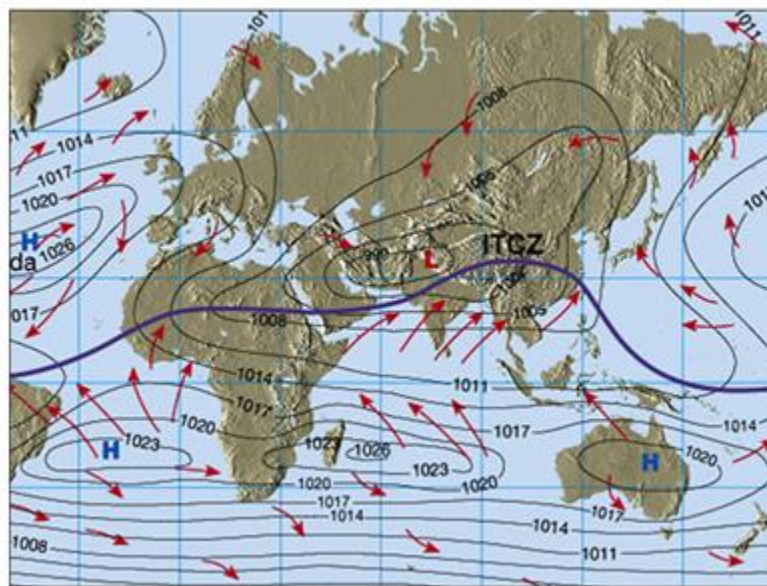


Figure 9. Schematic illustration of the major lower atmospheric and upper oceanic circulation features during the July peak of the Asian summer monsoon. (From: Lutgens and Tarbuck (2001), available online from <http://www.ux1.eiu.edu/~cfjps/1400/circulation.html>). Accessed September 2007.

The equatorial trough is a band of low pressure that lies between the northern and southern hemisphere subtropical pressure belts (American Meteorology Society Glossary of Meteorology). It is a region of high humidity in which small variations in atmospheric stability can cause large differences in weather conditions, and thus in EDH. The equatorial trough contains regions of doldrums, and sections of it are intertropical convergence zones. This band moves from south to north and back as the annual cycle of solar forcing crosses the equator twice a year.

Due to the coupled nature of the ocean-atmosphere boundary, the monsoon regime also affects surface currents within the region. Figure 10 shows the mean surface circulation for each phase of the monsoon regime. These currents circulate water masses of various temperatures around the IO basin, and thus influence SST, ASTD and EDH. Mean SST in the tropical western IO varies between 26 ° and 28 °C, which is cooler than its eastern counterpart due to upwelling off Somalia and surface cooling off Madagascar .

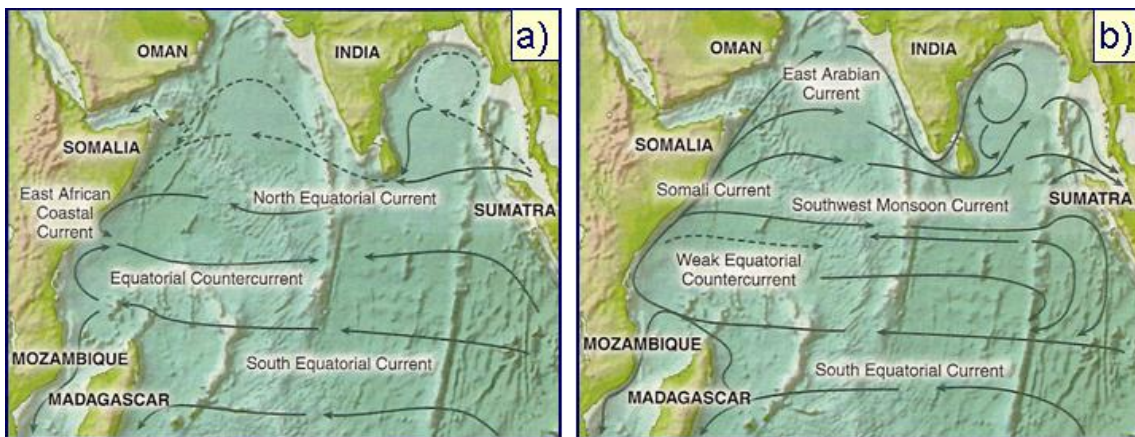


Figure 10. A schematic representation of identified current branches during (a) January (northeast monsoon) and (b) July (southwest monsoon). (From: Sean Chamberlin and Dickey, 2007)

The monsoon regime is the dominant climatological pattern. However, the IO has other climate modes which are inherent to the basin (e.g., modes linked to ENLN in the tropical Pacific, internal independent oscillations, Lau 2003, Krishnamurthy 2002).

E. LARGE SCALE CLIMATE VARIATIONS

LTM climatology is highly useful for military planning, on all time scales, and forms the basic knowledge required for a tactically useful environmental background. However, by their very nature, LTM values can not reflect significant climate variations that can impact operations and thus should be considered in planning. A climate variation is a persistent deviation from the LTM value of a climate system variable (e.g., temperature, winds, humidity) (Murphree 2006d). A persistent deviation is a departure from the LTM on the timescale of a week or more. This makes climate variations critical to extended range (i.e., medium to long range) forecasting, and thus to military planning.

EDH is dependent upon surface factors (WS, Ta, SST and humidity), and as climate variations influence these surface factors it is expected that EDH will also vary due to climate variation influences. There are numerous known climate variations, of varying strengths and time periods, affecting broad areas of the global climate system. In this study, we will concentrate on two inter-annual variations, El Nino-La Nina (ENLN) and the Indian Ocean Zonal Mode (IOZM). ENLN is a well studied and understood oscillation originating in the Pacific Ocean, while the IOZM is a more recently and controversially defined dipole variation in the IO.

1. El Nino – La Nina

During an El Nino (EN) or La Nina (LN) event the magnitude and influence of global fluctuations are second only to the seasonal cycle (Philander 1990). These events have a period between two and seven years, usually last about one year starting in May-June of the first year and lasting until the following May-June. (Murphree 2006a). The basic progression for an EN or LN event can be thought of as a chain of anomalous events (Murphree 2006a). A synopsis of the anomalous patterns and the sequence associated with ENLN is described and

illustrated below; but for further details on the development, cycle and effects of ENLN the reader is referred to Murphree 2006a, Philander 1990, Ropelewski and Halpert 1987, 1989, 1996, and Hildebrand 2001.

For an EN event, the basic progression is (Murphree 2006a):

- Pacific subtropical highs become anomalously low and/or tropical – southeast Asian Pacific lows become anomalously high.
- Pacific trade winds become anomalously weak.
- Sea surface temperature (SST) becomes anomalously cool (warm) in the western (eastern) tropical Pacific.
- Tropical convection becomes anomalously weak (strong) in the western (eastern) tropical Pacific.
- Energy, moisture, and momentum transports into and out of the tropical Pacific becomes anomalous in many ways.

A LN event follows an anomalous sequence that is approximately opposite to the outline above. Differences in the atmospheric global Hadley-Walker circulation for normal, EN, and LN events are clearly shown at Figure 11. The atmospheric and oceanic effects in the Pacific region are seen in the schematics at Figure 12, and these illustrate the changing depth of the thermocline caused by anomalous upwelling. Part of the oceanic process that links the SST to the slow physics of thermocline dynamics involves Rossby and Kelvin waves are essential elements in controlling the ENLN cycle (Meyers et al., 2007). They are also key to the predictability and persistence of the climate system. SST is a primary factor in determining the phase of the tropical Pacific ENLN variation. Figure 13 shows a map of the correlation of SST in the Pacific and Indian basins with an ENLN index. The SST correlations have a distinctive pattern across the Pacific and IO basins and are, in large part, the result of the atmospheric and oceanic Rossby-Kelvin wave response. Note in particular that Figure 13 reveals a tendency for SST anomalies (SSTAs) in the western (eastern) IO to vary in phase with SSTAs in the central-eastern (western) tropical Pacific on interannual scales.

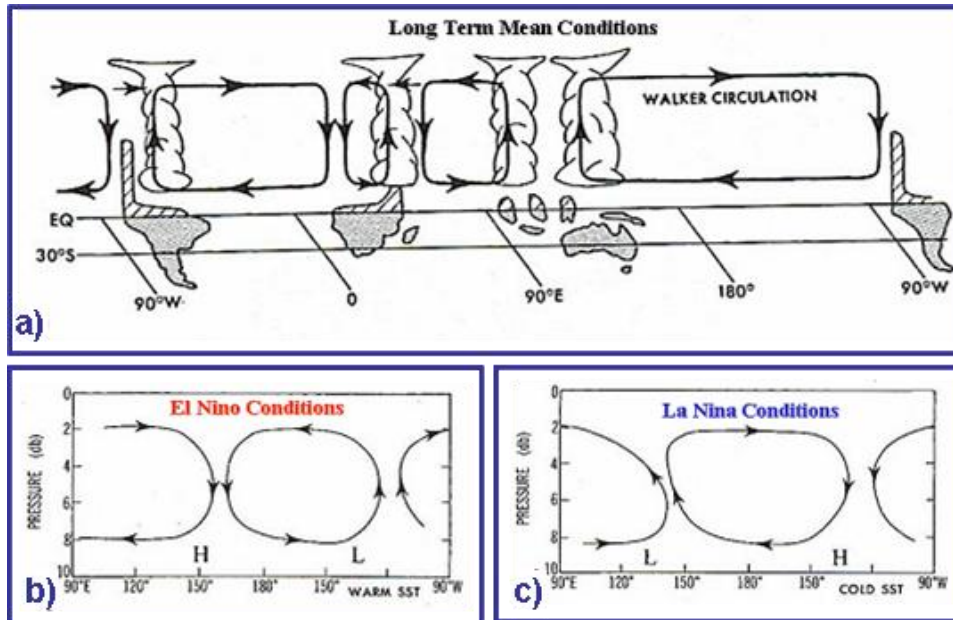


Figure 11. Schematic representation of the equatorial zonal component of the Hadley-Walker circulation (HWC): a) long term mean (LTM) zonal equatorial HWC, b) anomalous zonal equatorial HWC during EN, and c) anomalous zonal equatorial HWC during LN. After: Peixoto and Oort (1992). Note the LTM zonal overturning circulations in the tropical Atlantic, African, IO, and Pacific regions. These are the Walker circulation components of the HWC. Note that the IO and Pacific Walker circulations are weakened (strengthened) during EN and LN events.

Vorhees (2006) and Syed et al., (2006) concluded that EN and LN events can have significant effects on weather patterns in southwest Asia. For example, anomalous warming of SSTs in the MC region during an LN event tends to increase convective activity over that region. Thus, deep ascent is enhanced and creates anomalous upper level divergence, from which there is then an equatorial Rossby-Kelvin wave response (Figure 14; cf. Ford 2000; Matsuno 1966; Gill 1980). During an EN event the reverse set of patterns and processes occur.

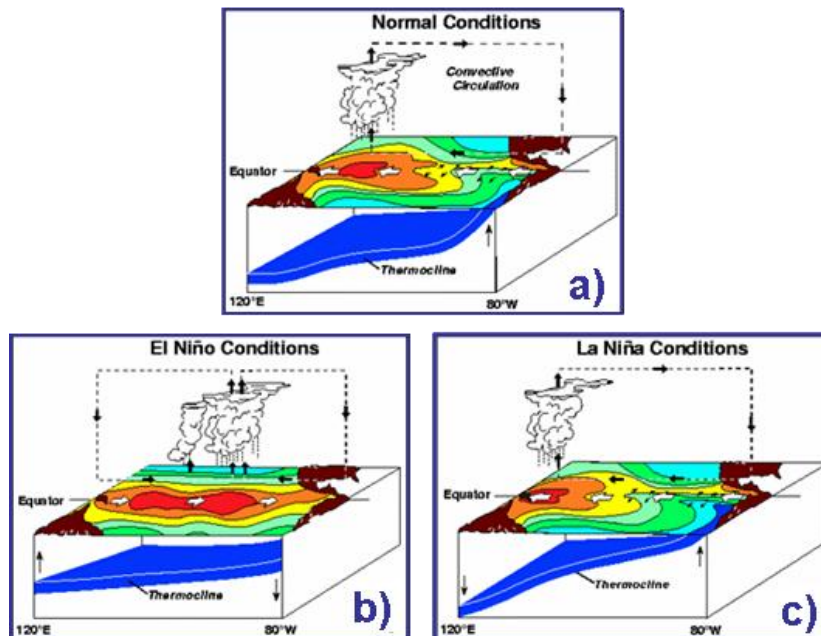


Figure 12. Schematic of tropical Pacific atmosphere and ocean during a) normal, b) El Niño, and c) La Niña periods. (From: Pacific Marine Environmental Laboratory (PMEL), available online from http://www.pmel.noaa.gov/tao/el_nino/nino-home.html#. Accessed September 2007).

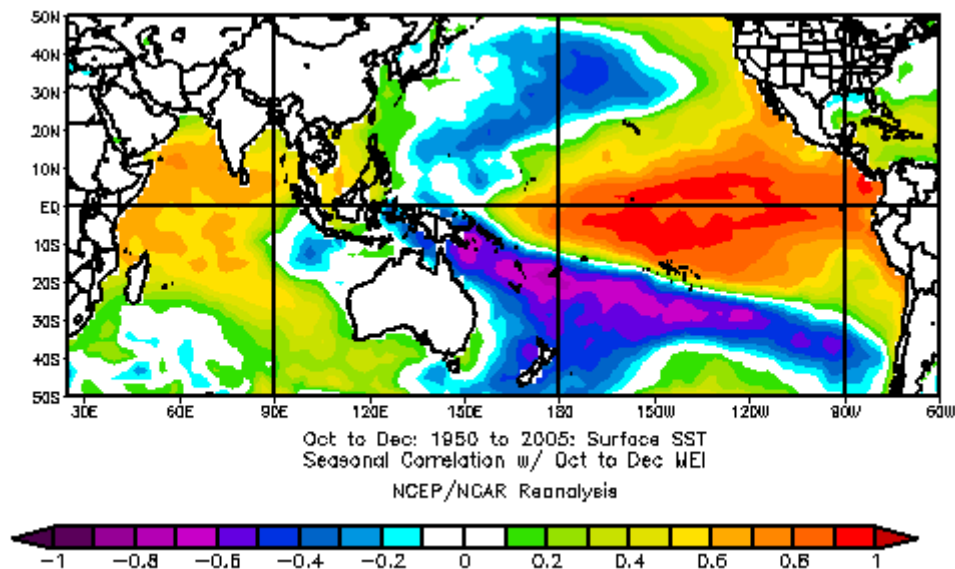


Figure 13. Correlation of SST with El Niño-La Niña Index (using Multivariate El Niño Southern Oscillation Index) for October-November. Figure created using NCEP reanalysis data and CDC web site. (From: <http://www.cdc.noaa.gov/Correlation/>, accessed September 2007).

The anomalous convection in the tropical Pacific Ocean triggers anomalous Rossby-Kelvin wave responses that extend into the NWIO and therefore should affect EDH. ENLN also effects the monsoon, the reader is referred to Ashok et al., (2003); Chiang and Sobel (2002) and Wainer and Webster (1996) for further information.

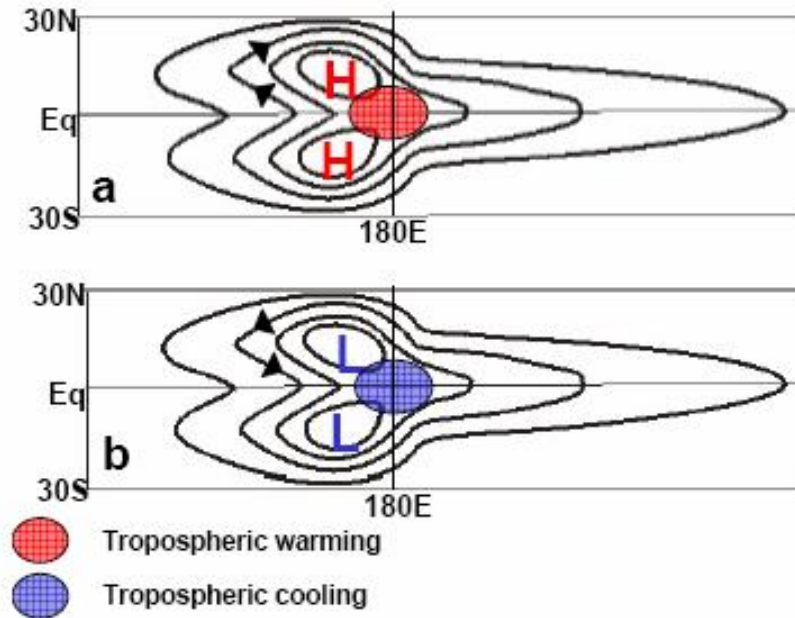


Figure 14. Schematic of the Rossby-Kelvin wave response to anomalous equatorial tropospheric (a) warming and (b) cooling. Contours show perturbation isobars. To the east of the forcing region, there is a ridge in (a) and a trough in (b) associated with the Kelvin wave response. To the west of the forcing region, there is a trough in (a) and a ridge in (b) associated with the Kelvin wave response. To the northwest and southwest of the forcing region, there are paired anticyclones in (a) and cyclones in (b) associated with the Rossby wave response. From: Ford (2000).

2. Indian Ocean Zonal Mode

With the benefit of an increasing observational data set across the IO and more realistic coupled atmosphere-ocean models, a new variation mode, the Indian Ocean Zonal Mode (IOZM), was identified in the late 1990s. This is an inter-annual mode of variability in SST across the IO which produces an

anomalous east-west temperature gradient with opposite SST anomalies (SSTAs) in the western and eastern tropical Indian Ocean. In the positive (negative) phase of the IOZM, the SSTAs are positive (negative) in the western tropical IO and negative (positive) in the eastern tropical IO. (Figure 15).

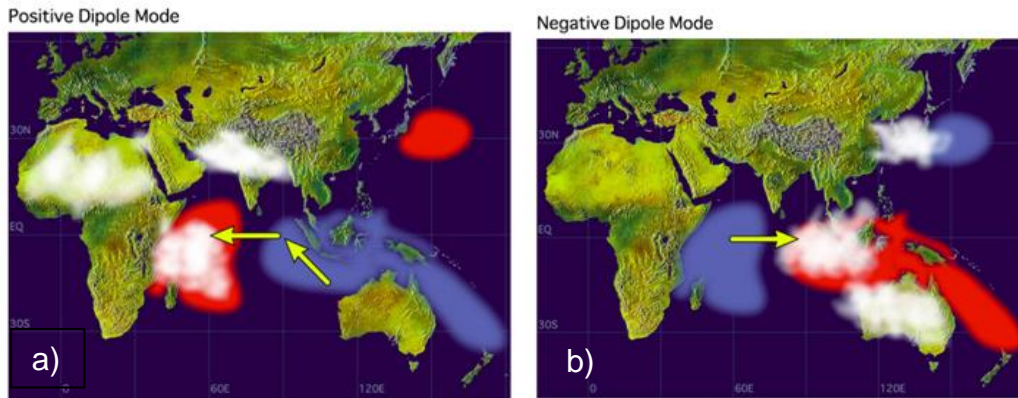


Figure 15. Schematic diagrams of characteristic IOZM anomalies. SST anomalies (positive (negative) SSTA in red (blue)) during (a) positive IOZM phase and (b) negative IOZM phase. White patches indicate anomalously strong convective activity. Anomalous wind directions are indicated by arrows. (From: <http://www.jamstec.go.jp/frsgc/research/d1/iod/IOD1.html> accessed September 2007)

Initial papers by (Saji et al., 1999) and (Webster et al., 1999) proposed a mechanism for the IOZM and their findings are outlined below. LTM tropical SSTs in the eastern IO are slightly warmer than in the western and central regions. This SST gradient induces, through air-sea interactions, a west to east pressure gradient force that contributes to an equatorial Walker circulation as illustrated in Figure 11.

A positive IOZM phase initiates in May-June with negative SSTAs and southeasterly wind anomalies in the equatorial eastern IO. Through the summer months the cold anomalies in the easterly IO intensify and extend westward along the equator and the easterly wind anomalies strengthen. Positive SSTAs develop in the western and central equatorial regions of the IO, especially off the coast of E Africa between northern Somalia and northern Mozambique. There

are also convection and precipitation anomalies, notably an increase in precipitation over equatorial E Africa and a reduction over the MC. The net result is a set of west-east dipoles in IO oceanic and atmospheric anomalies (e.g., in SSTAs, Figure 15). Key elements of the eastern IO atmospheric and oceanic feedback mechanism are outlined in the flow diagram in Figure 16.

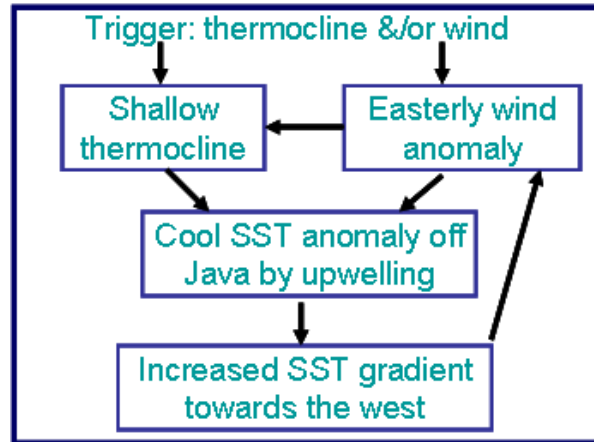


Figure 16. Ocean-atmosphere feedbacks in the eastern Indian Ocean controlling the growth of the positive phase IOZM. (After: Meyers et al., 2007).

The maximum SSTA dipole normally forms by or during October, at the same time that low level wind anomalies are most easterly. After October, the anomalies gradually weaken and conditions slowly return to a more normal boreal winter state. The effects of an IOZM event are rarely evident after December (Saji and Yamagata, 2003). IOZM anomalies in the surface factors that affect are large enough that we hypothesize that there should be significant impacts of the IOZM on EDH in the IO.

Since the initial studies of the IOZM, there has been considerable research into both the atmospheric and oceanic components and mechanisms of the IOZM and lively discussions on how independent the IOZM is from ENLN. For this study it suffices to state that climate variations, by their very nature, affect and influence other climate variations, often by complex and poorly

understood mechanisms. However, it is necessary to investigate each component separately before trying to link all climate variations together. Some of the IOZM mechanisms are very similar to the ENLN response in the IO. However, IOZM phases do not always occur at the same time as their equivalent ENLN events and therefore ENLN and IOZM are considered by some researchers to be largely independent of each other. The reader is referred to Ashok et al., (2001); Ashok et al., (2003); Ashok et al., (2004); Behera et al., (2006); Krishnamurthy and Kirtman, (2003); Meyers et al., (2007) for further information on the relationship of ENLN and IOZM.

3. North Atlantic Oscillation

Like ENLN, the North Atlantic Oscillation (NAO) has been extensively researched and is one of the most frequent and significant variations in the northern hemisphere (Hurrell 2003). It can occur at any time throughout the year but it tends to be most intense in the boreal winter. The NAO is essentially an oscillation of atmospheric mass between the Azores High and the Icelandic Low, and its influence is known to extend into SW Asia, Vorhees (2006) and Syed et al., (2006). Schematic depictions of the positive and negative phases are shown in Figure 17 and the reader is referred to LaJoie (2006) and Vorhees (2006) for further background on the NAO.

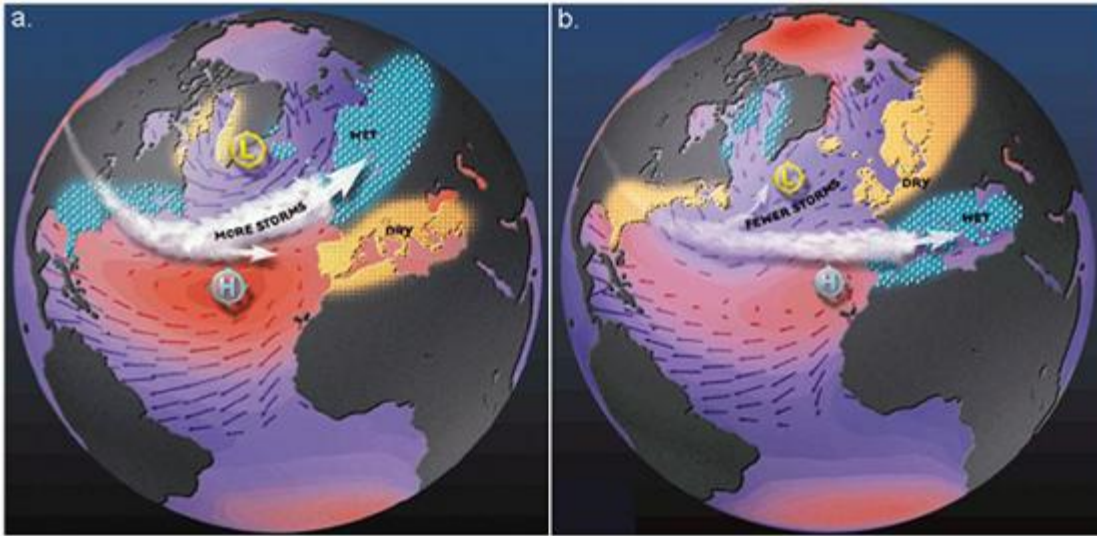


Figure 17. Schematic depiction of the NAO phases: (a) positive and (b) negative. (From: <http://eesc.columbia.edu/NAO/>, accessed September 2007).

In the negative phase, the North Atlantic mid-latitude storm track is generally located further to the south than normal and passes over southern Europe and the Mediterranean Sea, bringing increased precipitation to these areas. Conversely, the positive phase normally brings drier conditions to southern Europe. The impacts of NAO on SW Asia are examined by Vorhees (2006) and Syed et al., (2006). These studies concluded that the effects of a single NAO phase tend to change from autumn to winter. For example, in a positive phase during autumn and winter, Vorhees (2006) found that temperatures tend to be cooler in SW Asia, but precipitation tends to be anomalously high in the autumn and low in the winter. Our area of interest is largely farther south of SW Asia. However, based on these prior studies, we hypothesize that the NAO will have some effect on EDH in the northern portion of our study area (see Figure 7).

F. EXISTING EVAPORATION DUCT HEIGHT CLIMATE PRODUCTS

The existing EDH climatology in use by the U.S. Navy is contained within the Historical Electromagnetic Propagations Conditions database (Patterson, 1987). The EDH portion of this database, known as DUCT63, was derived from 15 years (January 1970 to December 1984) of marine observations 'assembled from ship logs, ship weather reporting forms, published ship observations, automatic buoys, teletype reports, and card decks purchased from foreign meteorological services' (Patterson, 1987). These observations were obtained from the National Climatic Data Center Standard Tape Deck-11 database, which was a precursor to what is now known as the International Comprehensive Ocean-Atmosphere Data Set (ICOADS). In this study, this present U.S. Navy EDH climatology will be referred to as the *existing EDH climatology* or simply the *existing climatology*.

The EDH values for DUCT63 were computed from the marine meteorological observations using the Paulus-Jeske (PJ) ED model (Patterson 1987). It is important to note that the PJ model applies an 'open-ocean correction' such that if the air temperature is more than 1° C higher than the SST, the air temperature measurement is assumed to be in error due to thermal contamination and is set equal to SST +1 °C (Patterson 1987). This assumption has very important implications for the final EDH climatology results, especially in coastal regions where such air-sea temperature differences greater than +1 °C can occur due to warm air advection from nearby land areas.

Monthly LTM values and frequency of occurrence histograms of EDH are available in DUCT63 for a gridded set of numbered 10° by 10° boxes, known as Marsden squares. Only those Marsden squares that contain ocean areas and that had at least 100 valid observations per month were included in the final EDH climatology in order to obtain meaningful statistics and to reduce the effects of spurious observations (Patterson 1987). For the Marsden squares that cover the IO, the number of observations per square per month varies from ~100 to more

than 3000. Much of this data was obtained along major shipping routes and thus may not always accurately represent the average EDH conditions across the entire Marsden square.

The DUCT63 EDH climatology database is available from within AREPS. Users can select any desired Marsden square and view monthly distributions for night and/or day. Figure 18 shows the location of the Marsden squares. Figure 19 is an example of data available for the central Arabian Sea Marsden square.

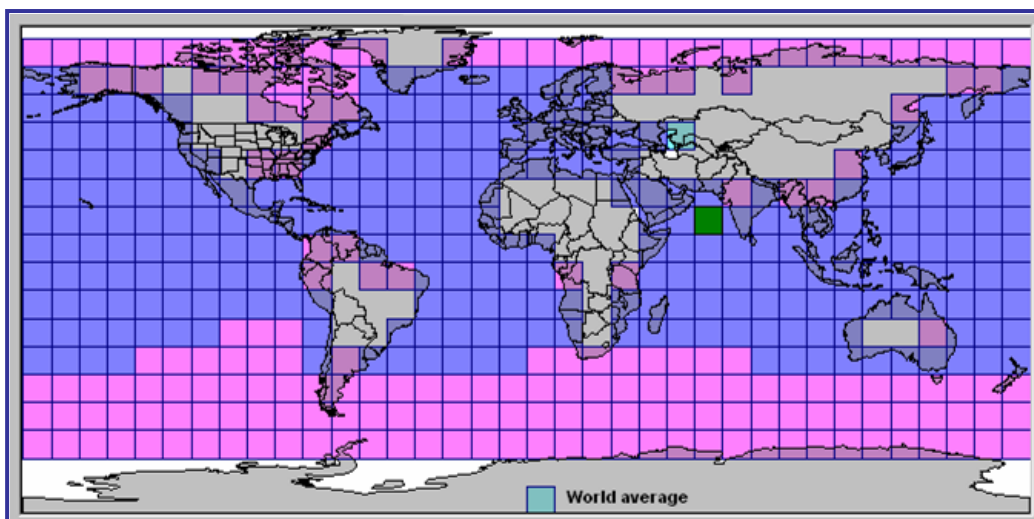


Figure 18. Distribution of 10x10 degree boxes (Marsden squares) for which long term mean climatological EDH values are available, one EDH value per square per month, from the existing EDH climatology used the U.S. Navy and Royal Navy. The dark blue (magenta) boxes indicate the locations for which values are (are not) available. The green box indicates the central Arabian Sea box for which the EDH values are shown in Figure 19. (From: AREPS, Space and Naval Warfare Systems Center: <http://areps.spawar.navy.mil/>, accessed September 2007).

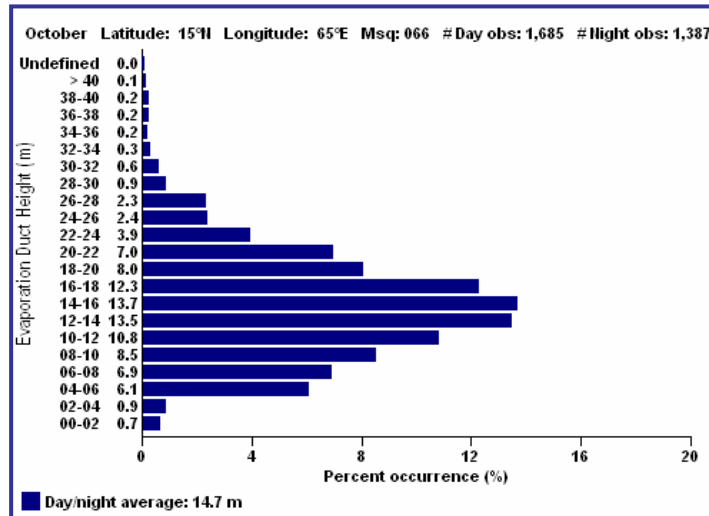


Figure 19. Histogram of EDH versus percent occurrence for October in central Arabian Sea box indicated in Figure 18, an example of the existing EDH climatology. (From AREPS, Space and Naval Warfare Systems Center: <http://areps.spawar.navy.mil/>, accessed September 2007).

Smart climatology methods have the potential to substantially improve the existing evaporation duct climatology products. These methods include use of dynamically balanced reanalysis data, compositing of reanalysis fields according to major climate variations and regimes, climate forecasting, and other methods described in Chapter I, section C1.

G. MOTIVATION AND DESIGN OF THIS STUDY

The motivation behind this research is to provide operationally useful information on: (1) climate scale temporal and spatial variability in EDH; and (2) the impacts of these variations on surface sensor performance in the Indian Ocean and nearby seas. This study also seeks to provide a ‘proof of concept’ for updating global EDH climatologies. This study investigates seasonal and anomalous variations in the air-sea boundary layers of the equatorial and northern IO, and nearby seas, and their effects on electromagnetic propagation

via EDH variations. It focuses on areas of operational interest and utilizes smart climatology analysis methods (refer to Chapter I, section C1), a modern reanalysis dataset and a state-of-the art EDH model.

The methods and data used in this study are discussed in Chapter II. Chapter III presents our main results and examples of climatological sensor performance surfaces. Chapter IV concludes with a summary of results and provides suggestions for future research.

THIS PAGE INTENTIONALLY LEFT BLANK

II. DATA AND METHODS

A. DATA

1. NCEP Reanalysis Dataset

The primary climate data used in this analysis is the National Center for Environmental Prediction (NCEP) Reanalysis-1 six-hourly surface flux data, (Kalnay et al., 1996). Data was acquired from the Cooperative Institute for Research in Environmental Sciences/Climate Diagnostics Center (CDC) and Physical Science Division, Earth System Research Laboratory, National Oceanic and Atmospheric Administration, Boulder, Colorado, from their web site at <http://www.esrl.noaa.gov/psd/> (accessed September 2007). This reanalysis data is generated using historical observations and a fixed forecast-analysis system, with a T62 global atmospheric model. Six-hourly reanalysis data is available from 1948 to the present day, and global atmospheric fields are provided for a variety of atmospheric factors. The spatial coverage is on a Gaussian grid with 192 x 94 grid points from 88.543°N to 88.543°S, which provides data with an equivalent horizontal resolution of ~210 km. Figure 20 shows the study area with an overlay of the NCEP reanalysis Gaussian grid and the areas of interest highlighted.

EDH is calculated from near-surface atmospheric parameters at known heights and sea surface temperature. A list of these factors and their heights is given in Table 1, which also includes details of subsequently calculated data fields.

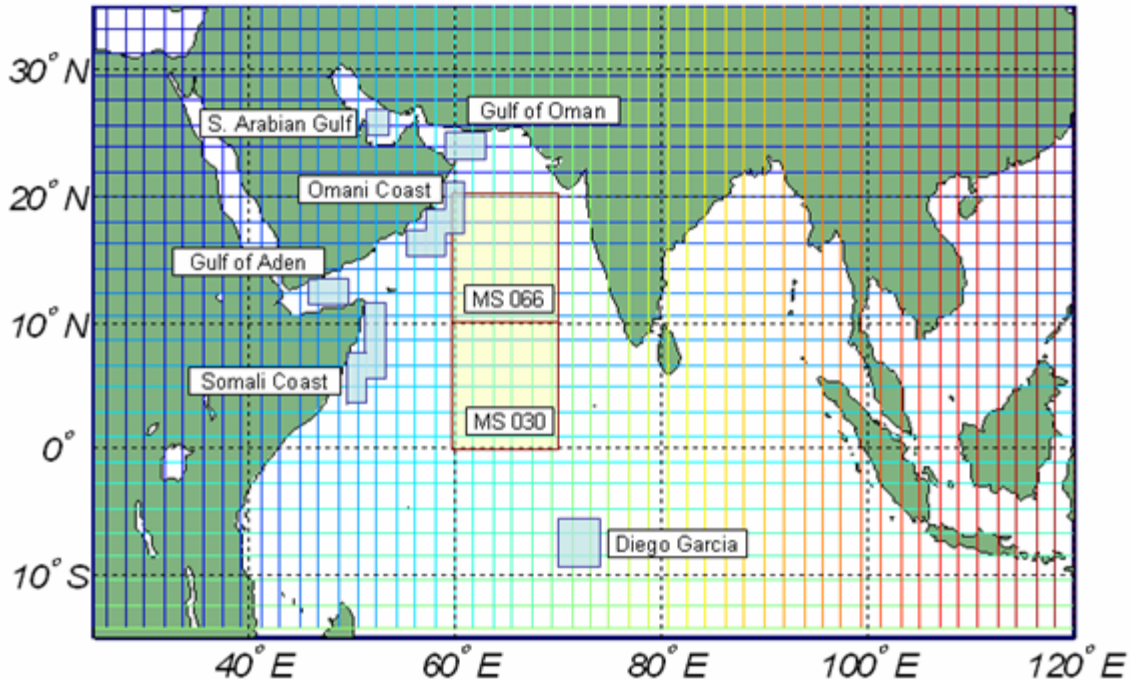


Figure 20. Indian Ocean study area with an overlay of the NCEP Gaussian grid. Areas of interest for this study are shaded blue and existing climatology boxes are shaded yellow.

Reanalysis output factor fields are classified into four classes, dependent on the extent to which they have been influenced by observations and/or model (Kalnay et al., 1996). All six primary data fields used in our analysis are classified as category B. This means that whilst direct observational data influences the analysis output, the model also has a strong effect on the factor value. As such, the model provides and ensures dynamical balance between all the surface flux data.

NCEP reanalysis-1 skin temperature data was used to provide sea surface temperature (SST) fields. Over open ocean areas the skin temperature uses the initial SST boundary conditions. This reanalysis used a combination of weekly optimal Interpolation SST reanalysis (Smith and Reynolds, 2003) (Reynolds and Smith, 1994) from 1982 to present day and the United Kingdom Meteorological Global Sea Ice Coverage and SST (GISST) data prior to that. Both SST reanalyses use ICOADS data based on ship observations, buoys, drifters etc;

and the more modern reanalysis includes satellite SST observations. The use of satellite data has been shown (Kalnay et al., 1996) to reduce SST errors from ~1.3 °C to 0.3-0.5 °C. Weekly SST data fields are interpolated to daily values, which are used for the four runs throughout the day.

Table 1. Primary factors used in this study and key factors calculated in this study. The primary factors were obtained from the NCEP reanalysis 1 data set.

PRIMARY FACTORS	Reanalysis Height (m)	Units	Abbreviation
Air Temperature	2m	°C	TA
Skin Temperature	Surface	°C	
Specific Humidity	2m	g/kg	SH
u component of wind	10m	ms ⁻¹	
v component of wind	10m	ms ⁻¹	
Sea Level Pressure	Surface	hPa	SLP
CALCULATED FACTORS			
Wind Speed	10m	ms ⁻¹	WS
Air-Sea Temperature Difference	2m	°C	ASTD
Relative Humidity	2m	%	RH
Evaporation Duct Height	NA	m	EDH

Although assimilation of satellite data significantly improves the accuracy of the model analyses, it only began to be incorporated from the late 1970s onwards. Thus, it may seem plausible that an ideal dataset for calculating an EDH climatology would include only data from after 1982, when SST and other factors improved in accuracy. However, for this study such a dataset would only include 25 years of data and would not include an equal representation of several major climate variations (e.g., EN and LN events, positive and negative IOZM

events). Thus, we chose a data set covering the 37 years from 1970 to 2006 to encompass a balance of EN and LN years and to enable a more robust smart climatology analysis (cf. Ford 2000; Hildebrand 2001; Vorhees 2006).

B. CLIMATE INDICES

1. Multivariate ENSO Index (MEI)

Over the last several decades, there has been, and there continues to be, extensive research into the El Nino, La Nina, and the Southern Oscillation (also known, collectively, as El Nino–Southern Oscillation, or ENSO) phenomenon, and many valid indices have been developed to measure the oscillations associated with ENLN. They are generally based on a variety of observed meteorological and oceanographic factors, and provide different methods of classifying ENLN events and their relative strengths. A brief historical overview of the various ENLN indices are found in Ford (2000) and Hildebrand (2001).

Our index of choice is the Multivariate El Nino Southern Oscillation Index (MEI) which incorporates a greater range of data than other indices using six key observable factors (sea level pressure (SLP), u and v surface winds, SST, Ta and total cloudiness fraction of the sky) in the tropical Pacific. By incorporating a mixture of oceanographic and atmospheric factors it better reflects the coupled ocean-atmospheric system and is less vulnerable to any data anomalies.

An explanation of methodology is summarized by Wolter (1987) at www.cdc.noaa.gov/people/klaus.wolter/MEI/index.html, (accessed August 2007) as:

After spatially filtering the individual fields into clusters (Wolter, 1987), the MEI is calculated as the first unrotated Principal Component (PC) of all six observed fields combined. This is accomplished by normalizing the total variance of each field first, and then performing the extraction of the first PC on the covariance matrix of the combined fields (Wolter et al., 1993). In order to keep the MEI comparable, all seasonal values are standardized with respect to each season and to the 1950-93 reference period.

MEI values are computed for bimonthly time periods (January-February, February-March, etc.). A graphical display of the index, 5 month smoothed, is shown in Figure 45. For further background information, the reader is referred to Vorhees (2006) and LaJoie (2006).

2. Dipole Mode Index (DMI)

The primary means for measuring the Indian Ocean Zonal Mode (IOZM) is the Indian Ocean Dipole Mode Index (DMI) as defined by (Saji et al., 1999) . This is essentially a measure of the SST difference between a western tropical IO box and an eastern tropical IO box, with the boxes located at 10°N-10°S, 050°-070°E and 0-10°S, 090°-110°E. The index presented in (Saji et al., 1999) utilized the GISST version 2.3b dataset.

For our study, we developed our own version of the DMI using a monthly averaged time series of SST for each of the two boxes based on NCEP reanalysis six-hourly skin temperature data, but excluding NCEP grid boxes which encompass land. The resulting SST time series for each box was de-trended using a linear de-trend function, then smoothed using a five month running mean, after which the time series were filtered to remove periodicities greater than seven years. The difference between the resulting SST time series for the east and west boxes was then found, and the resulting difference time series normalized using the standard deviation of the time series.

The resulting DMI time series is plotted in Figure 45 in Chapter III. Positive (negative) DMI values equate to a positive (negative) IOZM phase (i.e., cold (warm) SST near the maritime continent and warmer (cooler) SST in the western tropical IO). The DMI is a simple index for a complex atmospheric and oceanographic variation. More recent indices use differing combinations of factors, for example, u-surface wind, outgoing long wave radiation, and SST. Further information can be found at the Indian Ocean Dipole homepage <http://www.jamstec.go.jp/frsgc/research/d1/iod/IOD1.html> (accessed September 2007).

3. North Atlantic Oscillation Index (NAOI)

There are a number of different indices that define the phase and intensity of the North Atlantic Oscillation (NAO). The reader is referred to section E3 of Chapter I for further details on the oscillation. Simple indices measure the gradient of SLP across the region. The NAO index (NAOI) for this study is a more rigorous monthly index, which utilizes an empirical orthogonal function analysis technique and is maintained by the Climate Prediction Center. The techniques involved in producing this index are beyond the scope of this paper, and are presented in Barnston et al. (1987).

C. METHODS

1. EDH Computation

Six-hourly values of T_a , SST, SLP, specific humidity, and wind speed (derived from the u and v components) were used to compute six hourly values of EDH for all ocean grid boxes throughout the extended area using the NPS bulk evaporation duct model). This model has been compared to the PJ model and found to provide more accurate estimates of EDH (Frederickson et al., 2001, Frederickson et al., 2003).

Reanalysis values at a given grid point are the average of data over the whole surrounding grid box. Thus, if a grid box encompasses both land and sea, then the reanalysis values for the box will reflect a combination of land and sea data. In other words, the data for these boxes is intended to represent the box as a whole, and thus may not provide a clear distinction between conditions over land versus those over sea. This is particularly significant for determining the SST fields since they are derived from the skin temperature reanalysis fields. Thus the values for grid boxes which encompass both land and sea areas reflect a mixture of SST and land skin temperature data. Therefore, to ensure that EDH

was calculated from data representing only sea conditions, a masking was applied to exclude data from land areas. Figure 21 shows which grid boxes that represent only sea areas (blue shaded area).

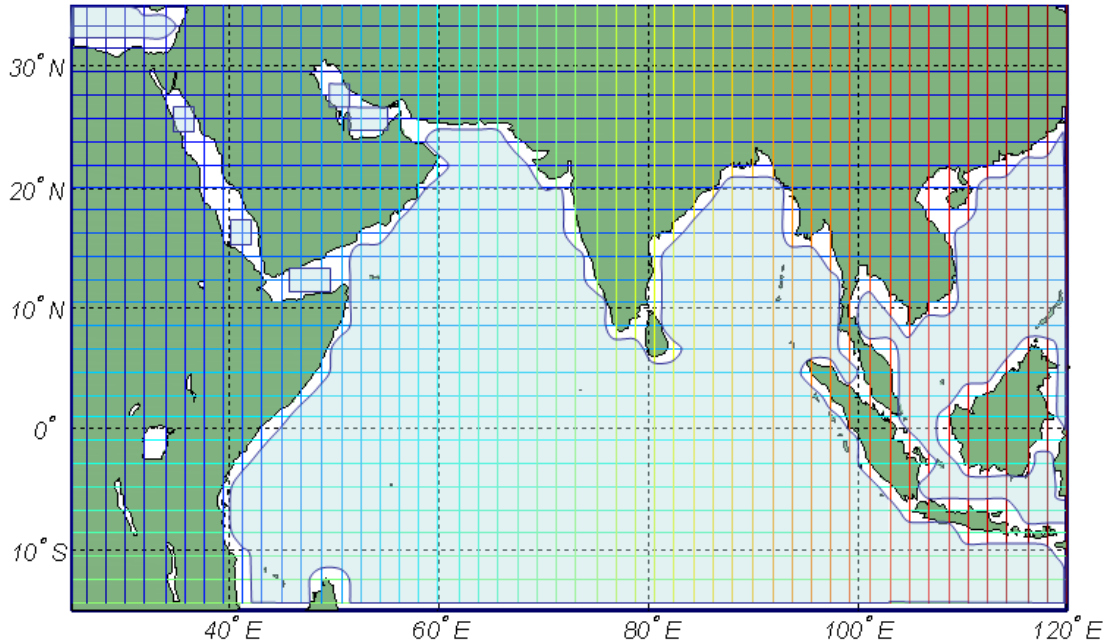


Figure 21. Masking of land: EDH calculated only for blue shaded grid boxes.

2. Understanding EDH and its Associated Factors

Mean monthly values of EDH and all its associated factors were calculated from the six-hourly values and then plotted in a map format.

A preliminary explanation of EDH variability was formed based upon how each of the factor fields changed and a knowledge of its influence on EDH. To aid this understanding, a correlation analysis of EDH with its factors was completed for the areas of operational interest. The formula used for correlation is:

$$\text{Correlation value} = \frac{\sum(xy)}{\sqrt{(\sum(x^2)(y^2))}}$$

where x and y are the values to be correlated with their time means subtracted. This is the same correlation used by the Physical Science Division of CDC in

their web based climatology analysis tools at:
<http://www.cdc.noaa.gov/Correlation/> and
<http://www.cdc.noaa.gov/ClimateIndices/> (accessed September 2007).

3. Investigating the Effects of Climate Variations on EDH

In order to investigate the effects of IOZM and ENLN on EDH in the IO, various composite analyses were conducted. The composite for any given variable is the mean of the members of the composite (e.g., mean EDH during the five strongest EN events for the October-November-December (OND) season, with the EN events determined from the MEI data). Further analysis was conducted using composite anomaly fields that show the difference between the composite and the LTM, with the EDH anomaly field being equal to the LTM subtracted from the composite. The anomalies help identify the regions impacted by climate variations.

The years for which composites were calculated were selected based on the 1970-2006 values of the climate variation indices (e.g., MEI, DMI, NAOI). The five most extreme events were chosen for each phase of each index, following the methodology used by LaJoie (2006).

The OND season was selected as the focus season for ENLN compositing based on the results from previous smart climatology studies in the region; in particular, the relatively large impacts of ENLN in the IO region during OND, and the tendency for a large change in the response to ENLN events from OND to January-February-March (Vorhees 2006; LaJoie 2006). In addition, OND is a season in which IOZM events tend to have relatively strong impacts on the IO region. Thus, the choice of OND for the ENLN composites allowed us to make direct comparisons between ENLN impacts and IOZM impacts. The focus seasons for our IOZM composites are discussed in Chapter III, where we also present our results from calculating the DMI for this study from reanalysis data.

Climate anomalies can show strong variations that clearly indicate dynamically understandable patterns. However, they can also show weak and inconsistent patterns that are difficult to interpret. Such patterns often indicate, upon closer analysis complex responses to climate variations that are important to unravel. Both strong and weak anomalies can provide insight into the phasing of the responses, whether there is asymmetry in the different phases of the variations, and the dynamical processes that underlie the anomalies. In general, the anomalies help reveal the patterns and processes that lie behind complex climatological variations and their impacts on EDH.

To further our understanding of climate variations on EDH, particularly in the areas of operational interest, correlation analyses were conducted using the CDC climate web site correlation tools at <http://www.cdc.noaa.gov/ClimateIndices/> (accessed September 2007). Correlations of EDH in the focus regions (Figure 20) with MEI, DMI and the CPC NAOI, with EDH lagging the climate variation index by zero, one, and two months, were completed for our focus areas (Figure 20). Correlations between EDH factors in the focus regions (Figure 20) and the three climate variation indices were also calculated using the tools at <http://www.cdc.noaa.gov/Correlation/> (accessed September 2007). These correlations of variables separated by long distance provide examples of climate system teleconnections. Such teleconnections can be very useful in determining the global scale climate dynamics that force regional changes, including changes in EDH in the NW IO and nearby seas.

D. SUMMARY

In this study, we have employed a smart climatology approach by:

1. using a state-of-the-art reanalysis data set
2. using a state-of-the-art ED model

3. applying statistical analysis methods (e.g., time series analyses, EDH-factor correlations, correlations of EDH and EDH factors with climate variation indices, teleconnection analyses) to determine the factors and dynamical processes that most strongly affect EDH variations
4. developing and applying climate indices
5. applying compositing techniques to develop conditional climatologies for different states of the climate system (e.g., EN, LN, positive IOZM, negative IOZM)
6. assessing the predictability of climate variation impacts on EDH
7. developing a state-of-the-art EDH climatology
8. developing prototype climatological sensor performance products (also known as climatological performance surfaces)

III. RESULTS

The evaporation duct height (EDH) is dependent upon a number of factors, primarily surface wind speed (WS), humidity and air-sea temperature difference (ASTD). As these factors vary due to oceanic and atmospheric fluctuations, EDH will also change. Section A of this Chapter presents our long term mean (LTM) seasonal values of EDH across the Indian Ocean (IO) basin, calculated using NCEP reanalysis data and the NPS ED model. Section B summarizes the main variations in the surface factors that affect EDH. These results provide insights into why EDH varies spatially and temporally, a topic that is examined further in section C in which correlation results for areas of particular operational interest are presented.

Section D compares our reanalysis EDH results to the existing climatology and to one year of buoy observations from the Arabian Sea. Section E presents correlation charts, which illustrate how various climate variations are correlated to equatorial EDH in the boreal autumn. From these it is surmised that EDH is influenced by local and global climate oscillations. In section F, a composite and anomaly analysis technique is used to investigate how EDH varies with some global variations. A correlation analysis of three primary climate variations (ENLN, IOZM and NAO) against EDH for the areas of interest is included. The final section applies the EDH results to illustrate their utility by developing climatological 'performance surfaces' for radar detection ranges.

A. EDH LTM

Figure 22 shows seasonal LTM EDH across the IO, and Figure 23 shows the same but for the NW IO. Appendix B contains monthly plots of EDH for the IO and NW IO areas.

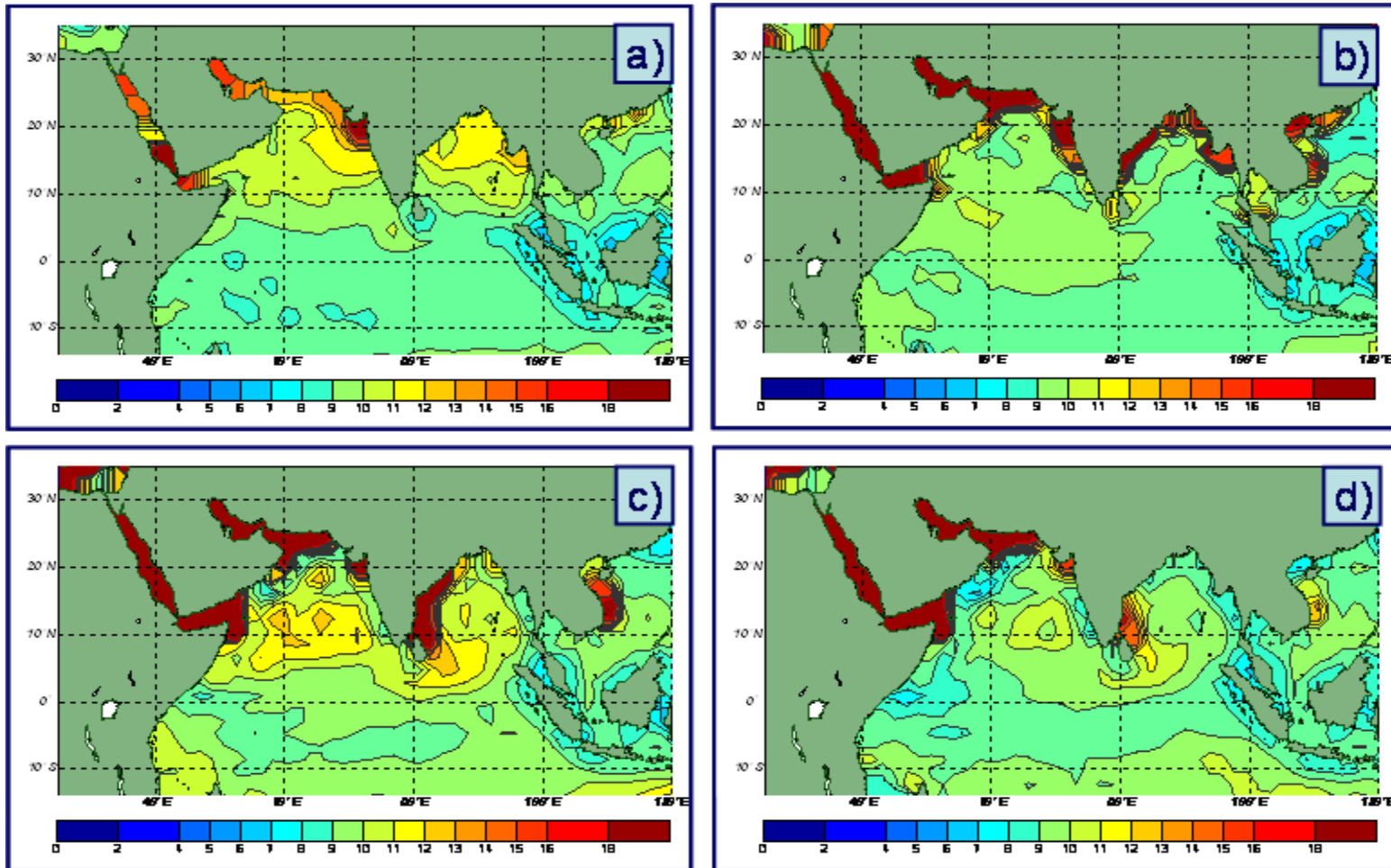


Figure 22. Seasonal LTM EDH(m) for the tropical and northern IO for: (a) November-December-January (NDJ); (b) February-March-April (FMA); (c) May-June-July (MJJ); and (d) August-September-October (ASO). Coastal values should be used with caution (see Chapter III, section A).

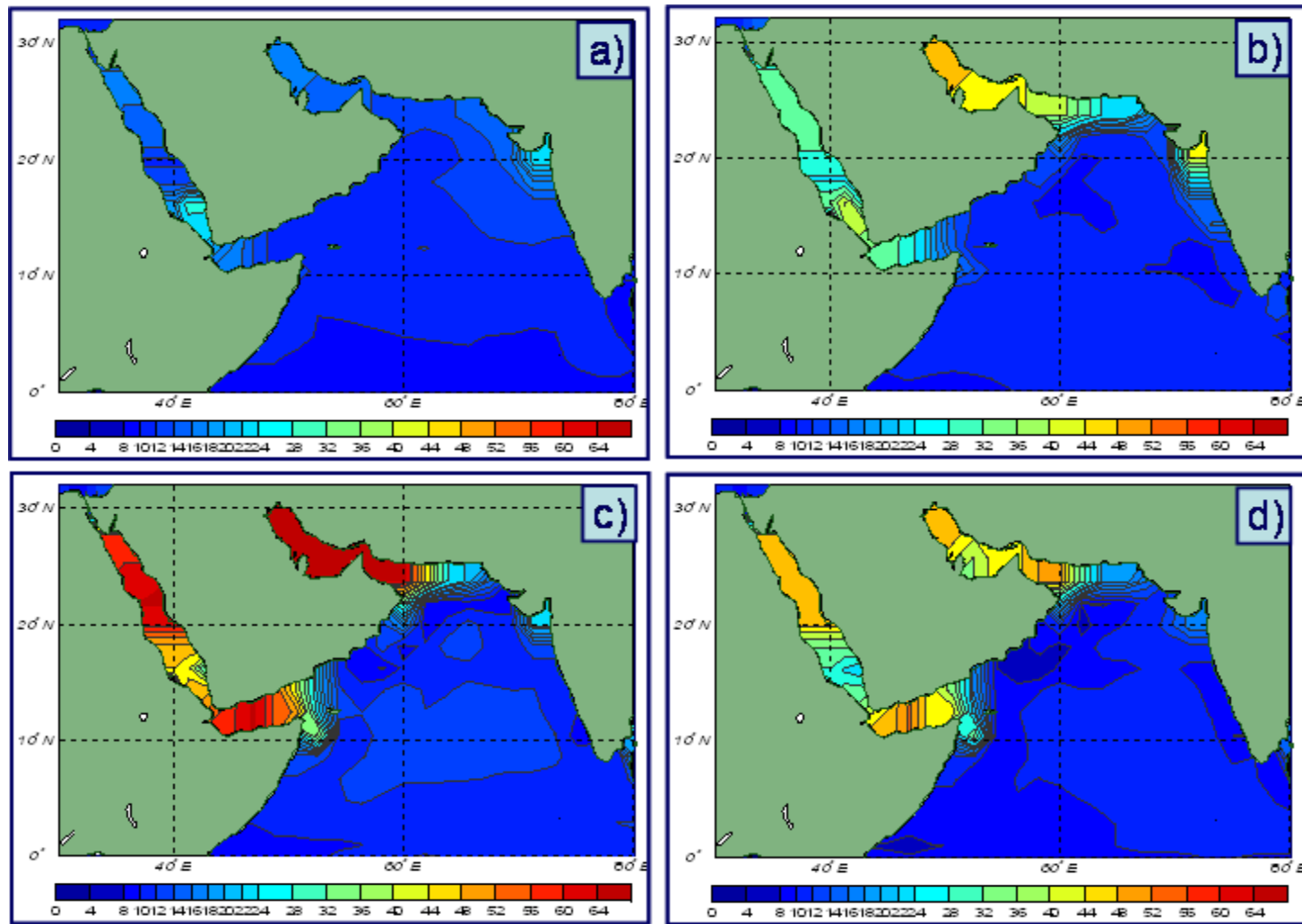


Figure 23. Seasonal LTM EDH(m) for the NW IO for: (a) NDJ; (b) FMA; (c) MJJ; and (d) ASO. Coastal values should be used with caution (see Chapter III, section A).

All the EDH Figures in this study use an approximation for grid boxes which encompass land and sea. The land masking, discussed in Chapter 2 section C1, means that EDH values are not calculated for many coastal sea areas (see Figure 21). For this study, we assumed that EDH in these coastal sea areas is similar to the EDH value in nearest seaward grid box, or the mean of the EDH values in the nearest seaward grid boxes. Figure 24 illustrates how, using this assumption, we calculated EDH in these coastal sea areas. The mapped outcome utilizing this approximation provides the reader with a clearer understanding of the large scale trends in EDH across the Indian Ocean and close to the coast. However, the EDH values near the coast should be interpreted with caution, since they are not directly calculated for these areas but instead are mapped to these areas from nearby sea areas. In addition, whilst the use of NCEP reanalysis data has a temporal resolution of six hours, it is not at a fine enough spatial resolution to provide insights into small scale coastal influences on EDH, such as land-sea breeze effects.

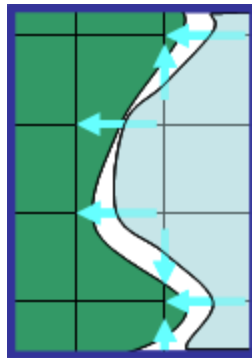


Figure 24. Mapping of sea grid points land-sea grid points. Compare to Figure 21. The blue arrows indicate the direction from which EDH values from seaward grid boxes are mapped to coastal sea areas containing both land and sea, and for which EDH is not directly calculated due to the influence of land (see Chapter II, section C1).

1. Equatorial Region

Figure 22 shows in the equatorial region, 0-10°S a predominantly zonal band of low EDH values ranging from seven to ten meters in height. This EDH

minima band moves southward, to 5-10°S, during the boreal winter and equatorward (0-7°S) in the summer. The minima band is slightly bowed, with the western IO and MC minima areas being more northerly than the central longitudes of the band.

The minimum values of EDH in the western IO occur off the African coast within the equatorial minima band during the summer and early autumn.

2. Arabian Sea

The Arabian Sea is a more complex region with significant coastal EDH variation, as seen in Figures 22 and 23. During NDJ there is a gradual increase in EDH to the northeast Arabian Sea. Spring brings a decrease in heights in the central region, which then become a local maxima by June-July-August, reaching monthly LTM heights of 14-15 m. As autumn approaches, the maxima region shifts eastward and reduces in intensity, and a band of lower EDH forms off the coasts of the Horn of Africa and the Arabian Peninsula. The intrusion of lower heights from the southwest slackens as winter approaches, leading back to the winter EDH gradient.

Along the Omani coast there is an increase in EDH from March to June, then the area becomes a local minimum from July to September. The Gulf of Cambay, to the north of Mumbai, is an area of increased EDH from October to June with the maximum heights (~40 m) occurring in April.

3. Gulf of Aden

In the Gulf of Aden (GOA) during NDJ the EDH is approximately 10-15 m. Heights increase rapidly during the spring in the western gulf and then occur further to the east. However, by June and until September the whole of the gulf has mean monthly EDH values above 60 m, and there is a steep EDH decrease to Socotra Island, at the exit of the gulf. During September-October the EDH quickly reduces back to winter values.

4. Gulf of Oman and South Arabian Gulf

In the Gulf of Oman (GOO) and Southern Arabian Gulf (SAG) EDH follows a similar cycle as in the GOA, with the SAG EDH increasing and then waning in height before the GOO. November to January EDH is 15-20 m; during February, EDH increases to 30-35 m in the SAG and slightly less in the GOO. However, by April heights in the SAG and GOO have risen to above 60 m, and remain high until September. During September and October heights decrease back towards winter values, with the SAG EDH decreasing before the GOO values.

B. LTM FACTORS

1. LTM Factors which Affect EDH

In this section we review the seasonal and spatial variations of the atmospheric and sea surface factors which influence the EDH in order to develop a basic understanding of the likely causes of the EDH variation discussed in part A.

a. Surface Wind

Figure 25 shows the surface wind regime over the annual cycle of seasons. The Arabian Sea and Horn of Africa are dominated by monsoonal wind reversals, whilst the equatorial trough and southeasterly trade winds are the key features further south. During the boreal winter, north to northeasterly monsoon winds affect the whole Arabian Sea, with a mean maximum speed of 8 ms^{-1} off the Somali coast. On average, the transition to summer conditions begins during April and southwesterly monsoon winds and the Somali Jet dominate until October. The southwesterly Somali Jet in the NW IO is a major feature of the boreal summer wind field and reaches a surface monthly mean maximum in June, with speeds up to 15 ms^{-1} .

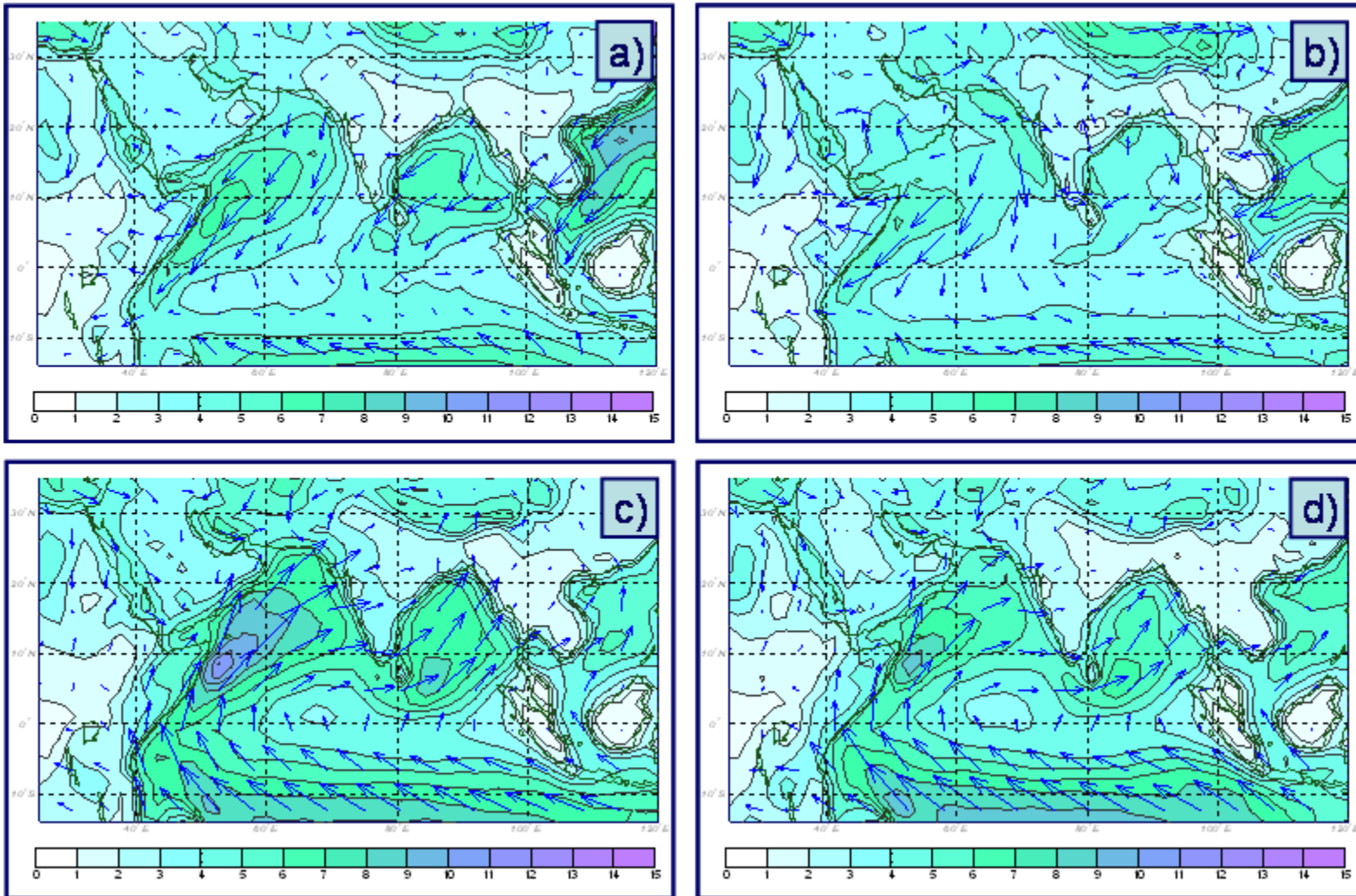


Figure 25. LTM wind speed (ms^{-1}) and direction for: (a) NDJ; (b) FMA; (c) MJJ; and (d) ASO.

During the boreal winter, the northeasterly monsoon winds over the NW IO feed into northwesterly winds south of the equator. These northwesterly winds converge with the southeasterly trades at the ITCZ at approximately 10 °S. During the boreal spring, the southeasterly trades strengthen and move towards the equator, reaching a mean strength of 10 ms⁻¹ by June.

b. Sea Surface Temperature

Figure 26 shows seasonal LTM SST variations. During the boreal winter the warmest SSTs occur in the equatorial region and slightly south of the equator in the western basin, off the coast of Tanzania. Across the Arabian Sea the temperature gradient is predominantly from northwest to southeast, such that GOA, Omani coast and GOO SSTs are approximately 4-5° less than at the equator. After the spring transition, southwest monsoonal winds cause upwelling of cooler water along the Somali coast, and along the Omani coastline by July-September. The western boundary current also helps advect this cooler water into the western Arabian Sea such that the western IO and Arabian Sea are on average approximately 3 °C cooler than at the same latitudes in the eastern IO. Evidence of this cooling associated with coastal upwelling and cool water advection persists through the autumn transition season, when the upwelling ceases, and into the winter.

All the seasonal (Figure 25) and monthly (not shown here) charts show a distinctive spatial oscillation or wave pattern in the northwest Arabian Sea. This is not investigated here; however, (Gill, 1983) hypothesizes that this is due to nonlinear effects in the western boundary current.

Temperatures in the SAG dip to 21-22 °C during the boreal winter and warm to 30-35 °C over the summer. Similarly high temperatures are also reached in the GOO. But in the GOA, SSTs only increase to 25-30 °C.

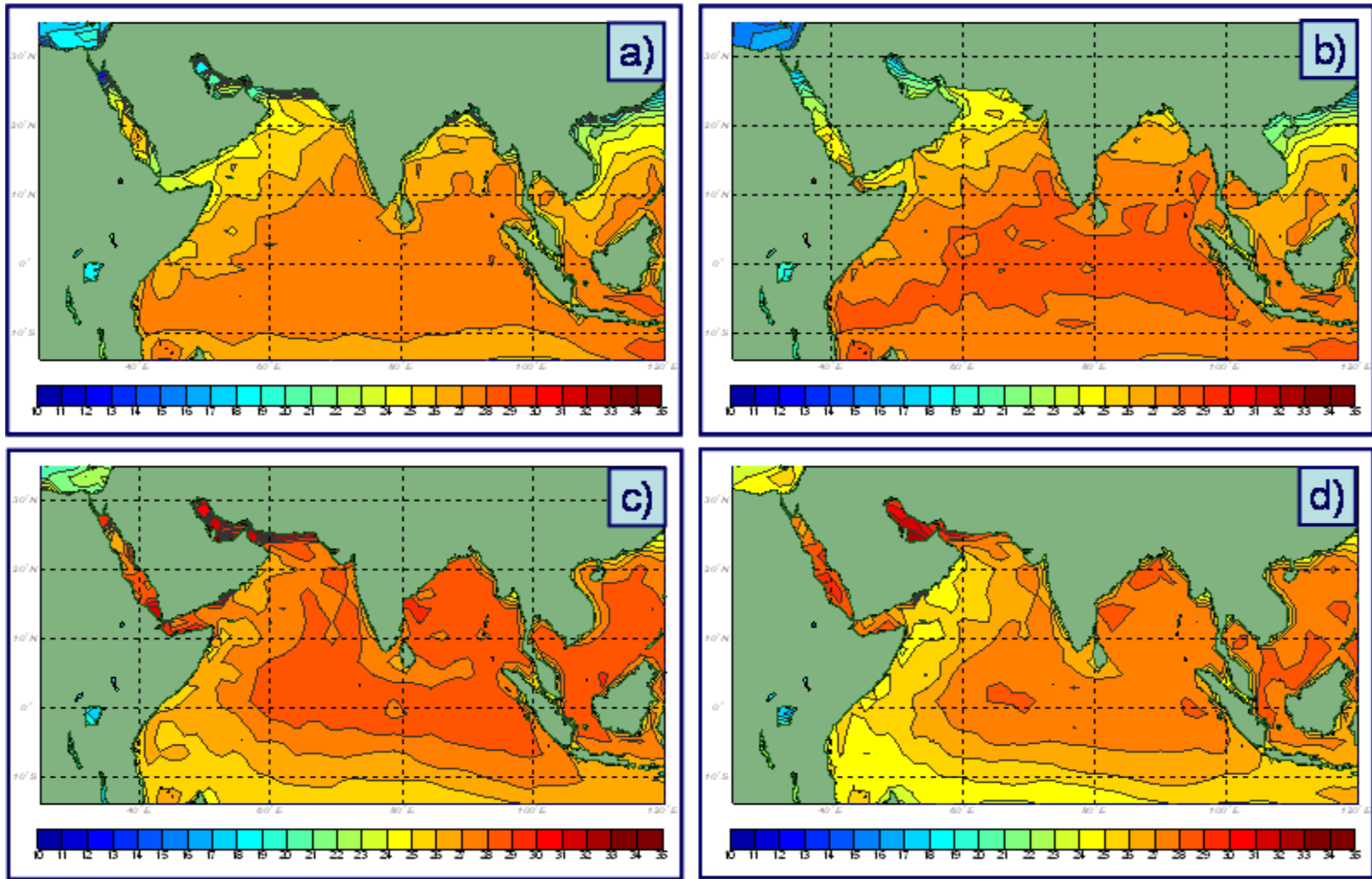


Figure 26. LTM SST ($^{\circ}\text{C}$) for: (a) NDJ; (b) FMA; (c) MJJ; and (d) ASO.

c. Surface Air Temperature and Air-Sea Temperature Difference

Figure 27 shows the seasonal air temperature (T_a) variation throughout the region. Over the open ocean, air temperatures are generally a degree or more cooler than the SST. However, as surrounding landmasses respond to the annual heating cycle, coastal ocean regions may be affected by the offshore advection of inland temperatures. This is particularly significant during the boreal winter in the Arabian Sea, Arabian Gulf, GOO and GOA, where mean surface T_a falls and ASTD becomes negative (Figure 28).

ASTD charts (Figure 28) are presented due to their significant effect on EDH (Chapter I, section B2). When ASTD is positive, EDH may increase dramatically, particularly at low wind speeds and for moderate to lower humidity conditions. Figure 28 shows that in the open ocean, conditions are generally unstable (i.e., SST greater than T_a). Particularly unstable surface conditions are evident in the equatorial region. This stretches across the IO basin and is associated with light wind areas.

From May to September the western boundary areas of the IO and Arabian Sea are less unstable and occasionally become stable, in association with high wind speeds and coastal upwelling. Increased wind speeds cause more ocean mixing, SST reduction, and an increase in ASTD. ASTD in the gulfs is generally positive over the boreal summer months.

d. Relative Humidity

Figure 29 shows seasonal RH charts throughout the region. Over the ocean and gulfs, moisture content is highly influenced by the wind direction and to a lesser extent wind speed. Moisture advection is better represented using specific humidity (SH) charts. However, as EDH generally has a stronger correlation to RH, this paper concentrates on RH. It should be noted that whilst SH is not presented, it has been calculated, plotted and used in our analyses.

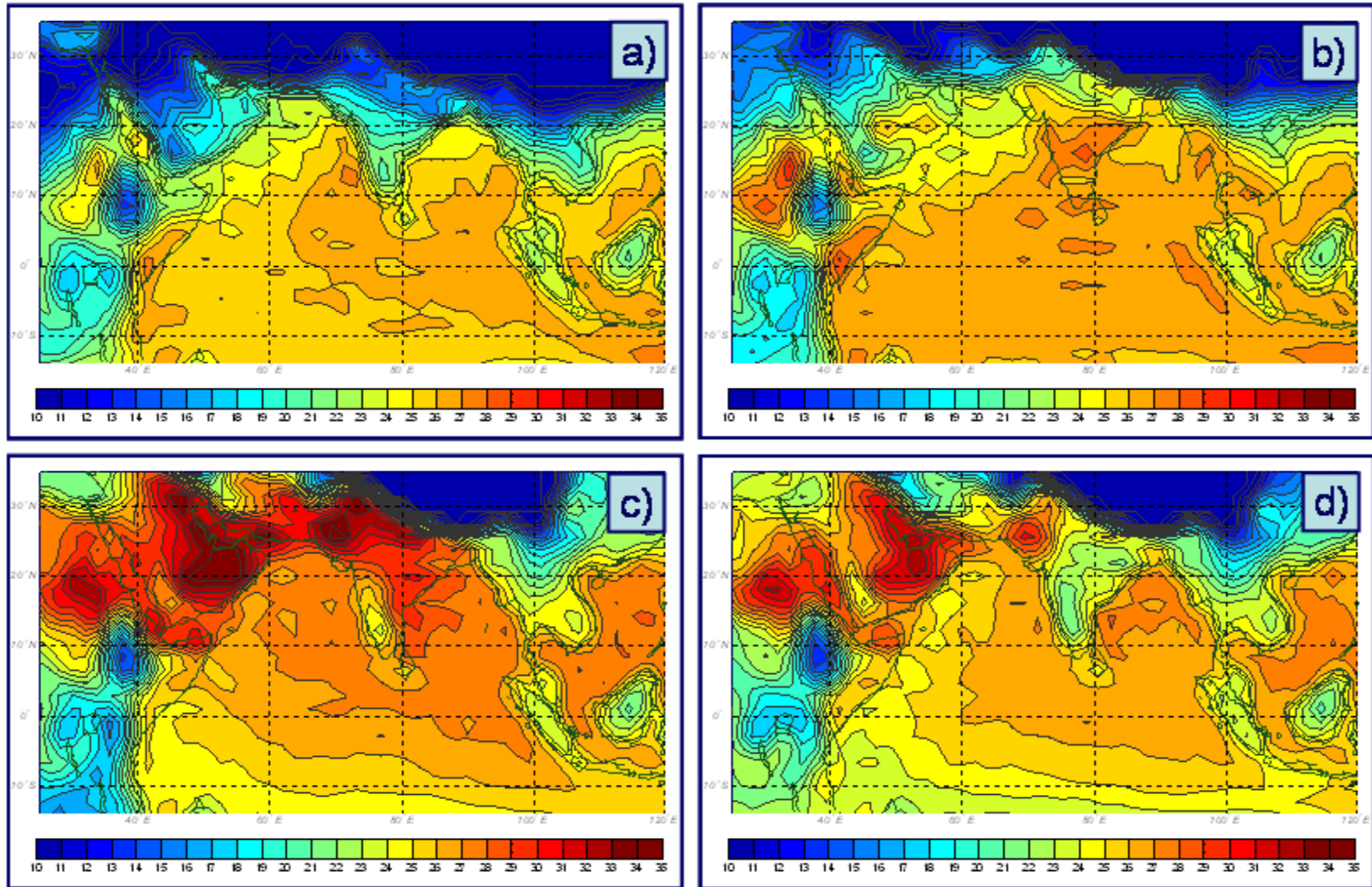


Figure 27. LTM air temperature (°C) for: (a) NDJ; (b) FMA; (c) MJJ; and (d) ASO

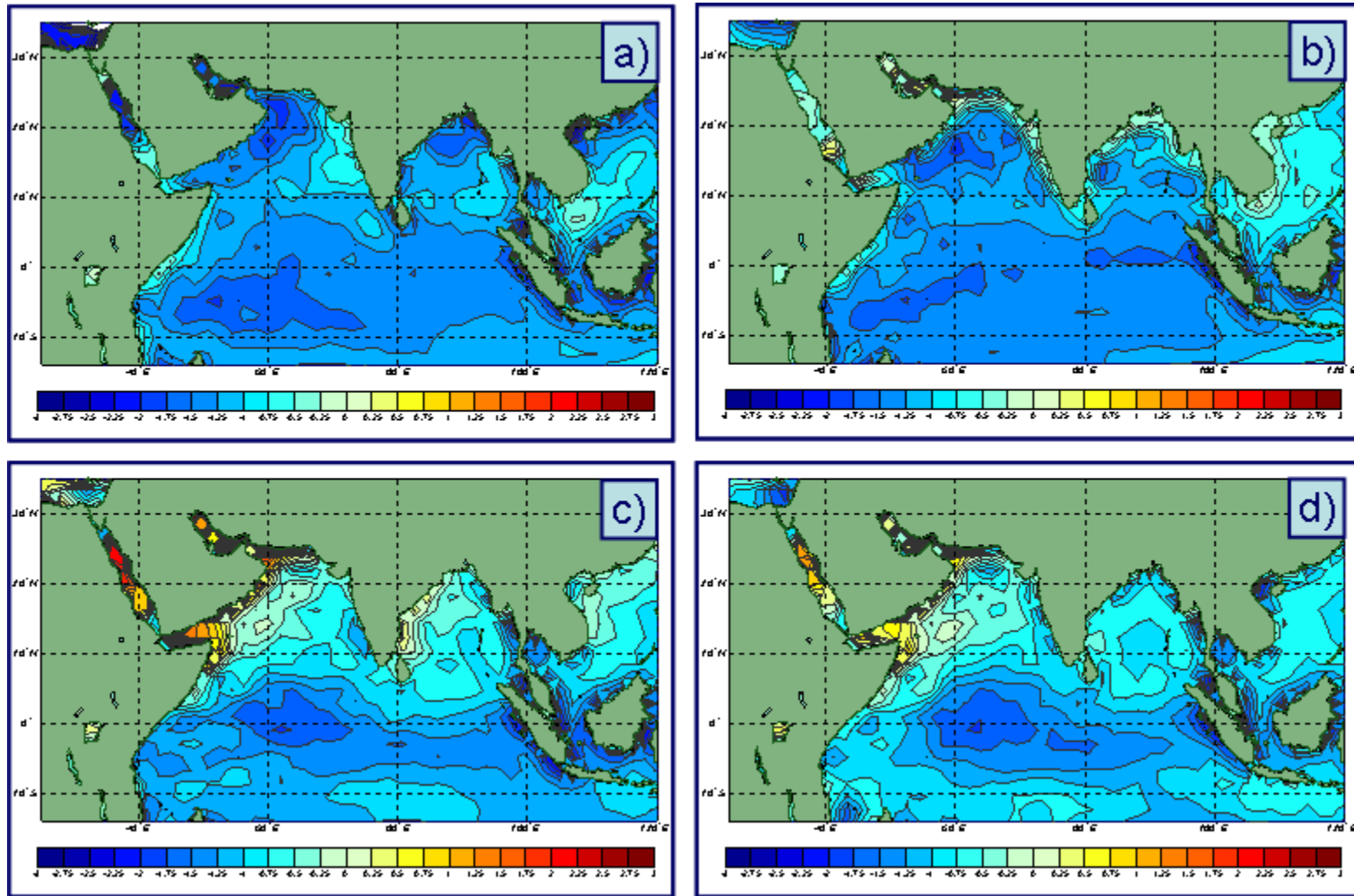


Figure 28. LTM ASTD ($^{\circ}\text{C}$) for: (a) NDJ; (b) FMA; (c) MJJ; and (d) ASO

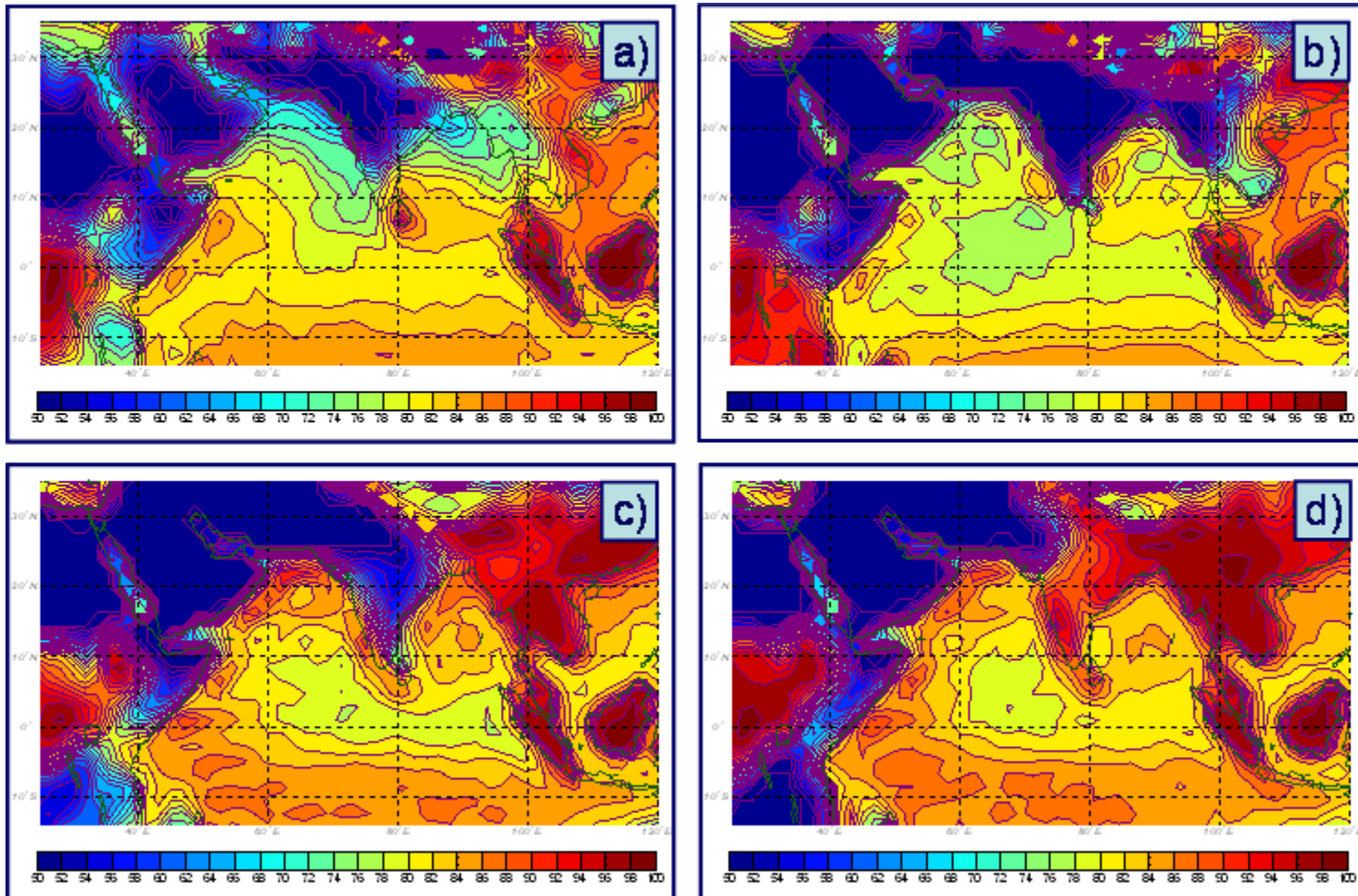


Figure 29. LTM RH (%) for: (a) NDJ; (b) FMA (c) MJJ; and (d) ASO

The effects of moisture advection are clearly seen in Figure 29a where, in the northeast monsoonal flow, drier air extends across the northeast Arabian Sea with increasing RH as its sea track increases. The RH LTM maxima, ~85%, is found along the Somali coast and in the SE trade wind region.

During the boreal summer, in the southwest monsoonal regime, moisture is advected from the equatorial zone northeast along the Somali coast and into the Arabian Sea. Higher RH regions are also observed along the west Indian coast with the onset of annual rains. RH in the Arabian Gulf remains low (~55-60%) for most of the year, but increases to ~70% during boreal winter months.

C. INFLUENCE OF FACTORS ON EDH IN SPECIFIC AREAS.

1. Equatorial Region

As an example of EDH variability and how it is affected by the factors that determine EDH, we studied the Diego Garcia region (see Figure 20). Monthly average EDH in this region varies from 8.6 to 10.2 m in a biannual cycle, as illustrated in Figure 30a. Monthly mean LTM values for wind, SST, Ta, ASTD and RH are also plotted in Figure 30(b-e).

EDH monthly LTM values do not vary that much over the course of a year because: (1) conditions are unstable throughout the year on average; (2) for the observed LTM ASTD range (-0.9 to -1.6 °C), the bulk ED model is relatively insensitive to changes in the input parameters (see Appendix A); (3) the factors that affect EDH do not vary much in this open ocean region; and (4) the factor variations that do occur tend to counteract each other. When wind speeds are higher, which tends to produce higher EDH, the RH is high and SST is low, both of which tend to produce lower EDHs. The reverse situation is also observed (e.g., when WS is low, RH is also low and SST is high).

The maxima in LTM EDH values (~10.2 m) occurs in July-August due to the maxima in wind speed (8 ms^{-1}), this WS maxima being just high enough to counteract the RH being high (86 %) and the LTM SST being at its lowest values (26 °C).

Monthly correlations of Diego Garcia EDH with the various factors are shown in Figure 30f. These correlations are used to help determine which of the factors is likely to be the most important in causing mean monthly EDH changes. It is important to note that a strong correlation between a factor and EDH does not by itself show that changes in the factor are the cause of changes in EDH. However, given that we know how bulk EDH estimates vary as one input factor changes, high correlations and factor value changes may indicate which factors are most important at different times and locations. The significance of the correlation values in Figures 30-34 are given in Table 2. Further information on the significance of correlations is discussed at <http://www.cdc.noaa.gov/Correlation/significance.html> (accessed August 2007).

Table 2. Significance of correlation values for a 37 year climatology. Information from <http://www.cdc.noaa.gov/Correlation/significance.html>, accessed August 2007.

Correlation Value	Significance Level
0.274	95%
0.324	97.5%
0.380	99%
0.470	99.5%

For Diego Garcia, WS is the most significantly correlated factor over the annual cycle with correlation values between 0.4 and 0.8 indicating a significance level of 99 % or more. Although WS itself has a biannual cycle, the minima and maxima of WS and EDH do not exactly align; indicating that other factors are also important.

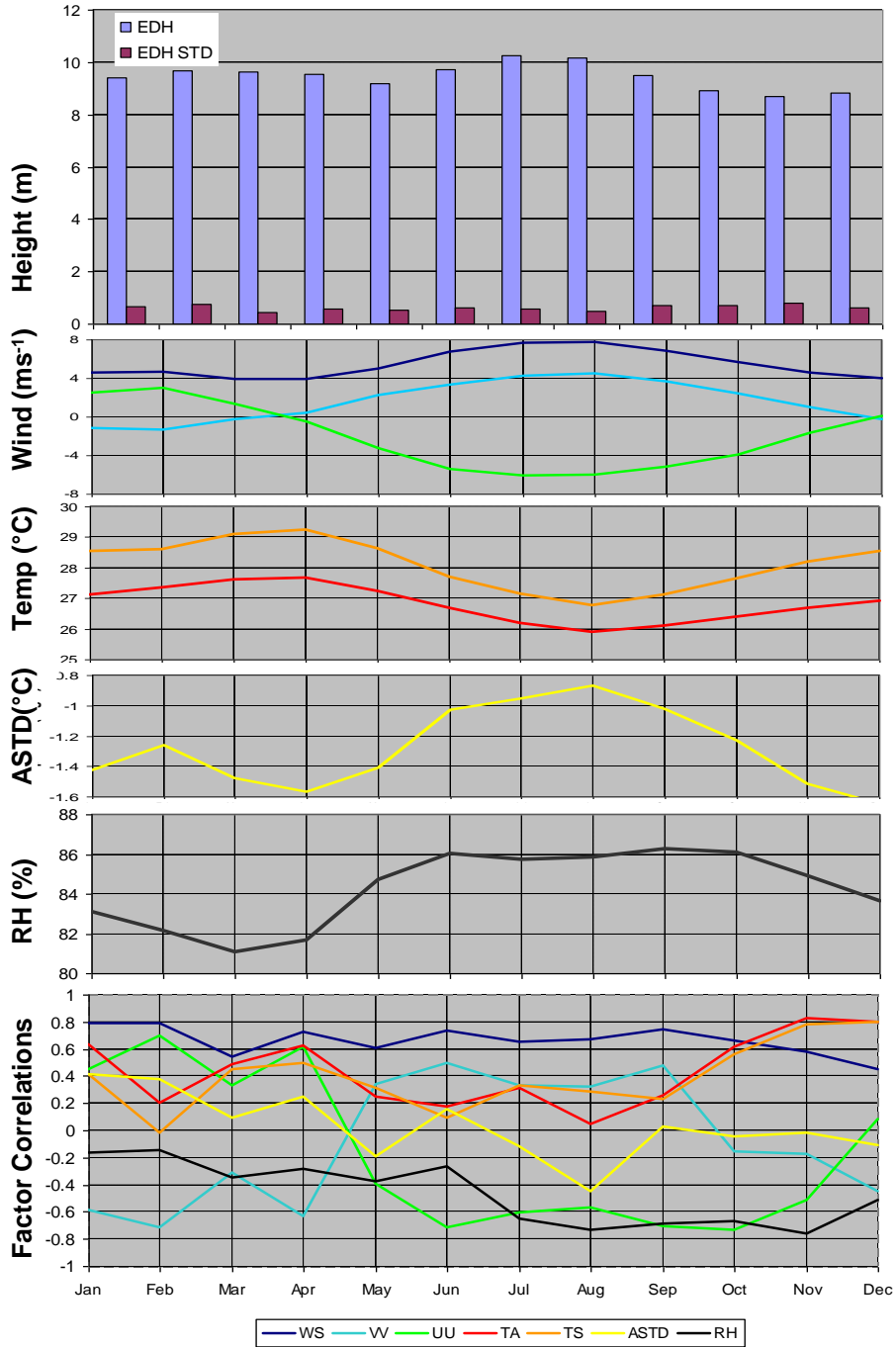


Figure 30. Seasonal cycle of monthly LTM EDH and EDH factor values (panels a-e) and correlations of EDH with EDH factors (panel f) for Diego Garcia region (see Figure 20). (a) EDH and EDH standard deviation; (b) wind speed, u and v components of wind; (c) SST and Ta; (d) ASTD; (e) RH; (f) zero lag correlation for each month of EDH (panel a) with each of the factors (panels b-e), with the color of the correlation curves indicating the factor for which the correlation was calculated (see color code).

RH is negatively correlated throughout the year. This is expected due to the relationship of EDH to RH seen in Appendix A. A negative correlation means that when RH is increasing, it has a reducing influence on EDH. Thus from March to June, when mean RH increases from ~81% to 86% and the correlation is ~-0.3 to -0.4, the RH has a reducing influence on EDH and indeed a slight height reduction is seen from March to May. However, by June, WS is increasing and is the dominant factor.

Between November and December, surface temperatures have a high positive correlation with a greater significance than the WS correlation. At this time, temperature increases and this is reflected in an increase in EDH. This occurs despite a decrease in WS, which is positively correlated and would thus have a height reduction influence. However, the RH factor values are decreasing and thus RH has an increasing influence on EDH between October and December.

Note that although ASTD values vary, they are not significantly correlated with EDH. This is primarily because these equatorial regions are unstable, so the small changes observed in monthly mean ASTD are not expected to cause a great change in EDH, which is borne out by the low significance values.

Thus the correlation plot indicates that for Diego Garcia, EDH changes are driven by a fine balance of WS and RH, and in the winter by Ta; all of which are strongly affected by monsoonal flows. The southeast trades are strongest in July and August, however, this occurs during the austral winter so temperatures are low. Increasing WS and decreasing temperatures have the opposite effect on EDH. For this area and season WS is the dominant factor, and the EDH seasonal cycle mimics the WS seasonal cycle.

For equatorial regions WS is the most significant factor for EDH change. WS varies considerably across the equatorial region as the monsoonal flow shifts from one regime to the other, causing EDH to vary accordingly. A vessel transiting across the equatorial region needs to be aware that as it crosses the

equatorial trough into or out of the southeasterly trades or northwest monsoon flow that EDH will vary driven primarily by changes in WS and also RH and Ta/SST to a lesser extent.

2. Arabian Sea

During the boreal winter, along leeward coasts in the Arabian Sea area, dry air is advected from the land over the ocean (Figure 29a), which would tend to lower RH and increase EDH. In the central Arabian Sea, there is a complex balance between lower RH (which would increase EDH), cooler SST (which would decrease in EDH), and varying wind strength (Figures 22, 23, 25, 26, 29, 31).

During the spring and summer, along the western ocean boundary, strong southwest monsoon winds cause mixing of the atmospheric and oceanic boundary layers, upwelling, and relatively cool SSTs (e.g., during July-September, along the Somali and SE Omani coasts). This leads to cooler and more humid surface conditions, and thus to lower EDH in many areas of the Arabian Sea (Figures 22, 23, 25, 26, 29, 31).

To investigate the effect of upwelling on EDH a correlation analysis was completed for the Omani and Somali coast regions (see Figure 20). These two regions have many similar features, therefore only the Omani correlations are presented in this section (Figure 31). The Somali coast correlations are shown in Appendix C.

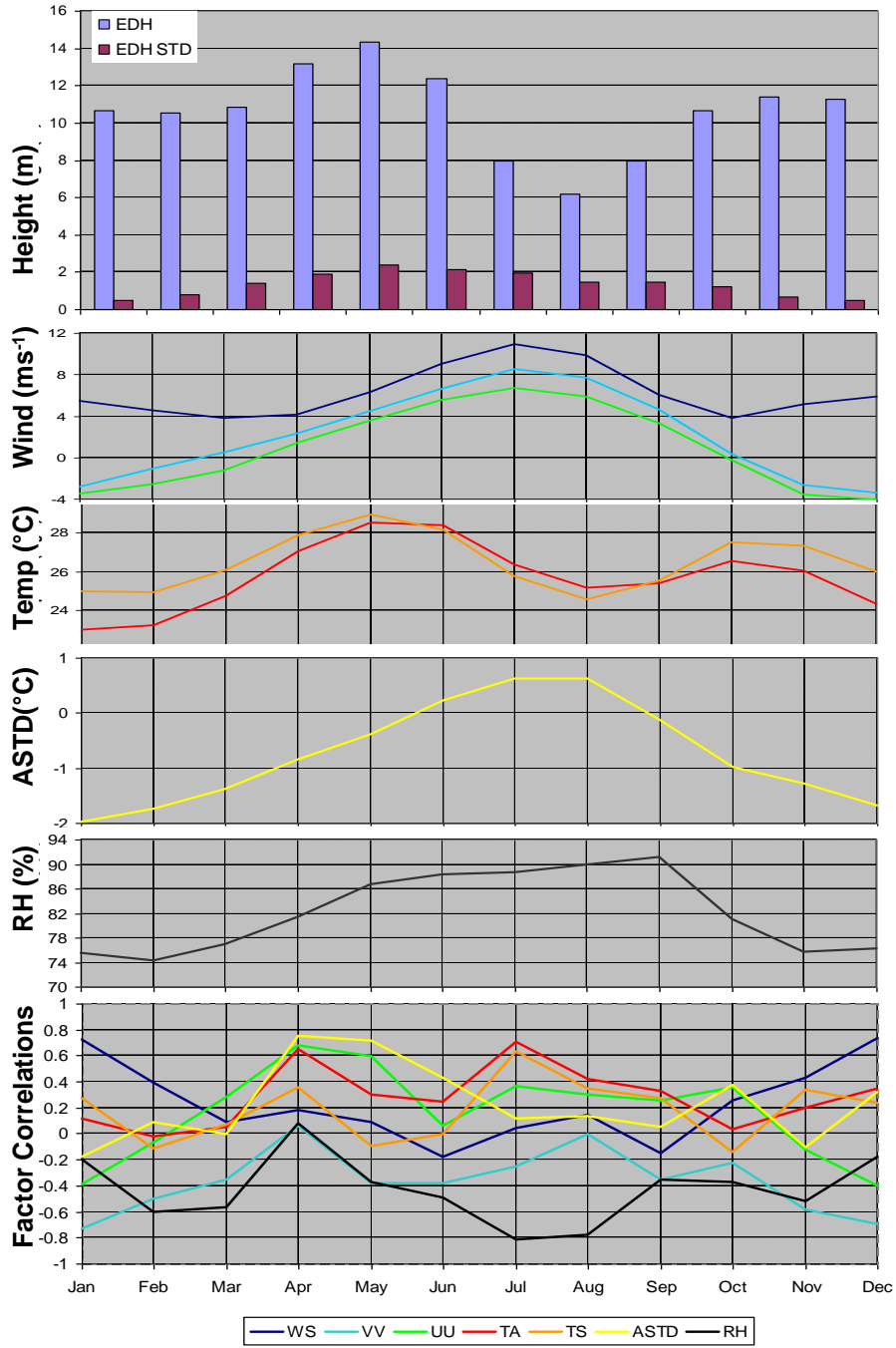


Figure 31. Seasonal cycle of monthly LTM EDH and EDH factor values (panels a-e) and correlations of EDH with EDH factors (panel f) for Omani coast region (see Figure 20). (a) EDH and EDH standard deviation; (b) wind speed, u and v components of wind; (c) SST and Ta; (d) ASTD; (e) RH; (f) zero lag correlation for each month of EDH (panel a) with each of the factors (panels b-e), with the color of the correlation curves indicating the factor for which the correlation was calculated (see color code).

a. Omani Coast Correlations

As expected, monthly LTM EDH values in the coastal Omani region vary more than in the open ocean Diego Garcia region, and range from a minimum of ~6.2 m in August to a maximum of ~14.5 m in April (Figure 31). This greater range in EDH is expected since: (1) ASTD varies from -2 to 0.6 °C, and thus includes both unstable and stable stratification; and (2) the factors that determine EDH have significantly higher variations than in the Diego Garcia region.

The minima in monthly LTM EDH values occurs during August (incidentally, the same time as when Diego Garcia has its EDH maxima), and coincides with the Somali Jet causing upwelling of cold water along the Omani Coast (Figures 22, 23, 25, 26, 31). The cold SSTs lead to stable conditions (ASTD ~0.6 °C, Figures 28, 31). At the same time, the southwesterly Somali Jet winds that parallel the coast of Africa bring moist air from near the equator and that air advects moisture to the Omani Coast region, with RH values in August-September reaching 90% (Figures 25, 29, 31). At these high humidity values, EDHs are actually lower in stable conditions than unstable (see Appendix A). Therefore, the combination of stable conditions and very high humidity leads to the monthly mean EDH minima occurring in August (Figure 31).

The EDH-factor correlations for the Omani coast region (Figure 31f) show that during December-January, WS has a strong positive correlation with EDH and a significance level over 99.5%. From January to February, the WS correlation falls but still has a significance level over 95%, and RH has an increasingly significant correlation with correlation values of -0.6 in February that are maintained into March. For the December to February period, EDH varies little, indicating that there is a balance between the reducing influence on EDH due to the decrease in WS, and the expected increase in EDH due to RH rising from February through the summer. During the spring transition season and in the early southwest monsoon (April-May), ASTD is the most positively correlated

factor; even though it remains negative, indicating unstable conditions. The next most significant positive correlation factors are T_a and the u component of wind. Both factors are increasing due to summer heating and the southwest monsoon, and thus lead to an increase in EDH.

In June, EDH begins to decrease, reaching a minimum in August. As discussed earlier, this is primarily due to upwelling of cold water along the coast, which causes SST to reduce and subsequently T_a . From June to September, RH increases less rapidly than in previous months and has the highest absolute correlation values, -0.5 to -0.8. This negative correlation indicates that as RH increases, EDH decreases. This decrease in height is also positively correlated to the decreasing T_a . It is worth noting that the ASTD becomes positive over this time period but is not significantly correlated to the changing EDH.

In September-October, upwelling diminishes or ceases, and both RH and WS decrease. In September, the negative correlation to RH has a value of ~ -0.4 and T_a has a positive correlation as it increases and leads to higher EDH values.

This western boundary example of EDH-factor correlations, and the analogous Somali coast correlations (Appendix C), show that EDH does not increase when ASTD becomes positive due to the upwelling of cold water. In fact, EDH has its lowest annual mean values during the boreal summer upwelling period, due primarily to the very high humidity and relatively high wind speed conditions associated with the southwest monsoon flow that causes the upwelling. That is, the southwesterly flows that produce the upwelling and stable conditions (positive ASTD) also produce high WS and RH values that have a dominant influence on EDH and lead to the lowest EDH values of the year. This indicates that EDH values in the Somali Jet region are sensitive to the strength and moisture content of the monsoonal flows. Variations in the monsoon flow

can cause significant changes in EDH. Therefore, the Somali Jet and its variations should be closely monitored when analyzing and forecasting EDH in the Somali and Omani coastal regions.

3. Gulf of Oman

In the Gulf of Oman (GOO) region (Figure 20), monthly LTM EDH values are highly dependent upon the wind direction and the advection of warm or cold air from adjacent land and sea areas, depending upon the season (Figures 22, 23, 25, 27, 32). EDH varies on an annual cycle from 11 m in December-January to 65 m in May.

From November to February, the wind direction in the GOO has a northerly component that advects subsiding cool, dry air from the Asian High into the GOO (Figure 25, 32). The cool air advected into the GOO causes conditions to be unstable, which leads to lower EDH, despite the low RH values (Figure 32) which would normally be associated with increasing EDH (Appendix A, Figure 59).

The May values of the different factors are nearly identical to those in October, leading to very similar EDH values in these two transition months. As winds shift to a southerly direction and there is more insolation during March-May, the air temperature increases more rapidly than the SST, leading to stable conditions and higher EDHs in the GOO (Figure 32). Peak LTM values of EDH occur in April-May, when ASTD is at or near its maximum positive values ($\sim +1.5$ °C) and RH is still low ($\sim 70-72$ %). The increase in SST from March to June also helps produce higher EDHs.

The correlations of EDH with its factors (Figure 32f) confirm that: (1) EDH is strongly correlated to ASTD throughout the year, remaining above 0.8 from February to October; and (2) from December to April, T_a is the next most

significant factor with correlation values between 0.4 and 0.8. T_a dips down to ~ 22 °C in January and increases to 28 °C by April, and these changes in T_a are reflected in the corresponding fall and rise of EDH.

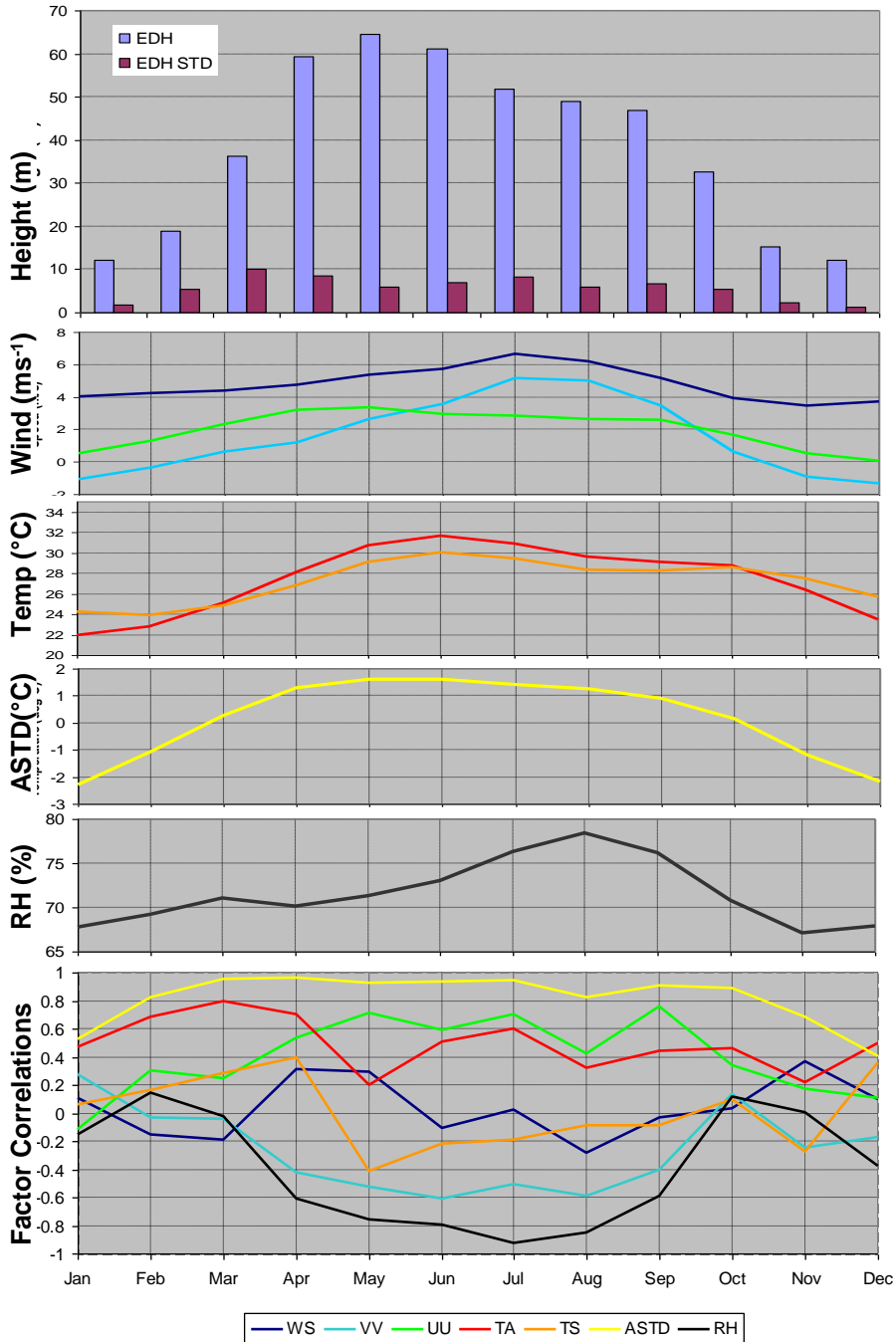


Figure 32. Seasonal cycle of monthly LTM EDH and EDH factor values (panels a-e) and correlations of EDH with EDH factors (panel f) for the Gulf of Oman (see Figure 20). (a) EDH and EDH standard deviation; (b) wind speed, u and v components of wind; (c) SST and Ta; (d) ASTD; (e) RH; (f) zero lag correlation for each month of EDH (panel a) with each of the factors (panels b-e), with the color of the correlation curves indicating the factor for which the correlation was calculated (see color code).

From April to September, RH and the v component of wind are negatively correlated to EDH, both exceeding 99.5% significance level (Figure 32). As the southwest monsoon flow intensifies, the wind direction becomes more southerly, thereby leading to the advection of more moisture into the region, with RH reaching a maximum in August (Figures 25, 29, 32). As the RH increases, EDH decreases due to the combined effects of ASTD and RH. However, by September the RH is falling, which slows the rate at which EDH declines. The correlation of RH with EDH (Figure 32f) indicates that: (1) RH is a significant factor for much of the year; (2) when the magnitude of the RH correlation changes from insignificant to significant levels from March to May, there is a pronounced increase in EDH; and (3) when the magnitude of the RH correlation changes from significant to insignificant levels from September to November, there is a pronounced decrease in EDH.

4. South Arabian Gulf

Only the South Arabian Gulf (SAG) is discussed in this section, as this is the only region in the Arabian Gulf where there is a whole data grid box that does not include land (see Figures 20, 21). Monthly LTM EDH values in the SAG are highly dependent upon the wind direction and the advection of cold air in the winter and warm, dry air in the summer from adjacent land masses (Figures 22, 23, 25, 27, 29, 33). EDH varies from 10-15 m during the winter months to above 60 m during the summer, with a maximum in May. Wind speed is quite constant during the year, and thus has little effect on month to month EDH variations, as indicated by its low correlation values (Figure 33f).

Minimum EDH values occur from October to February, when cool air is advected from nearby land areas, leading to unstable conditions and lower EDH values. Humidity also tends to be higher during these months as the predominant wind direction is northwesterly providing a sea track over the SAG

(Figures 25, 26, 29, 33). SST is also lower due to wind mixing of the SAG and lower ambient air temperatures (Figures 26, 33c). Both of these factors tend to produce lower EDHs.

During the spring and through the summer warm, dry air is advected over the SAG and, although the SST increases during this time due to insolation, the air temperature increases faster, resulting in stable conditions from March to September (Figures 25-29, 33). These stable conditions, when combined with lower humidity, lead to very high EDH values, in excess of 60 m (Figures 22, 23, 33a). The peak EDH (>80 m) values occur in May-July, when ASTD also has its peak values (~3 °C) and RH has its minima (~60 %). Very high bulk EDH estimates are expected for these strongly stable and low humidity conditions. However, it should be noted that highly stable conditions also lead to greater uncertainty in the applicability of MOS theory, upon which the bulk ED model is based, see Chapter I section B. It is especially uncertain whether the surface layer actually extends to heights greater than 50 m in such highly stable conditions, therefore the exact values of the resulting large EDH values must be viewed with caution.

The correlation plot also indicates that ASTD is the most significant factor in the SAG, being positively correlated with a correlation value of ~0.8 from February to October, and accounting for a large part for the overall height changes in EDH throughout the year.

From February to June, EDH and RH are negatively correlated, with a correlation value of -0.3 to -0.4, and Ta is positively correlated with values above 0.4. This indicates that the advection of warm, dry air causes EDH to increase. Over the winter (November-January), Ta and the u component of wind are also significantly correlated factors. These correlations indicate that to predict EDH values in the SAG, it is particularly important to predict climate and weather patterns that would alter Ta and wind direction during the winter, and that would alter RH during the spring. Note to that when ASTD reaches near stable

conditions, small changes in T_a or SST can lead to large changes in EDH (see Appendix A). For example, when ASTD is close to zero, diurnal heating processes can lead to large diurnal variations in stability, and thus in EDH.

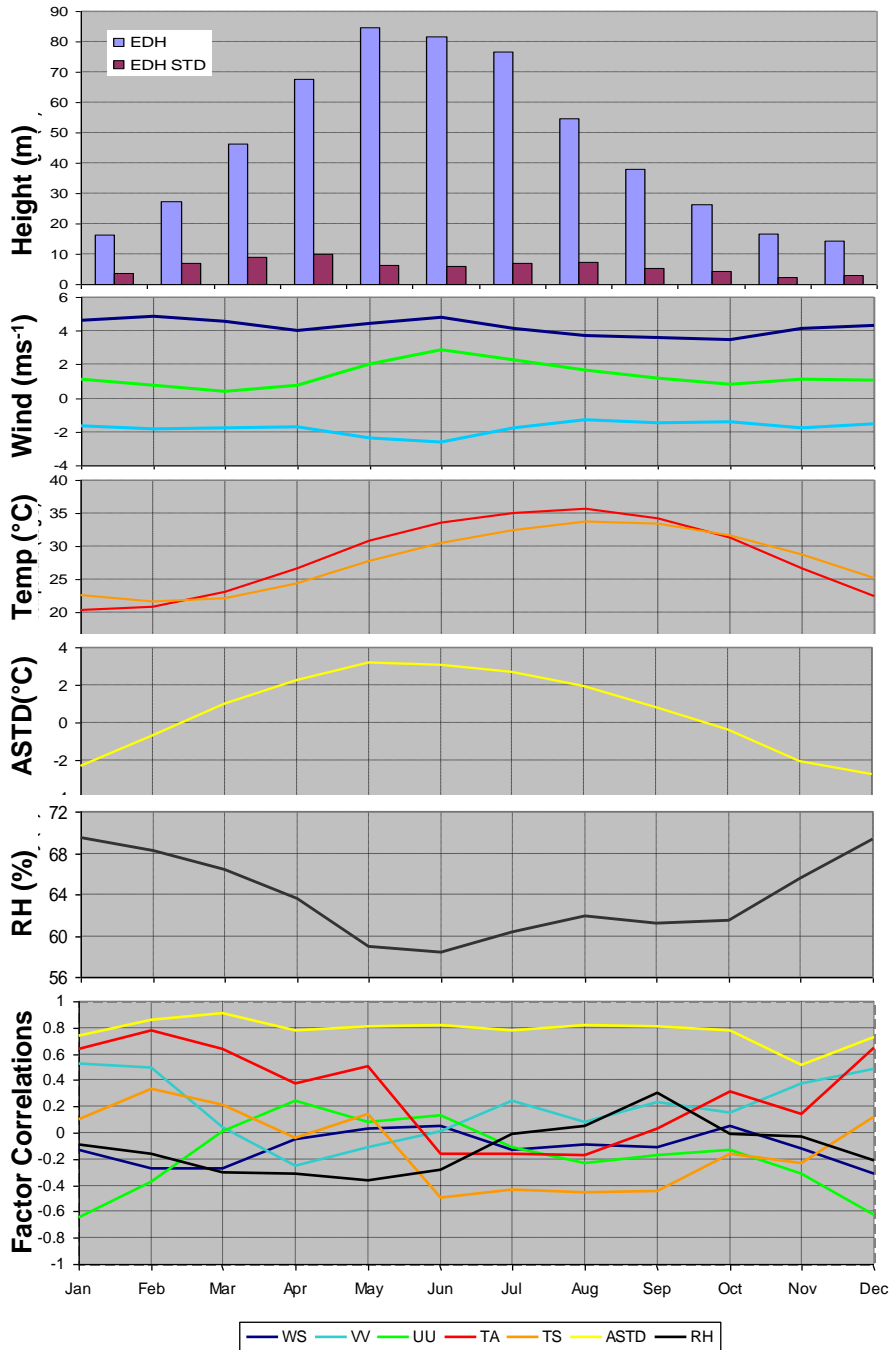


Figure 33. Seasonal cycle of monthly LTM EDH and EDH factor values (panels a-e) and correlations of EDH with EDH factors (panel f) for the Southern Arabian Gulf (see Figure 20). (a) EDH and EDH standard deviation; (b) wind speed, u and v components of wind; (c) SST and Ta; (d) ASTD; (e) RH; (f) zero lag correlation for each month of EDH (panel a) with each of the factors (panels b-e), with the color of the correlation curves indicating the factor for which the correlation was calculated (see color code).

5. Gulf of Aden

EDH in the Gulf of Aden (GOA, Figure 20) is, like the GOO and SAG, highly dependant on wind direction and the advection of warm, dry air from the adjacent land areas (Figures 22, 23, 25, 27, 29, 34).

During the winter, northeasterly winds flow into the GOA, leading to lower T_a , negative ASTD, and higher RH (Figures 25-29, 34). In March, the surrounding land begins to warm, and the ASTD becomes positive, initially in the western GOA and then throughout. Thus, EDH begins to increase, with higher EDHs occurring to the west.

During the summer period of southwesterly monsoonal flow, high T_a , low RH air is advected over the GOA, resulting in stable ASTD conditions and very high EDH (Figures, 22, 23, 25-29, 34). By July, the mean wind direction has veered from south-southwest to southwest and warm, low RH air is advected out of the GOA, such that an area with EDHs of 40-50 m extends out of the Gulf, encompassing the Horn of Africa and southern Omani coast (Figures 22, 23, 25, 29, 34). During the autumn transition season the wind strength slackens and EDHs reduce, returning to winter heights

The seasonal cycle of EDH in the GOA is similar to that in the SAG (Figures 33-34), although the maximum EDH values (~75 m) are reached in June-August, about one to two months later than in the SAG. The caution discussed in the SAG section regarding the high EDH values that occur in very unstable and low to moderate RH conditions also applies here.

Again, ASTD is the most significant factor in the GOA, with correlation values from 0.8 to 1 occurring from February to November, and dropping to 0.5 in December-January. The value of ASTD is positive from April to September, with EDH reaching a maximum in the middle of this period (June-July-August). Although WS peaks in June to August, it is not strongly correlated with EDH. This appears to be because the peak wind speeds are associated with the advection of warm, low RH air into and over the GOA, leading to high T_a , high

positive ASTD, and low RH, all of which act to: (1) raise EDH; and (2) counteract the effects of the relatively high wind speeds which would tend to reduce EDH (Figures 22, 23, 25-29, 34).

In September-November, the wind direction is significantly positively correlated with EDH, with both the u and v components of wind reaching correlation values of ~ 0.6 . This indicates the wind direction is an important factor, even though it is not an explicit factor in the ED model's calculation of EDH. Thus, it is likely that the wind direction is a proxy for one or more of the factors used in the model. During September-November, the EDH-wind direction switches from southwesterly to northeasterly, T_a declines sharply, ASTD switches from positive (stable) to negative (unstable), RH rises, and EDH falls rapidly. All of these changes are consistent with the onset of the northeasterly monsoon regime in which cold, high RH air flows across the NW IO and nearby seas (Figures 22-23, 25-29, 34). These results indicate the importance in analyzing and forecasting EDH in the GOA during fall and of carefully accounting for climate and weather changes cause changes in wind direction. These changes include early and late starts to the northeasterly monsoon regime, climate variations that alter this regime, and synoptic events that strengthen or weaken this regime.

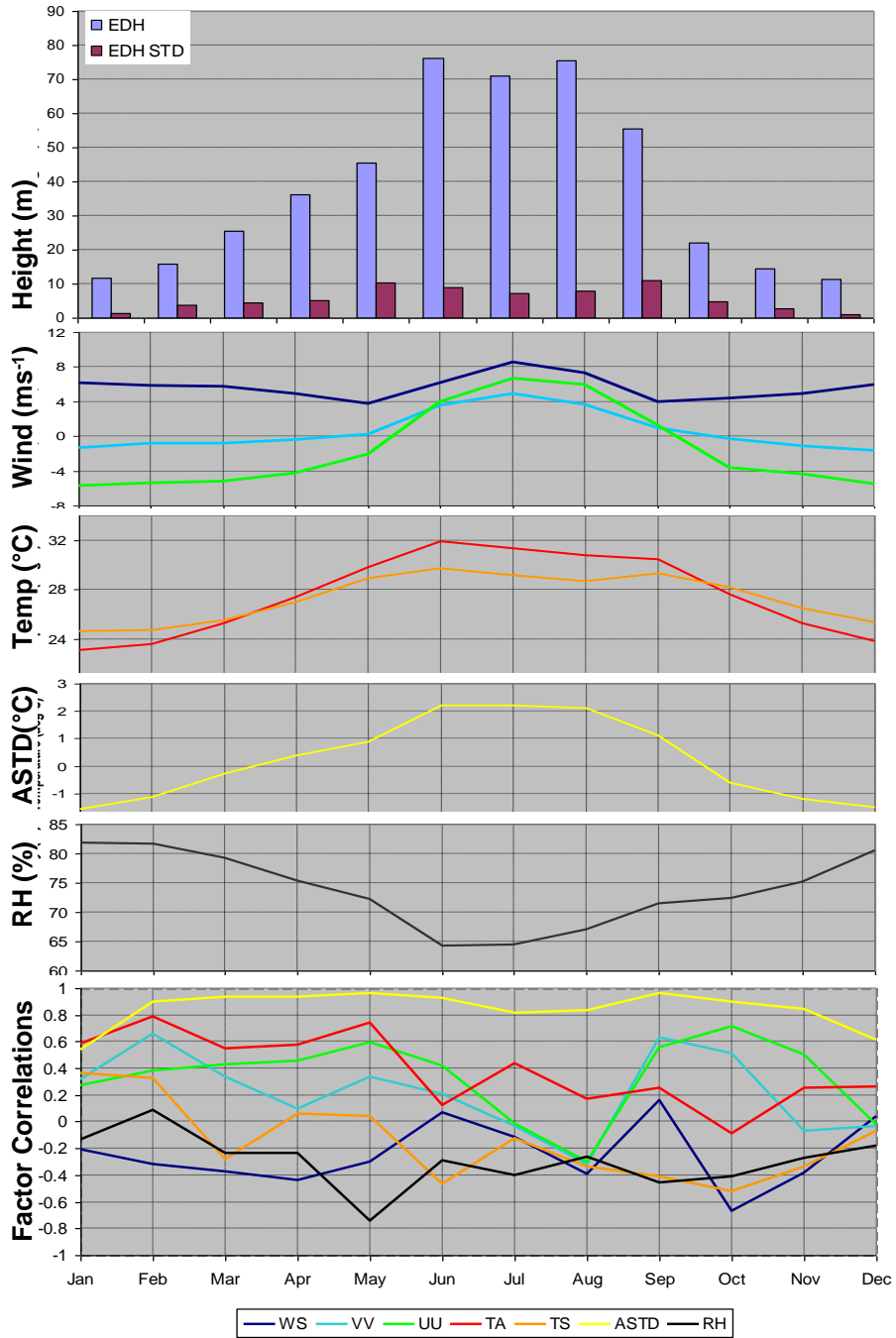


Figure 34. Seasonal cycle of monthly LTM EDH and EDH factor values (panels a-e) and correlations of EDH with EDH factors (panel f) for the Gulf of Aden (see Figure 20). (a) EDH and EDH standard deviation; (b) wind speed, u and v components of wind; (c) SST and Ta; (d) ASTD; (e) RH; (f) zero lag correlation for each month of EDH (panel a) with each of the factors (panels b-e), with the color of the correlation curves indicating the factor for which the correlation was calculated (see color code).

D. AREPS CLIMATOLOGY AND BUOY COMPARISON

1. Comparison to Present U.S. Navy EDH Climatology

Figures 35 and 36 compare monthly mean EDH values from: (1) the present U.S. Navy EDH climatology, referred to as the existing climatology, based on observations from 1970-1984 and the PJ model (see Chapter I, section F); (2) smart EDH climatology based on reanalysis data for 1970-2006; and (3) EDH climatology based on reanalysis data for 1970-1984. The regions represented by all three climatologies are the Marsden square 066 in the Arabian Sea (Figures 20, 35) and Marsden square 030 in the tropical NW IO (Figures 20, 36).

The comparisons show that all three climatologies have similar seasonal cycles but that the existing climatology has EDH values that are ~5-8 m (~30-50%) higher in all months. This difference is due primarily to the use of the PJ ED model in computing the existing climatology, which in most unstable and near-neutral conditions produces higher EDH values than the NPS ED model, which was used to compute the reanalysis-based climatologies. The fact that the two climatologies were derived from different data sets covering different years will also contribute to discrepancies between the existing and reanalysis-based climatologies. The small differences between the smart EDH climatology based on 1970-2006 reanalysis data and the similar climatology based on 1970-1984 reanalysis data indicates that, for the reanalysis data set, 1970-1984 was similar to 1970-2006, and thus representative of longer term mean conditions. This result hints that the substantial differences between the existing climatology and the reanalysis-based climatologies *may* be strongly related to differences between the PJ and NPS EH models.

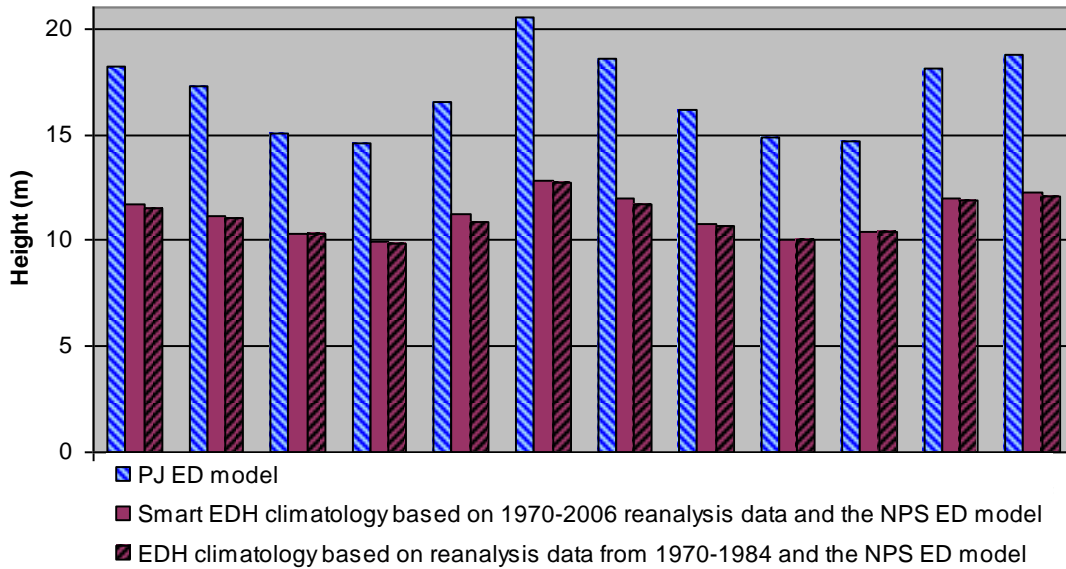


Figure 35. Comparison of monthly EDH from existing Navy climatology based on observations from 1970-1984 and the PJ ED model (blue), smart EDH climatology based on 1970-2006 reanalysis data and the NPS ED model (purple), and EDH climatology based on reanalysis data from 1970-1984 and the NPS ED model (dashed purple) for Marsden square 066 in the Arabian Sea (see Figure 20)

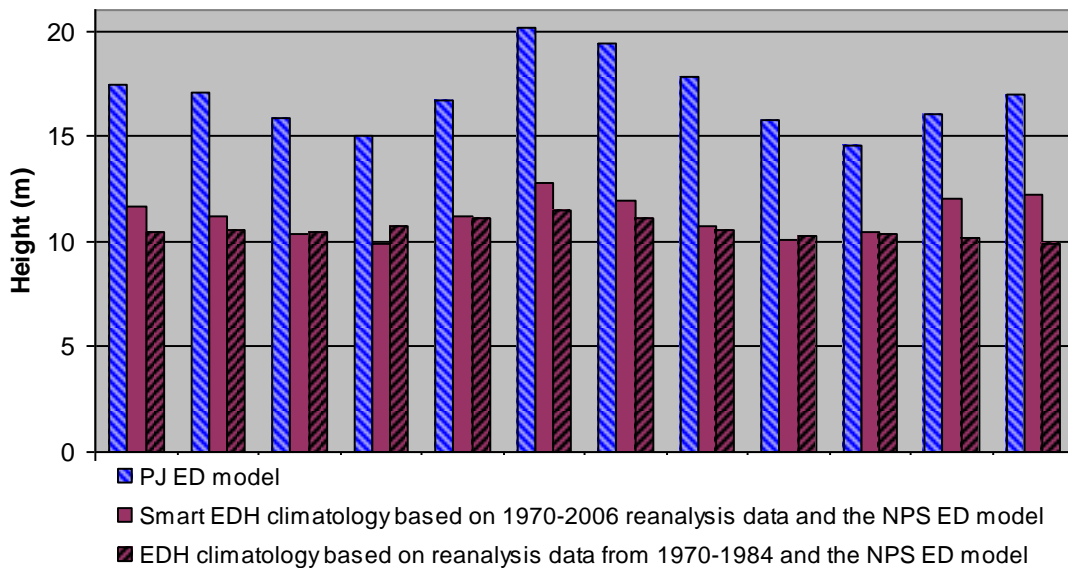


Figure 36. Comparison of monthly EDH from existing Navy climatology based on observations from 1970-1984 and the PJ ED model (blue), smart EDH climatology based on 1970-2006 reanalysis data and the NPS ED model (purple), and EDH climatology based on reanalysis data from 1970-1984 and the NPS ED model (dashed purple) for Marsden square 030 in the tropical NW IO (see Figure 20).

The spatial resolution of our smart EDH climatology based on reanalysis data (~210 km x~210 km) is considerable higher than that of the existing Navy EDH climatology (~1000 km x ~1000 km), with about 25 times more grid points in a 10° x 10° box than the existing climatology. The existing climatology, as it is incorporated within AREPS, is only displayed in monthly bar graph form. However, to allow spatial and temporal comparisons of the existing and smart EDH climatologies, we created map displays of both climatologies. Figure 37 shows an example for September LTM EDH from the two climatologies. There are some basic similarities, but clearly large differences in both magnitude and spatial patterns. The EDH values in the gulfs are very dissimilar between the two climatologies, due to the 'open ocean adjustment' of the PJ model which does not allow stable conditions with their resulting higher EDH values to occur (see Chapter I, section F). Displays such as Figure 37 highlight the benefits of higher resolution data and enable a much improved understanding of EDH spatial variability. The marked difference in EDH magnitudes and spatial patterns in the two climatologies (Figures 35-37), combined with the differences in the data sets and ED models used to generate the two climatologies (see Chapter I, sections B.3 and F; Chapter II, sections A and C), indicate that the smart EDH climatology is considerably more accurate than the existing Navy climatology. However, ground-truthing of the reanalysis fields used to develop the smart EDH climatology, and of the EDH values produced by the NPS ED model, is needed to assess the absolute accuracy of the smart EDH climatology.

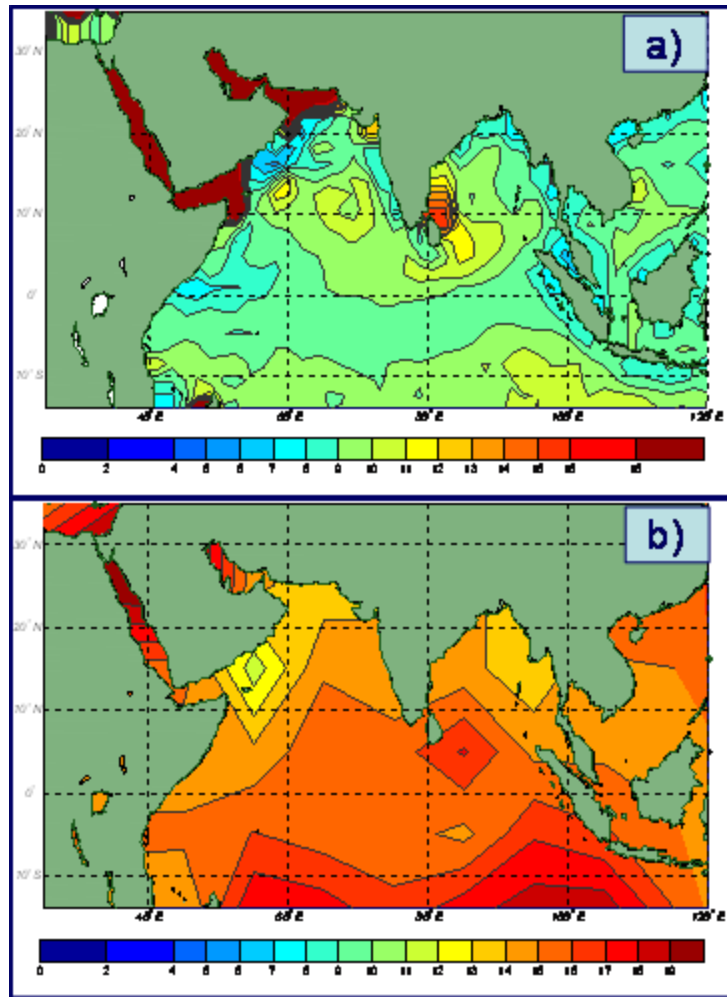


Figure 37. LTM EDH (m) values for September from (a) smart EDH climatology based on reanalysis data for 1970-2006 and the NPS ED model; and (b) existing Navy climatology based on observations from 1970-1984 and the PJ ED model.

2. Comparison to Woods Hole Oceanographic Institute (WHOI) Buoy Data

One method for ground-truthing climatologies is to compare them to independent observations. However, such comparisons can be problematic, since it is very difficult to find buoys, or sets of buoys that are suitably instrumented, provide long term observations, and have a spatial coverage comparable to that from an individual climatology grid point. To conduct such a comparison, we used data from a Woods Hole Oceanographic Institute (WHOI)

buoy located at 15.5°N, 061.5°E (Figure 38). This buoy provided measurements of near-surface atmospheric conditions and SST from October 1994 to October 1995, (Weller et al., 2002). We used this data to calculate EDH from hourly buoy data using the NPS bulk ED model (Frederickson, personal communication) and compared this buoy EDH to the existing Navy EDH climatology from the Marsden square that includes the buoy location and the reanalysis grid point closest to the buoy location (Figure 38).

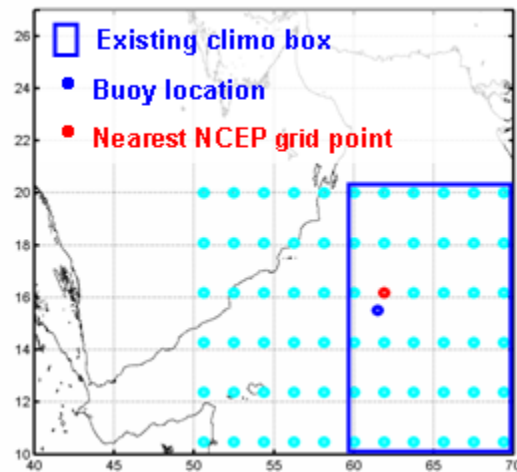


Figure 38. Location of WHOI buoy (dark blue dot), nearest NCEP reanalysis grid points (light blue dots), and closest Marsden square. (Marsden square 066, dark blue box).

Figure 39 compares monthly mean EDH values based on the WHOI buoy data with those from the closest Marsden square for the existing climatology and from the closest grid point for our smart climatology.

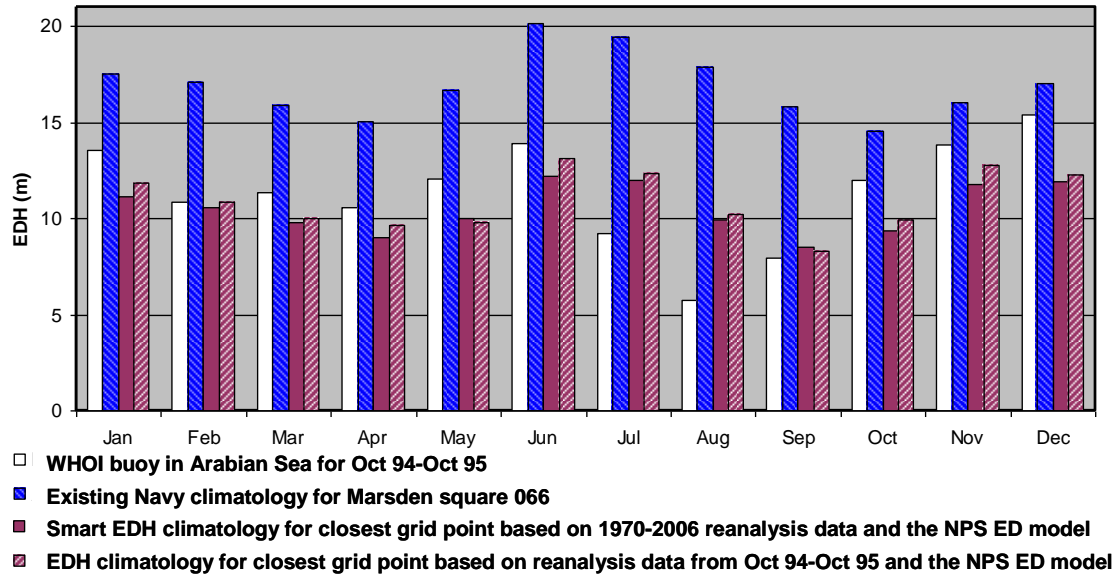


Figure 39. Comparison of monthly EDH from: WHOI buoy in Arabian Sea for October 1994–October 1995 (white); existing Navy climatology from Marsden square 066 and based on observations from 1970-1984 and the PJ ED model (blue), smart EDH climatology from closest reanalysis grid point and based on 1970-2006 reanalysis data and the NPS ED model (purple), and EDH climatology from closest reanalysis grid point based on reanalysis data from 1994-1995 and the NPS ED model (dashed purple). See Figure 38 for locations.

This plot shows that all datasets exhibit a similar annual cycle of EDH. The buoy values give monthly EDH means that vary more than either of the other three climatologies presented. In addition, the timing of the seasonal cycle varies, with the buoy EDH reaching a minimum of 6 m in August, whilst our smart climatology minimum is reached in September, and the existing climatology minimum is reached in October. The existing EDH climatology is consistently greater (~4-12 m) than the buoy mean values. Our smart EDH climatology is generally a couple of meters below the buoy means, except in July and August-September when it is greater. The EDH means calculated for 1994/95 gives values that are slightly more similar to the buoy than the smart climatology EDHs, except for March and July-August.

It should be stated that the EDH values based on the buoy, existing climatology, smart climatology, and 1994-1995 reanalysis monthly means should

not necessarily be the same, as they do not represent the same areas and/or time periods. Thus, no single set of EDH values represents an absolute truth or standard against which the others should be evaluated. However, we would expect the EDH values to be at least roughly similar; and they are, although the greater EDH values from the existing climatology are somewhat problematic. The buoy represents one point in space for one year, and was located where the Somali Jet position, structure, and strength would have a distinct effect on observations. Thus, it is unlikely to be representative of the mean across a large area, such as the NCEP grid box. This is supported by the poorest agreement between the buoy and the smart climatology EDH values occurring during July-August when the Somali Jet is strongest.

However, the generally good agreements between the buoy EDH and smart climatology EDH, and between the 1994-1995 reanalysis based EDH and the smart climatology EDH, indicate that the smart climatology EDH values are very plausible. In addition, two results suggest that our smart EDH climatology is more accurate than the existing Navy EDH climatology: (1) the generally better agreement between the buoy and the smart climatology than between the buoy and the existing climatology; and (2) the results from the comparisons of the smart climatology with the existing climatology shown in Chapter III, section D1.

E. CLIMATE VARIATIONS OF THE FACTORS WHICH AFFECT EDH

The EDH-factor correlation results (Chapter III, section C) indicate that the surface factors have significant correlations with EDH that vary with time and location. Thus, it is highly probable that climate variations, which affect many atmospheric and oceanic factors, could also have significant correlations with EDH in some regions and during some seasons. Figure 40 shows a map of the correlation of EDH for the Diego Garcia region with SST in the IO, with the corresponding significance levels shown in Table 2. Note that the EDH at Diego Garcia has significant positive correlations with SST near Diego Garcia and throughout much of the IO, but a significant negative correlation with SST

southeast of the Maritime Continent. This correlation, or teleconnection, pattern strongly indicates that EDH in the Diego Garcia region, and the equatorial IO in general, are affected by the IOZM (see Chapter I, section E, and Figures 13 and 15). Figure 41 shows the same results as Figure 40, but expanded to include the western and central Pacific. The negative (positive) correlations between Diego Garcia EDH and SST in the western (central) tropical Pacific indicate that EDH in the Diego Garcia region, and the equatorial IO in general, is strongly affected by ENLN events (see Chapter I, section E). The correlations shown in Figures 40-41 indicate, for example, that if SSTAs are negative southwest of the MC, or positive in the central tropical pacific, then EDH is likely to be anomalously high in the equatorial IO.

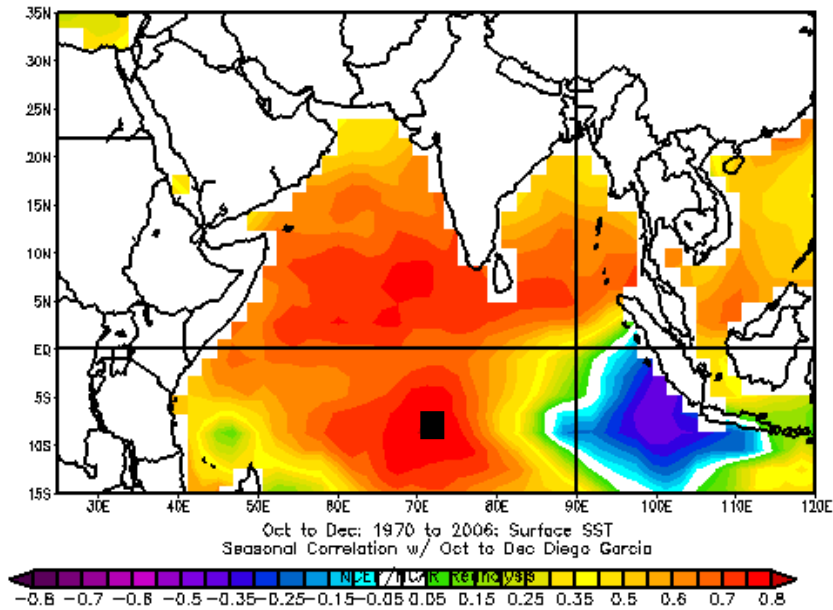


Figure 40. Correlation of our smart climatology EDH for the Diego Garcia region with SST across the IO. Black square marks the location of Diego Garcia. Image produced using NCEP reanalysis data and the NOAA/ESRL Physical Sciences Division web site at <http://www.cdc.noaa.gov/> using NCEP reanalysis data, (Kalnay et al., 1996) (accessed September 2007).

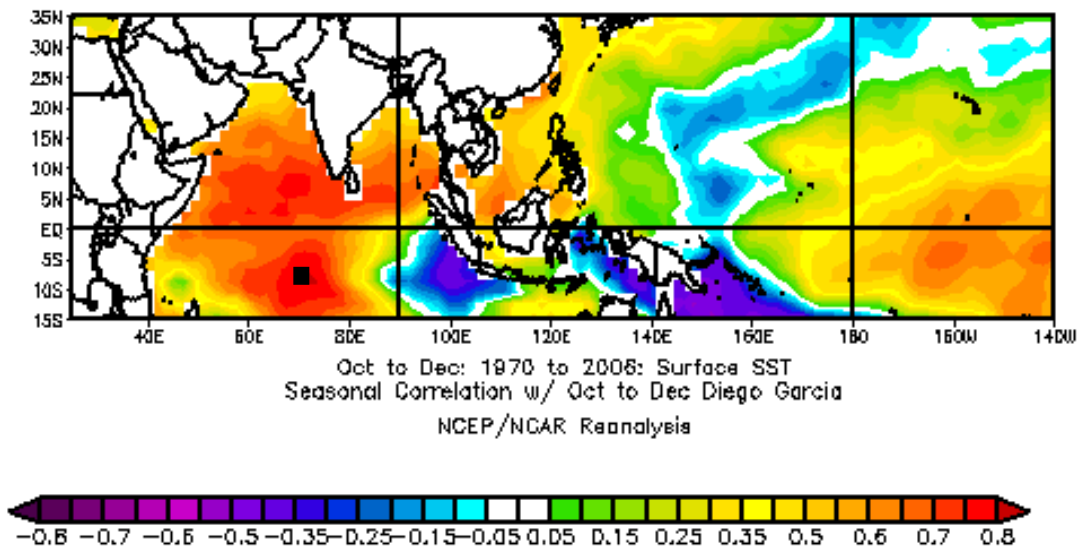


Figure 41. Correlation of our smart climatology EDH for the Diego Garcia region with SST across the IO and western-central Pacific. Image produced using NCEP reanalysis data and the NOAA/ESRL Physical Sciences Division web site at <http://www.cdc.noaa.gov/>, using NCEP reanalysis data, (Kalnay et al., 1996) accessed September 2007.

Figure 42 shows a correlation or teleconnection map for the correlation between EDH in the Diego Garcia region with 850 hPa geopotential heights in the IO region. The correlations reveal a pattern of positive correlations over India and the Bay of Bengal and the Diego Garcia region. This pattern is very similar to the Rossby-Kelvin wave response pattern that characterizes the low level height response to changes in MC convection during ENLN, IOZM and the Madden-Julian Oscillation (MJO; Madden and Julian 1994; LaJoie 2006; Vorhees 2006; Stepanek 2006). Together, Figures 40-42 indicate that EDH in the IO is affected by global scale climate variations that occur in and near the IO, including ENLN, IOZM, and MJO events.

Figures 43 and 44 show the correlations, or teleconnections, between EDH in the Somali coast region with zonal wind and outgoing longwave radiation (OLR), respectively.

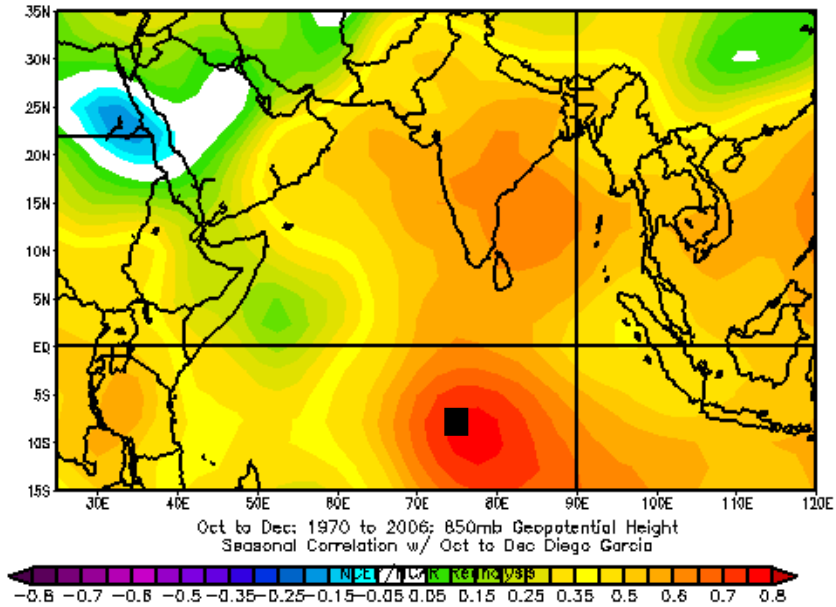


Figure 42. Correlation of our smart climatology EDH for the Diego Garcia region with 850 hPa geopotential height across the IO. Image produced using NCEP reanalysis data and the NOAA/ESRL Physical Sciences Division web site at <http://www.cdc.noaa.gov/>, using NCEP reanalysis data, (Kalnay et al., 1996) accessed September 2007.

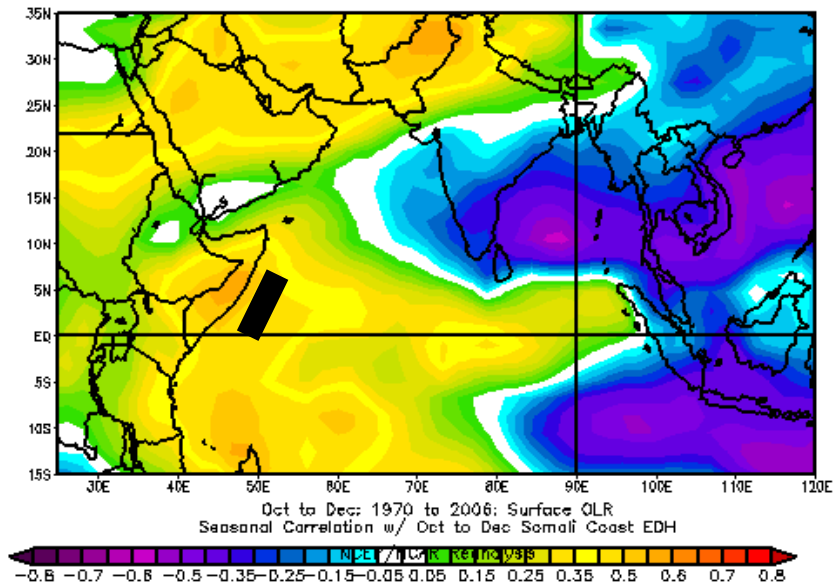


Figure 43. Correlation of our smart climatology EDH for the Somali coast region with OLR across the IO. Image produced using NCEP reanalysis data and the NOAA/ESRL Physical Sciences Division web site at <http://www.cdc.noaa.gov/>, using data referenced at (Liebmann et al., 1996), accessed September 2007.

Figure 43 indicates that EDH along the Somali coast is positively correlated with OLR in the western and equatorial IO, and negatively correlated with OLR to the northwest and southwest of the Maritime Continent (MC). This means, for example, that when OLR increases (decreases in the Bay of Bengal (corresponding to clear (cloudy) skies, then EDH in the Somali coast region tends to go down (up). Figure 44 shows that EDH along the Somali coast and is positively correlated with zonal surface wind speed across most of the NW IO and negatively correlated with zonal wind speed near the Tanzanian coast. The correlations in Figures 43-44 provide insights into the climate dynamics that affect EDH in the Somali coast region. For example, the negative correlations with OLR to the northwest and southwest of the MC are consistent with the Rossby-Kelvin wave response to changes in deep convection over the MC. This suggests that climate variations that affect this convection (e.g., ENLN, IOZM, MJO) also impact EDH in the Somali coast region. The positive (negative) correlation with zonal wind in the NW IO (near Tanzania) indicate the dependence of EDH in the Somali coast region to changes in the monsoonal winds that flow along the coast of east Africa (Figure 25).

These examples indicate that EDH changes in relatively localized regions of the IO are impacted by climate processes occurring over much larger regions of the IO and tropical Pacific. Thus, we hypothesized that EDH in the IO focus regions (Figure 20) varies in response to global scale climate variations. We tested this hypothesis using composite analysis techniques, as discussed in the next section.

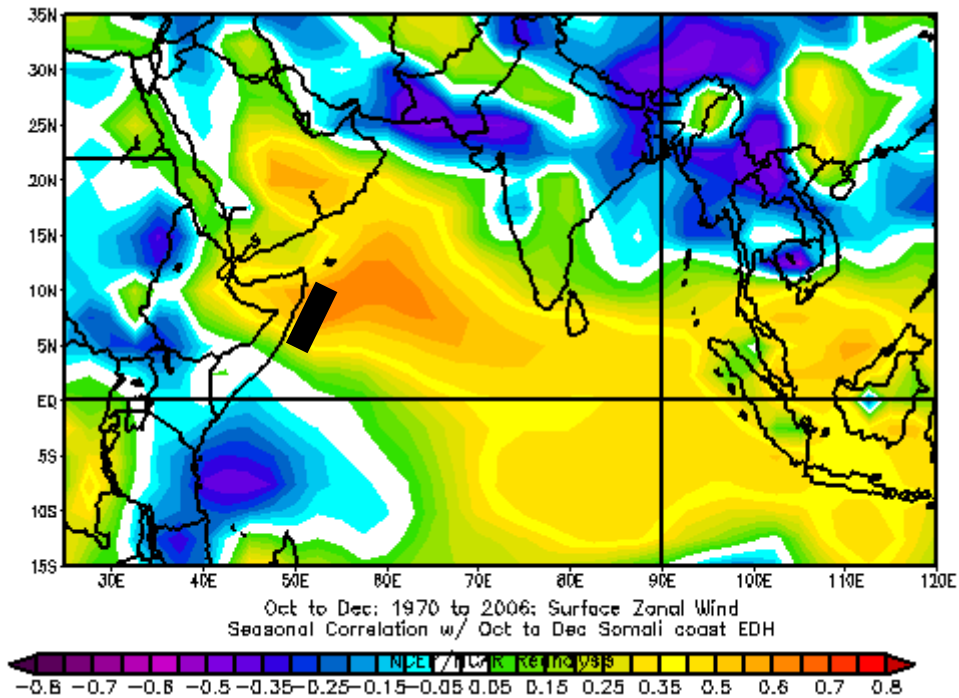


Figure 44. Correlation of our smart climatology EDH for the Somali coast region with surface zonal wind (u component of the wind) across the IO. Image produced using NCEP reanalysis data and the NOAA/ESRL Physical Sciences Division web site at <http://www.cdc.noaa.gov/>, using NCEP reanalysis data, (Kalnay et al., 1996) accessed September 2007.

1. Composite Analyses

Composite analyses were used to study the effects of ENSO and IOZM on EDH and its factors. The years and seasons composited were chosen based on the strength of their representative indices and the expectation of a homogenous response throughout a season based on previous studies, as discussed in Chapter 2.

a. DMI

Figure 45 displays the DMI time series created using NCEP reanalysis SST data and the methodology outlined in Chapter II. For comparison

the MEI (from the CDC MEI web site <http://www.cdc.noaa.gov/people/klaus.wolter/MEI/mei.html>, accessed September 2007) is also shown in Figure 45.

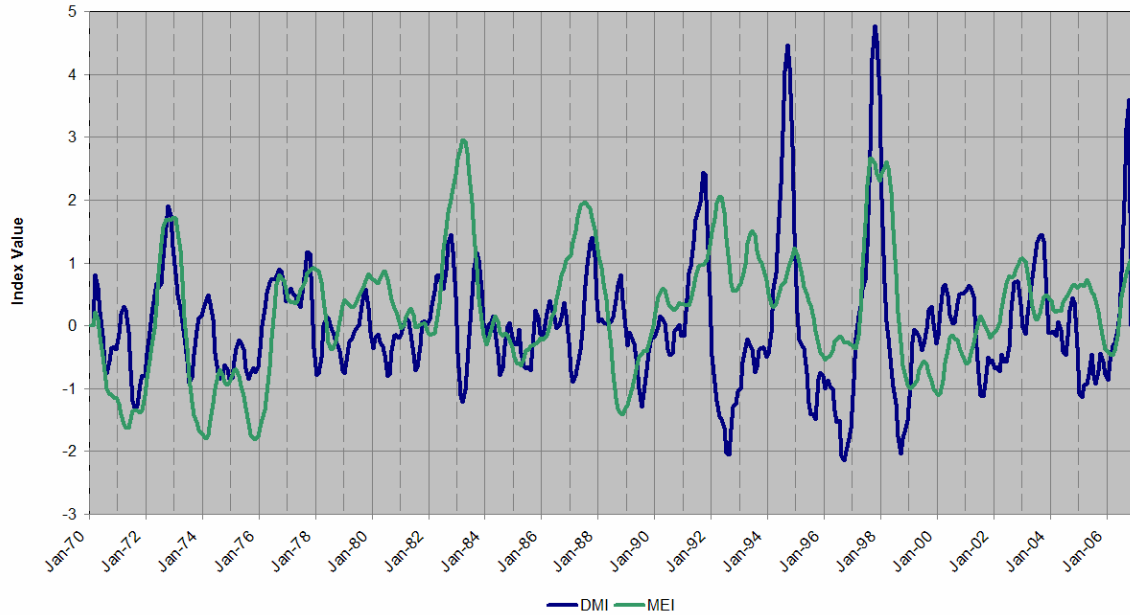


Figure 45. DMI created using NCEP reanalysis SST data and MEI (From: the CDC MEI web site <http://www.cdc.noaa.gov/people/klaus.wolter/MEI/mei.html>, accessed September 2007).

As discussed in Chapter 1, the IOZM occurs mainly during June-December. During these months, the three month period with the largest DMI magnitudes (+ and -) was August-September-October (ASO). The five most extreme years for both phases of the DMI over this season are listed at Table 3. The five most extreme years for EN and LN are also listed. For further information on the choice of MEI season see Chapter 2, section B1. Composite analyses were completed for each set of years listed in Table 3.

b. Composite Analysis Results

Separate composite analyses were conducted for EN, LN, positive IOZM, and negative IOZM. The positive IOZM and EN composites, and the negative IOZM and LN composites, have some years in common (Table 3;

Chapter I, section E). Thus, there are some similarities between these composites, along with some with some distinct differences (not shown). The EDH factor composites and the EDH composites for opposite phases of a climate variation (e.g., EN and LN, positive and negative IOZM; not shown), tend to be opposite to each other EDH values, but not completely opposite, indicating the response to the climate variations is not entirely linear. This is not surprising, given the complex nature of EDH and its sensitivity to small changes in several near-surface factors.

Table 3. IOZM and ENLN events selected based on DMI and MEI, respectively. Note that there is some overlap in the positive IOZM and EN years, and in the negative IOZM and LN years (see Chapter I, section E).

Top 5 IOZM events during August-September-October (ASO) season		Top 5 events ENLN events during October-November-December (OND) season	
Positive IOZM	Negative IOZM	El Nino	La Nina
1972	1971	1972	1970
1991	1992	1982	1971
1994	1995	1987	1973
1997	1996	1994	1975
2006	1998	1997	1988

c. Positive IOZM Composite Analysis Example

As an example of our composite results, the composite factors and composite EDH results for the ASO positive IOZM composite are presented in this section. The WS composite anomalies in Figure 46 are positive (negative)

where the positive IOZM composite WS is stronger (weaker) than the LTM WS. Note the positive WS anomalies to the south of the equator in the eastern IO, and the negative WS anomalies to the north of the equator.

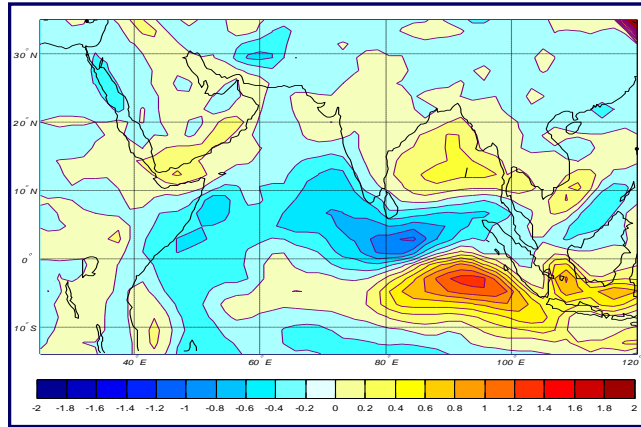


Figure 46. WS anomalies (ms^{-1}) for positive IOZM composite.

Figure 47 shows the composite anomalies for the other key EDH factors. Figures 47 a and b show a southeasterly to easterly vector wind anomaly in the eastern IO, and a negative SST anomaly near and to the west of the MC, consistent with the anomalous fields characteristic of the positive IOZM phase (Chapter I, section E). Figure 47 c and d show the corresponding positive RH and ASTD anomalies in the vicinity of the MC, as well as other anomalies responses across the IO.

The EDH anomalies for the positive IOZM composite show that during a positive IOZM event, EDH tends to be slightly higher than the corresponding LTM in the southeast IO and Bay and Bengal, and lower than the LTM just west of the MC, across much of the northern IO, in most of the Arabian Sea, the GOO, the Omani coast region, the eastern GOA, and the Somali coast region.

Based on our EDH-factor time series and correlation results (Chapter II, section C), we know the most significant factors affecting EDH at different times and locations. Thus, if a significant factor at a given location is strongly anomalous during the positive IOZM phase, then there should also be a

strong EDH anomaly at that location during the positive IOZM phase. For instance, we know that WS is the most significant positively correlated factor for EDH at Diego Garcia. Thus, we would expect some correspondence between the WS anomalies and the EDH anomalies in this region.

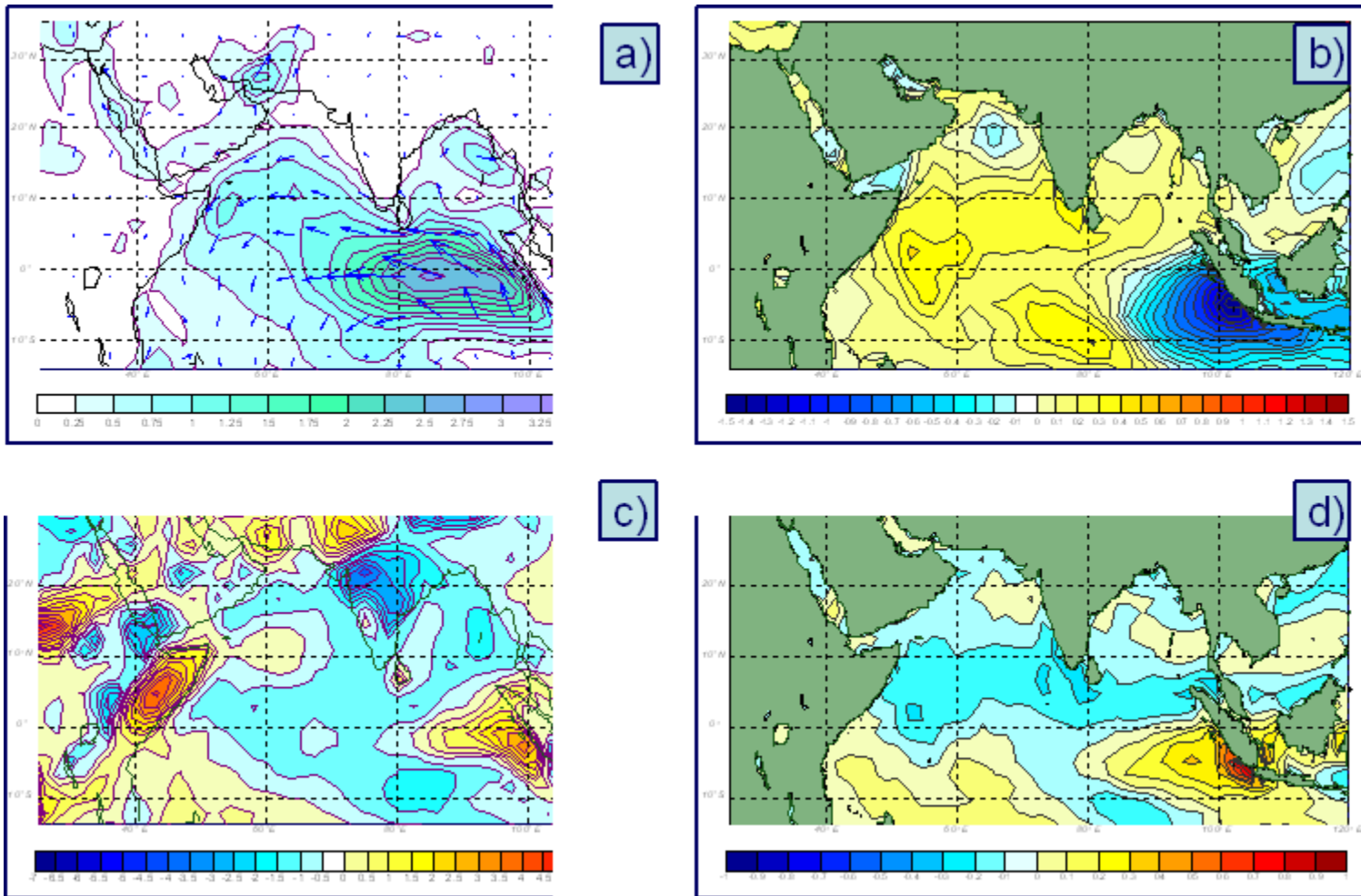


Figure 47. Anomalies for positive IOZM composite: (a) vector wind (ms^{-1}); (b) SST ($^{\circ}\text{C}$); (c) RH (%); and (d) ASTD ($^{\circ}\text{C}$).

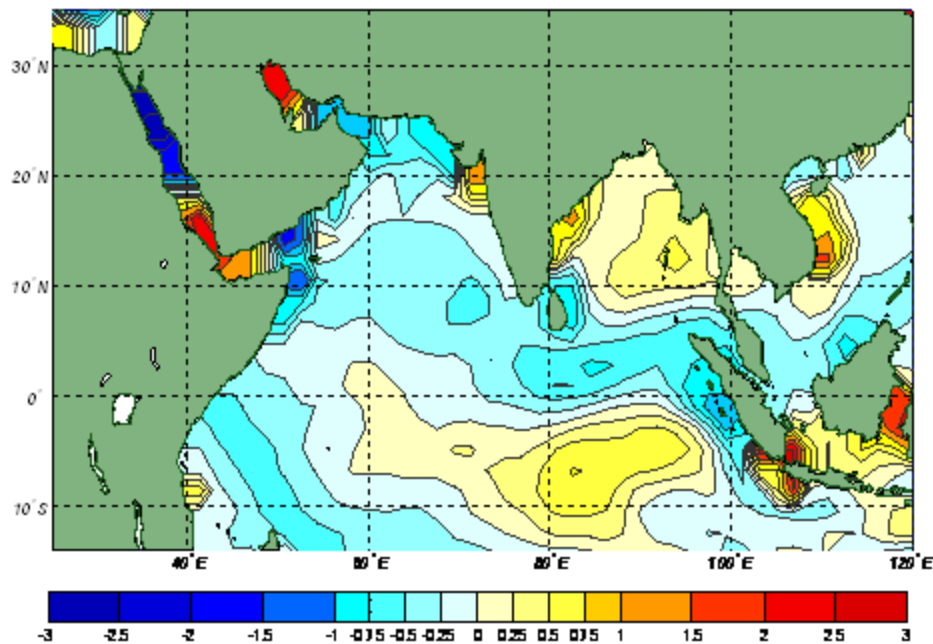


Figure 48. EDH anomalies (m) for positive IOZM composite.

A comparison of Figures 46 and 48 indicates positive WS and EDH anomalies in the Diego Garcia region and across a broader equatorial IO region. As another example, in the GOA, ASTD is a highly positively correlated factor with EDH (Chapter II, section C). Figure 47d shows negative ASTD anomalies in the eastern GOA where Figure 48 shows negative EDH anomalies. These and other composite results support our hypothesis that IOZM and ENLN events impact EDH in much of the tropical and northern IO and nearby seas.

The EDH anomalies in Figure 48 show large areas in which the EDH composite anomalies for positive IOZM events are less than 3 m. These are small anomalies, but they are an average of three months over five years, so the low values of anomalous EDH are not unexpected. For analyzing and forecasting the EDH anomalies for any particular positive IOZM event, the anomalies in Figure 48 should be used mainly to indicate the sign and general spatial pattern of the EDH anomalies. Similar conclusions hold for other climate

variations (e.g., negative IOZM events, EN, LN). It is also important to note that small changes in EDH can have large effects on radar ranges at certain radar frequencies, as discussed in the next section.

2. Extent of EDH Change due to Climate Variations

EDH anomalies for one month of one year are shown in Figures 49 and 50. These anomalies illustrate the extent of EDH anomalies for individual months. Note that the scales range from -10 m to +10 m. These anomalies show open ocean anomalies with magnitudes up to 2.5 m, and coastal anomalies with magnitudes up to 10 m.

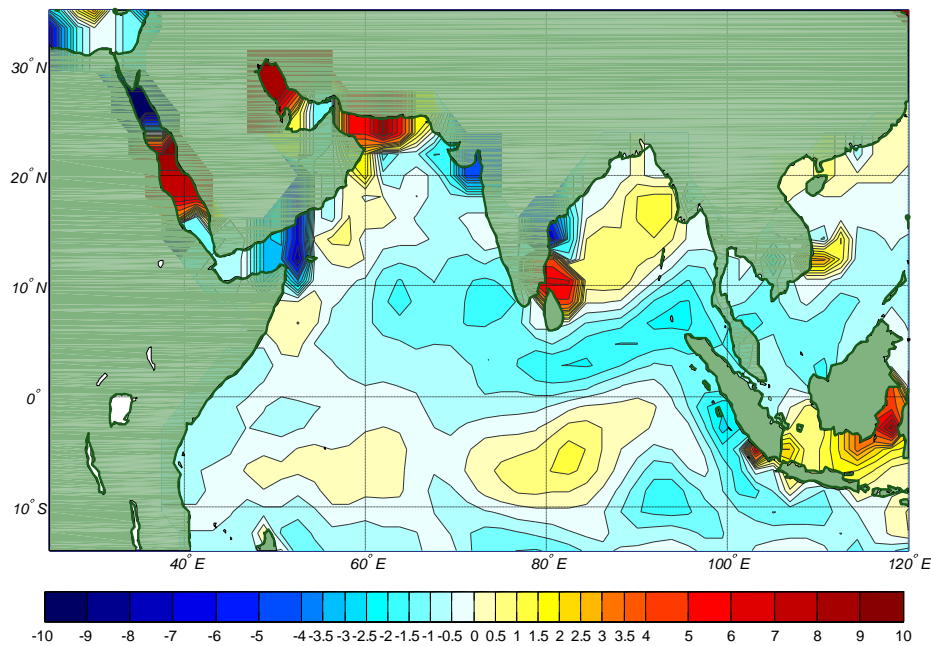


Figure 49. EDH anomaly (m) for September 1997.

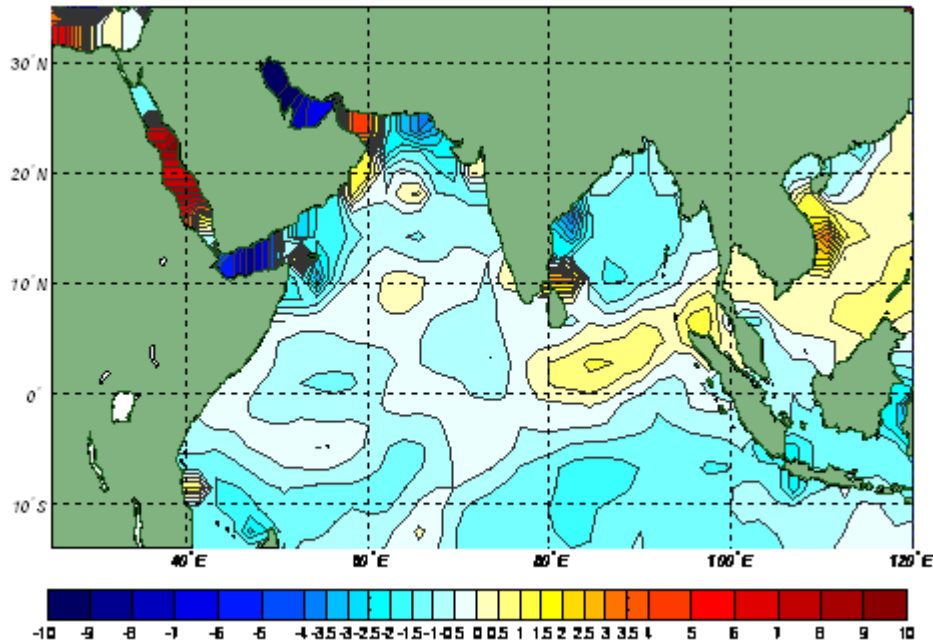


Figure 50. EDH anomaly (m) for September 1996.

During September 1997, there was both a positive IOZM event and an EN event, whilst in September 1996 there was a negative IOZM event. The EDH anomalies for these two months (Figures 49-50) are not completely opposite, nor do the September 1997 anomalies exactly match the positive IOZM composite anomalies (Figure 48). However, the overall anomaly patterns for the two individual months are opposite, and the September 1997 anomalies are very similar to those in the composite. These results highlight the complex nature of the EDH response to climate variations. To unravel some of these complexities and extract the most prevalent EDH changes corresponding to global scale climate variations, lag correlations between EDH in our focus regions and climate variation indices were calculated, as discussed in the next section.

F. CORRELATION TO CLIMATE VARIATION INDICES

The correlation between EDH in each focus region and the ENLN, IOZM, and NAO indices were calculated with, EDH lagging the indices by zero, one, and two months. The indices used were MEI for ENLN, DMI for IOZM, and NAOI for NAO (see Chapter II, section B). Tables 4 and 5 are summaries of these correlations.

Table 4. Correlations of EDH with MEI, DMI and NAOI for EDH lagging the climate indices by 0, 1, and 2 month lags, grouped by lag period. Significant correlations are indicated by colored cells (see color key). The absence of a significant correlation is indicated by white cells.

	MEI					DMI					NAOI				
	Jun	Jul	Aug	Sep	Oct	Jun	Jul	Aug	Sep	Oct	Jun	Jul	Aug	Sep	Oct
Zero Lag															
Diego Garcia															
Somali Coast															
GOA															
Omani Coast															
GOO															
SAG															
Lagged by 1 month (ie EDH lags variation)															
Diego Garcia															
Somali Coast															
GOA															
Omani Coast															
GOO															
SAG															
Lagged by 2 months															
Diego Garcia															
Somali Coast															
GOA															
Omani Coast															
GOO															
SAG															

Key		Positive correlation above 0.90 significance level
		Negative correlation above 0.90 significance level
		Positive correlation (correlation value 0.2)
		Negative correlation (correlation value -0.2)

These results show significant correlations of EDH with the climate variations for a number of months and at all lags. Overall, the strongest correlations are between EDH in the equatorial region, Diego Garcia, and the MEI and DMI (Tables 4-5). The Table 4 results are grouped according to the lag period and show that significant correlation occur at all lags. Table 4 also

highlights the seasons in which significant correlations occur for a given lag; for example, September to February for the MEI, and October to December for the DMI, for zero lag,. Significant correlations with the NAOI are more sporadic and generally tend to be negative correlations. Vorhees (2006) concluded that for southwest Asia there a reversal in the sign of the anomalous response to a given climate variation phase often occurred from autumn to winter. Some evidence of this is seen in the reversal in the sign of the correlations from autumn to winter in the Table 4-5 results (e.g., for the Somali coast and Gulf of Aden).

Table 5. Correlations of EDH with MEI, DMI and NAOI for EDH lagging the climate indices by 0, 1, and 2 month lags, grouped by focus region. Significant correlations are indicated by colored cells (see color key). The absence of a significant correlation is indicated by white cells.

LOCATION	LAG EDH lags variation	MEI					DMI					NAOI														
		Jun	Jul	Aug	Sep	Oct	Nov	Dec	Jan	Feb	Mar	Apr	May	Jun	Jul	Aug	Sep	Oct	Nov	Dec	Jan	Feb	Mar	Apr	May	
Diego Garcia	0 lag																									
	1 month lag																									
	2 month lag																									
Somali Coast	0 lag																									
	1 month lag																									
	2 month lag																									
GOA	0 lag																									
	1 month lag																									
	2 month lag																									
Omani Coast	0 lag																									
	1 month lag																									
	2 month lag																									
GOD	0 lag																									
	1 month lag																									
	2 month lag																									
SAG	0 lag																									
	1 month lag																									
	2 month lag																									

Key	Color	Description
	Orange	Positive correlation above 0.90 significance level
	Teal	Negative correlation above 0.90 significance level
	Yellow	Positive correlation (correlation value 0.2)
	Light Blue	Negative correlation (correlation value -0.2)

Table 5 displays the same results as Table 4 but grouped by focus region. It clearly illustrates that significant correlations exist when a lag of 1 or 2 months is applied (note the ‘marching backward’ pattern for the zero, one, and two month lagged correlations with the MEI and DMI). This indicates that there should be some predictability of EDH based on IOZM and ENLN indices. Correlations with

the NAOI show some significant correlations (e.g., with EDH in the GOA) but relatively little spatial or temporal consistency. The relative lack of temporal consistency may reflect the relatively strong intraseasonal character of the NAO compared to the strong interannual character of ENLN and the IOZM..

Overall, the correlations between EDH and the climate indices indicate a potential for skillful forecasts of EDH at lead times of weeks to months based on ENLN, IOZM, and the NAO (cf. Hanson 2007; Moss 2007; van den Dool 2007).

G. SENSOR PERFORMANCE IMPACTS

1. Introduction

Environmental information is one factor considered during military planning, for both tactical and strategic timescales. The utility of environmental information depends not only on its relevance to the scenario but also on the manner in which it is presented. This section examines how the EDH variations impact radar system performance and how this information can be most effectively presented.

a. Smart Climatology Environmental Assessment Surfaces

Geographic plots of EDH and its factors are examples of environmental assessment surfaces, as defined by the Battlespace on Demand (BonD) concept (McGee 2006), and of additional military layers within the NATO Recognized Environmental Picture concept (Great Britain. Ministry of Defence, 2004; United Kingdom Hydrographic Office, 2007). We have used smart climatological methods to derive monthly LTM EDH values and EDH variations from their LTM values due to climate oscillations. These results have been graphically displayed and are examples of smart climatological environmental assessment surfaces. These surfaces were also created for the factors that determine EDH (WS, Ta, SST, ASTD, RH).

b. Vertical Coverage Diagrams

Vertical coverage diagrams (VCDs) are height versus range plots of propagation loss for a given emitter, or of the probability of detection for a given scenario as defined by radar and target information. Figure 51 shows two examples of a VCD, for (a) a 'standard' vertical M profile with no evaporation duct and (b) an M profile with an evaporation duct. These examples illustrate: (1) how low-level propagation loss decreases, and thus detection ranges increase, for a strong evaporation duct; and (2) that the near-surface ED refractivity feature has detection range implications at heights well above the surface. If the propagation loss threshold for target detection (normally set to a 90% probability of detection level) is known, then a detection range can be found and graphical displays of detection range can be plotted for a target at a chosen height. In the following sections, VCDs are used to assess the operational relevance of the smart climatological products we have developed.

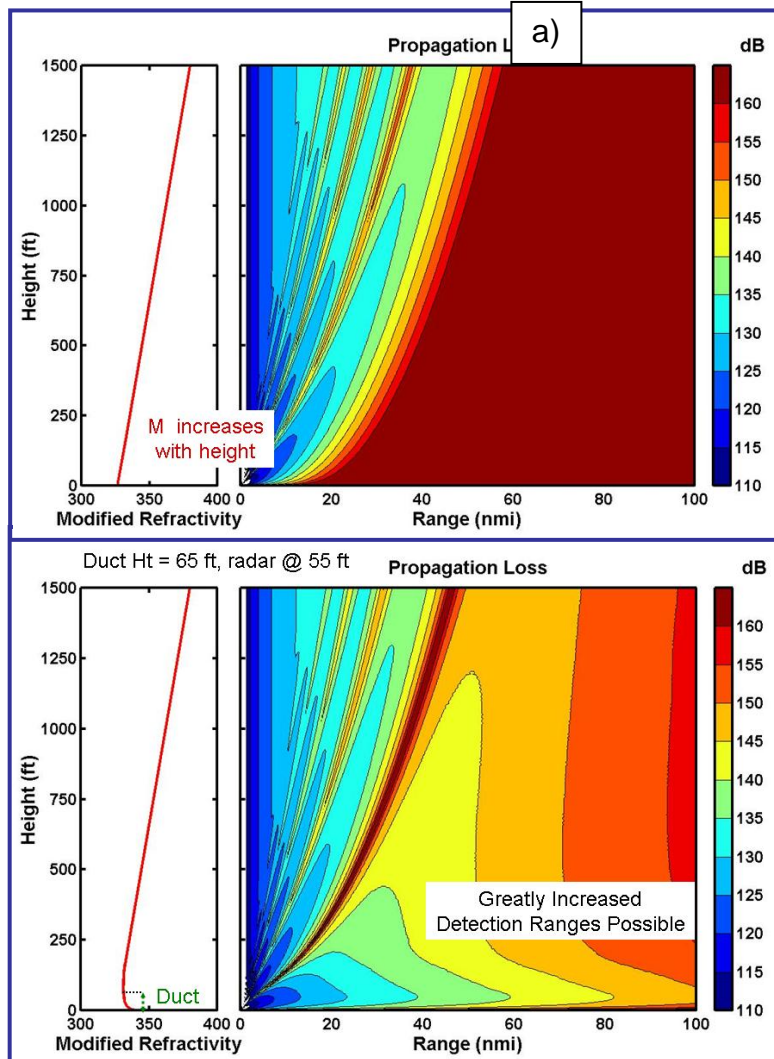


Figure 51. Vertical coverage diagrams of propagation loss for: (a) standard atmosphere with no ED; (b) atmosphere with ED. From Davidson (2006).

2. Smart Climatology Performance Surfaces

a. Surface Detection Range

Performance surfaces represent a sensor's performance for a given set of environmental conditions that affect the sensor's performance; for example, surface radar detection range for forecasted EDH conditions and for a

given scenario. Figure 52 shows an example of a performance surface produced for this study for surface radar detection ranges based on LTM September EDH values taken from our smart EDH climatology.

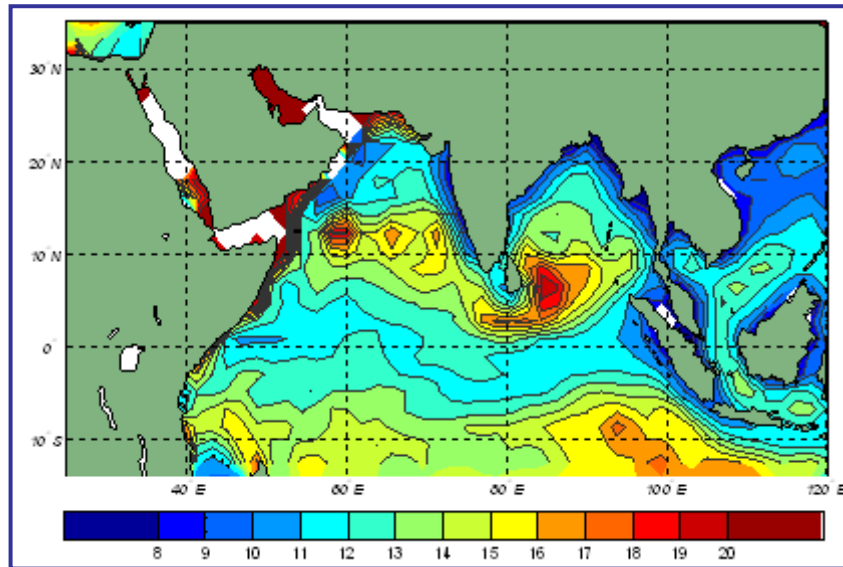


Figure 52. Estimated surface radar detection ranges (km) based on September LTM EDH from our smart EDH climatology, for a C-band radar at 30 ft and detection threshold of 150 dB.

The ranges shown in Figure 52 are based on monthly LTM values of the EDH factors that were used to reproduce an evaporation duct M profile which was appended to a standard refractive atmospheric profile. These M profiles were then input into APM to compute propagation loss curves at a given height, from which surface radar detection ranges were estimated (see Chapter I, section B3). It is feasible to calculate and then average range information, following a similar process as used for EDH; however, this has a high computational cost and was not feasible for this study.

Climate variations affect EDH across the IO basin and therefore affect detection ranges. To illustrate the effect of a climate variation on ranges during an active climate variation phase, we computed surface detection ranges from the surface factor data for September 1997 (Figure 53). The corresponding

surface detection range anomaly is (Figure 54) shows that climate variations can have a significant effect on surface detection ranges. In much of the IO, the range anomalies represent deviations from the LTM ranges of 25% or more.

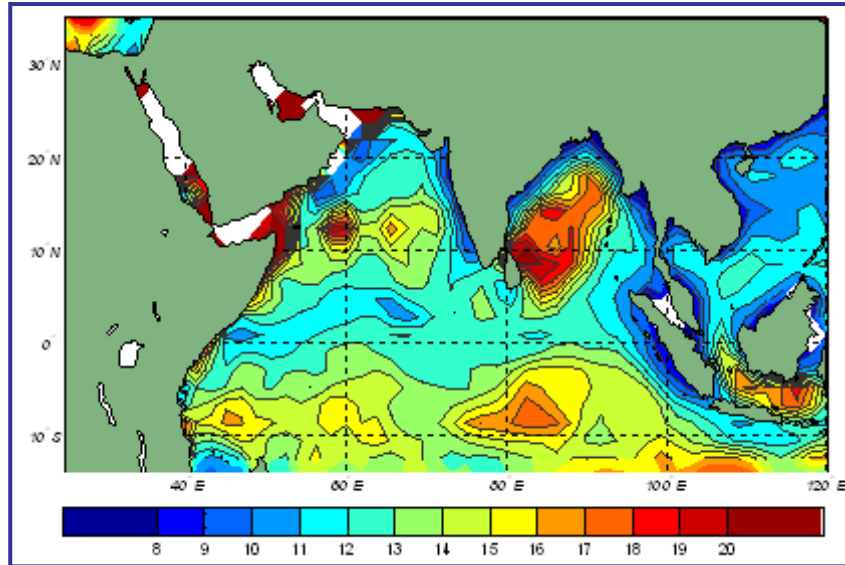


Figure 53. Estimated surface radar detection ranges (km) based on September 1997 EDH, for a C-band radar at 30 ft and detection threshold of 150 dB. Compare to Figure 52.

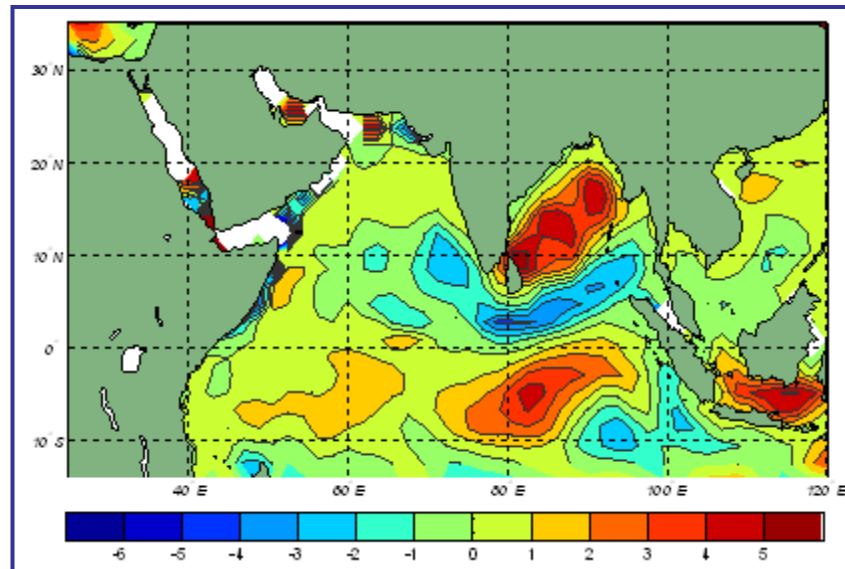


Figure 54. Estimated surface radar detection ranges (km) anomalies for September 1997 EDH, for a C-band radar at 30 ft and detection threshold of 150 dB. Compare to Figures 52-53.

b. Cut Off Frequency

Performance surfaces for CoF illustrate the effect of EDH on sensor performance for varying frequencies, and provide insight into which suite of sensors would most benefit from medium and long lead EDH forecasts. Figure 55 is an example of a smart climatology performance assessment surface for CoF. As stated in Chapter I, although the name alludes to a definite frequency the 'leaky' nature of the duct means that the CoF gives an indication of the frequency band and higher frequencies that will be particularly affected by the presence of an ED of defined height.

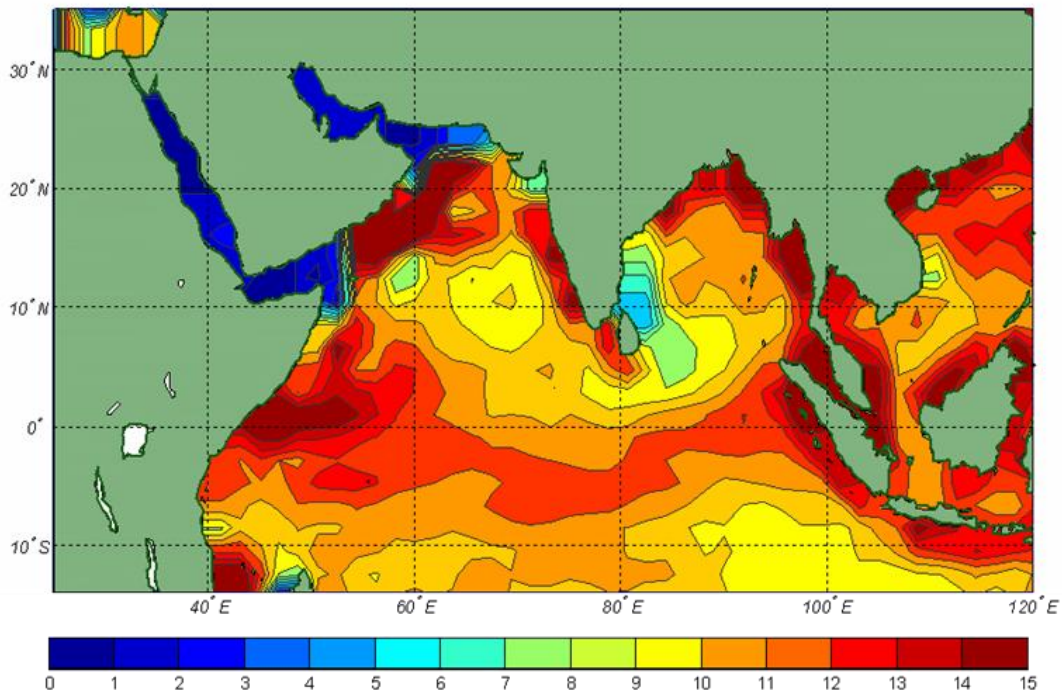


Figure 55. Estimated CoF (GHz) based on September LTM EDH from our smart EDH climatology.

c. Limitations

The sample performance surfaces shown in the preceding section are based on evaporation ducts only and do not account for surface-based ducts. Figure 56 shows VCDs for M profiles with a large surface duct and: (a) no evaporation duct; and (b) with an evaporation duct. The exact nature of a

surface duct is dependent on its height and structure. Figure 56a shows that increased detection ranges are possible at some distance from the radar, with a skip zone in between. As the height of the duct decreases, the skip zone will also decrease, until at some height there is full surface coverage. If there is an evaporation duct as well, then surface detection ranges will extend into the skip zone, thus increasing surface coverage. Within our considered area, surface ducts are prevalent in areas of subsidence, for example, on the poleward flanks of the trade wind areas and northeast monsoon regimes. However, the EDH impact remains very important for extended near-ship surface-detection ranges of small targets, such as submarine periscopes and snorkels, small boats, and dhows.

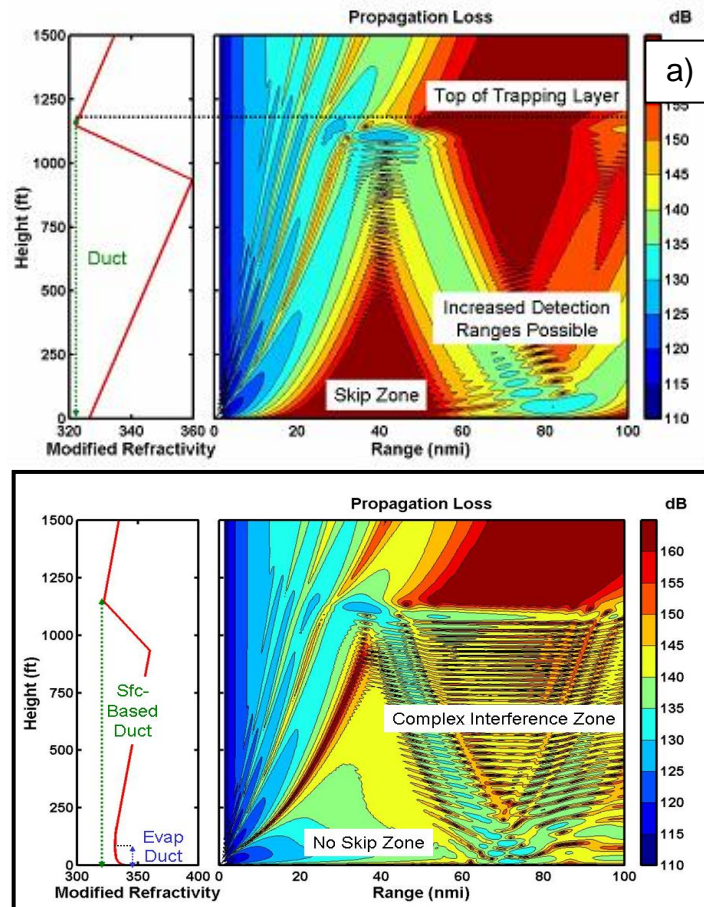


Figure 56. Vertical coverage diagrams of propagation loss (a) standard atmosphere with no ED, (b) atmosphere with ED. From Davidson (2006).

d. Summary

Overall, the results presented in Chapter III: (1) show that state-of-the-art LTM climatological performance surfaces can be produced using smart climatology data and methods; and (2) suggest that, for areas in which EDH is well correlated with predictable climate variations, skillful forecasted performance surfaces based on the occurrence of these variations could be produced at weekly to monthly lead times. These LTM and medium to long lead forecasted performance surfaces have the potential to significantly improve upon existing climatology products, and thus to improve medium to long term planning.

THIS PAGE INTENTIONALLY LEFT BLANK

IV. CONCLUSIONS AND RECOMMENDATIONS

A. SUMMARY

This study utilized smart climatology methods and a reanalysis dataset to produce improved LTM EDH values for the tropical and northern IO, and nearby seas. Monthly and seasonal map displays of this smart EDH climatology were generated. The temporal and spatial resolution of the smart EDH climatology is far greater than the present U.S. Navy EDH climatology. EDH was computed for six-hourly surface reanalysis data for 37 years, from 1970 to 2006, on a horizontal ~210 km by ~210 km grid. As EDH is the best parameter for quantifying near-surface microwave propagation, these results can also improve LTM spatial and temporal detection range climatologies, as demonstrated for a sample radar/target scenario.

The sensitivity of EDH to different surface factors (SST, Ta, humidity, wind) varies with location and season. Correlations of EDH with its component factors identify which factor(s) would be the key ones to monitor, analyze and forecast, and thus lead to improved analyses, forecasts, and forecast uncertainty estimates. Some of the key EDH factors for different seasons and regions of the IO that were identified in this study are:

- ASTD, throughout the year in the SAG, GOA and GOO regions
- RH, in April-September, in the GOO
- Ta and u component of wind, in January-May, in the GOA
- u component of wind, in September to November, in the GOA
- WS, throughout the year, in equatorial regions, such as Diego Garcia
- RH, in July-December, in equatorial regions
- Ta and SST, in October-January, in equatorial regions
- SST and RH, in May-September (southwesterly monsoon period), in western boundary regions (e.g., GOO and Somali coast regions)

Based on analyses of the GOO and Somali coast regions, EDH during the coastal upwelling season was found to be insensitive to ASTD, despite Ta being slightly greater than SST.

This study has determined that climate variations influence EDH values in the IO. Composite analyses completed for EDH and its factors, using the top 5 events for both phases of ENLN and IOZM, show that there are links between EDH, its factors and these climate variations. Correlations of regional EDH with ENLN, IOZM and NAO indices support these findings and identified spatial and temporal variations in the impacts of these climate variations. As EDH fluctuates with the seasonal cycle and due to the impact of climate variations, surface detection ranges also vary. EDH often lags the climate variation by 1-2 months, thus EDHs and surface detection ranges trends may be predictable at medium to long range lead times.

Results from this study are displayed as geographical plots and provide the first smart climatological EDH environmental assessment surfaces and examples of smart climatology performance surfaces. Thus this study has provided climatological information for: (1) the first and second tiers within the U.S. Navy's Battlespace on Demand (BonD) conceptual triangle (McGee 2006); (2) additional military layers within NATO's Recognized Environmental Picture; and (3) decision analysis products in Tier 3 of the BonD concept. Figure 57 is a flow diagram illustrating how our results fit into the BonD concept. It also shows a summary of recommendations, discussed in the next section, with respect to this concept.

This study provides 'proof of concept' for the use of smart climatology in environmental and performance assessments, and demonstrates the value of smart climatology for improving military climatologies. There are, however, a few caveats that should be noted. Firstly, data which comes from grid boxes that encompass both land and sea are unlikely to provide accurate EDH values and have not been used in this study. Rather, seaward values of EDH have been mapped towards the coast. Thus, in coastal grid boxes that contain both land

and sea areas, our EDH values should be used with caution. Secondly, the surface detection ranges shown in this study are based on evaporation duct only and do not account for surface-based ducts. Finally, the results of EDH derived from reanalysis data would, ideally, be 'ground truthed' before being used operationally (in practice, such ground-truthing will probably be difficult to conduct, except for very limited areas and periods).

B. AREAS FOR FURTHER RESEARCH

This study has improved the spatial resolution of EDH climatology by a factor of ~25 over the existing climatology. An even higher resolution reanalysis dataset would further increase spatial resolution, reduce the effect of coastal limitations, and enable a more developed analysis in the gulfs. NCEP is expected to release a global coupled atmospheric-oceanic reanalysis in 2008-2009, at 0.5 x 0.5 degree resolution for the atmosphere, and 0.25 x 0.25 degree resolution for the ocean. This reanalysis data should greatly reduce the uncertainty in a smart EDH climatology and provide information for a finer dynamical analysis of the effect of the land-sea boundary on EDH, for example the extent and range of the sea breeze effect.

Values for EDH were computed at six hour intervals from January 1970 through December 2006, and this data was then used to calculate monthly mean EDH values. Smart climatology methods were used to analyze this monthly data, and produced significant results (e.g., analyses of temporal and spatial variations in EDH and the factors that determine EDH, analyses of the impacts of climate variations on EDH). Further analysis of the six-hourly data would provide information on finer temporal effects, for example diurnal effects. Correlations using diurnally similar data should also provide some increased significance levels and a more thorough understanding of the dynamical influences.

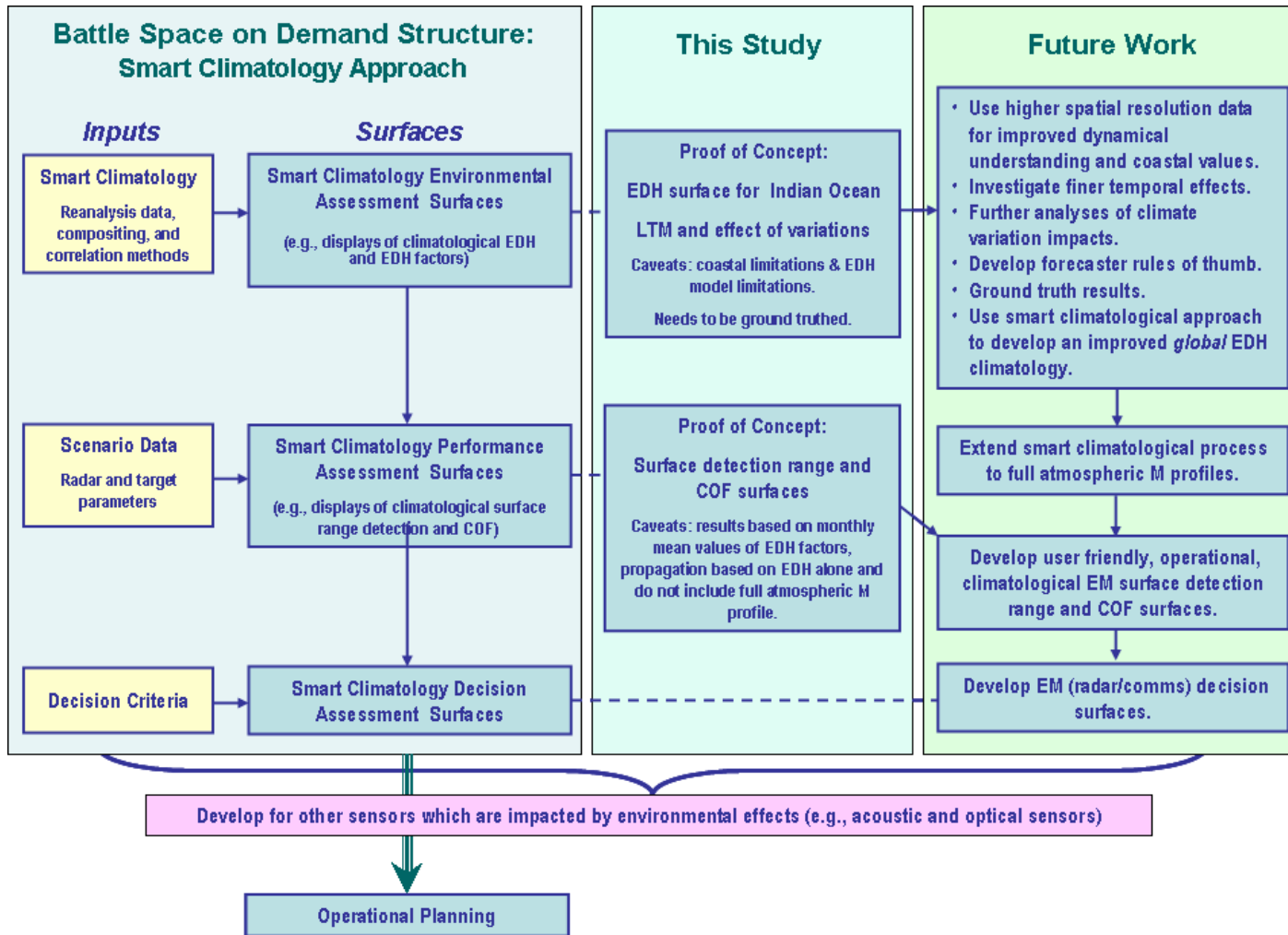


Figure 57. Flow diagram of results and of recommendations for future work within the BonD concept.

Conditional climatologies could also be constructed for different climate regimes (e.g., the variation of EDH as the Somali jet strength fluctuates or during a monsoon break period). Backward and forward climate analyses could also be used to provide 'smarter correlations' for specific factors and areas (e.g., the effects of wind direction on EDH in the GOO). Backward climate analyses start with regional climate variations and identify connections to larger scale climate variations. Forward climate analyses start with large scale climate variations and identify connections to regional climate variations.

ENLN, IOZM and NAO climate variations have been shown to affect EDH in the IO, particularly over some months or seasons. This study could be extended to include the effect of the Madden-Julian Oscillation, monsoon effects, different ENLN magnitudes, differences between combined or separate ENLN and IOZM years, and relationships to surface currents and thermocline depths. Ideally these results would then be developed into a correlation plotting tool for user-selected data (e.g., EDH during IOZM, ENLN events). Our studies also demonstrated that EDH has periods of significant correlation when lagged one or two months behind the climate variation indices. This suggests that there is potential to predict EDH and surface radar detection ranges based on climate variations. The theses by Hanson (2007) and Moss (2007) used smart climatology to develop prototype statistical long term prediction tools for precipitation and surface temperature over areas of southwest Asia. A similar process could be used to predict EDH variation at medium and long range lead times.

This study provides a sound basis for forecaster knowledge of EDH and near-surface propagation conditions. Superior information and forecaster 'rules of thumb' could be developed for specific areas of operational interest by combining higher spatial and temporal resolution with more analysis, including the use of backward smart climatology methods.

The existing EDH climatology and our monthly mean LTM values show similar temporal patterns; however, there is a consistent magnitude difference. This difference is due to different datasets and models being used in the development of each climatology. EDHs computed with NCEP reanalysis data and the NPS ED model should be ground-truthed. Unfortunately a year's worth of data from one buoy does not necessarily represent the full range of climatological variability for the large scale environment in which the buoy is located. Numerous buoys within a grid box area are required to provide confirmation that the NCEP fields are providing data that is accurate enough for use in the EDH model, particularly in areas of occasionally stable conditions.

EDH is an excellent parameter for providing refractive information for near-surface propagation. However in regions where deep surface ducts also exist, EDH will not be the only factor that determines near-surface propagation. Ideally EDH climatology would be combined with a full vertical atmospheric refractivity profile and thus provide accurate surface detection ranges in the presence of deep surface ducts and ranges throughout the atmosphere. The benefit of refractivity based on modeled vertical resolution has not been investigated in this study, but should be pursued in future studies.

This study provides a proof of concept for a smart climatological approach to develop an improved *global* EDH climatology. The use of geographical plots to display the data illustrate that it could easily be developed into an environmental assessment surface or additional military layer, thus providing the information in an operational frame. Accuracies of EDH computed by the EDH model vary with changing environmental conditions and input precision; thus, sensitivity assessment plots would provide the user with useful information about uncertainty and confidence in EDH products.

Sensor performance assessments are operationally useful when they are easy to use and provide the command with the required information at the correct time. A user interface needs to be developed to allow operational personnel to efficiently manipulate scenario and climatology inputs to produce a desired outcome.

This smart climatology approach to providing long term climatological values and forecasts should be extended to other environmentally sensitive sensors, such as optical and acoustic sensors.

THIS PAGE INTENTIONALLY LEFT BLANK

APPENDIX A.

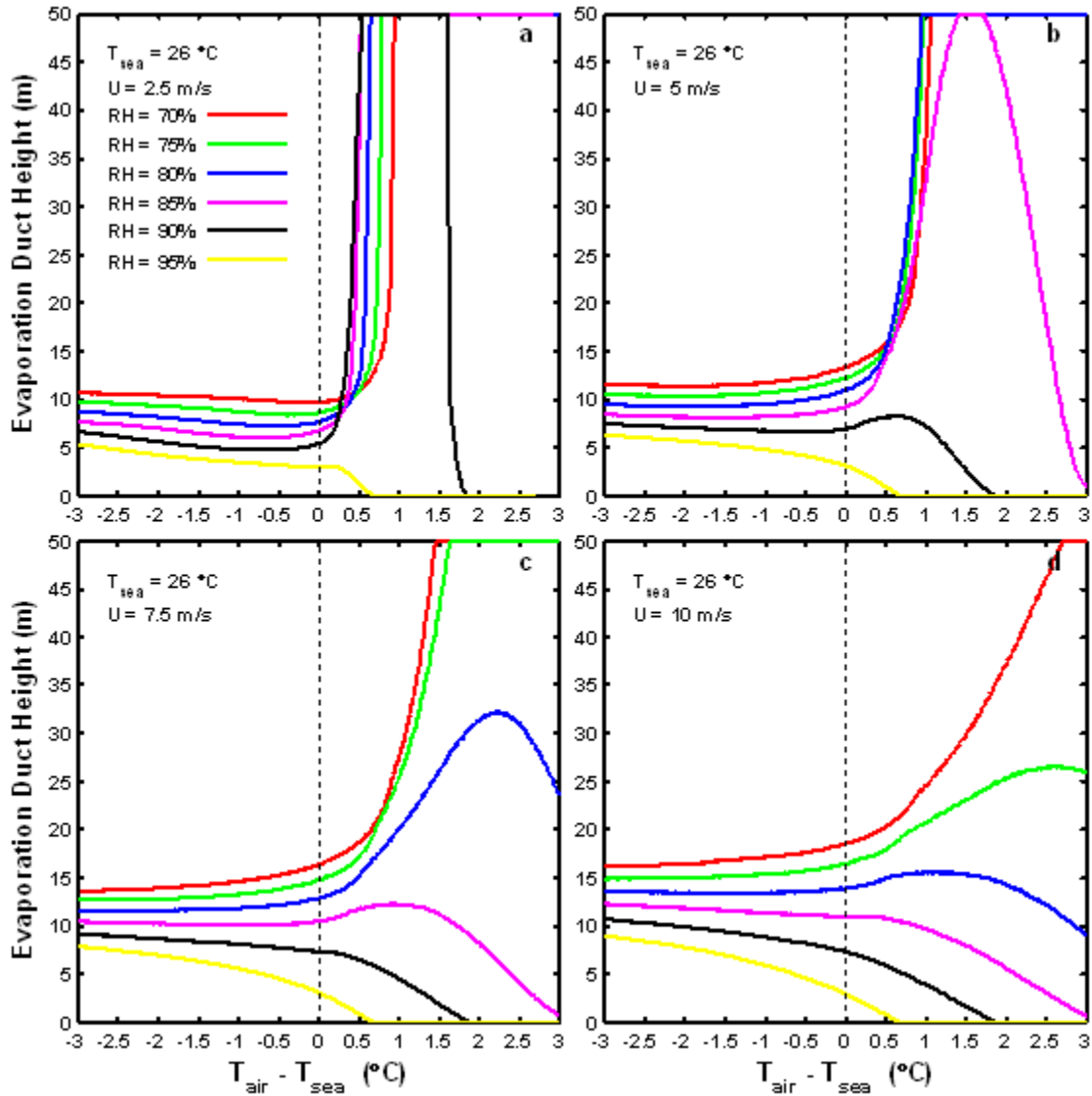


Figure 58. EDH computed by the NPS model versus ASTD for six different relative humidity values (six colored curves in each panel) and four different wind speed values (four panels). (From: Frederickson (2007)).

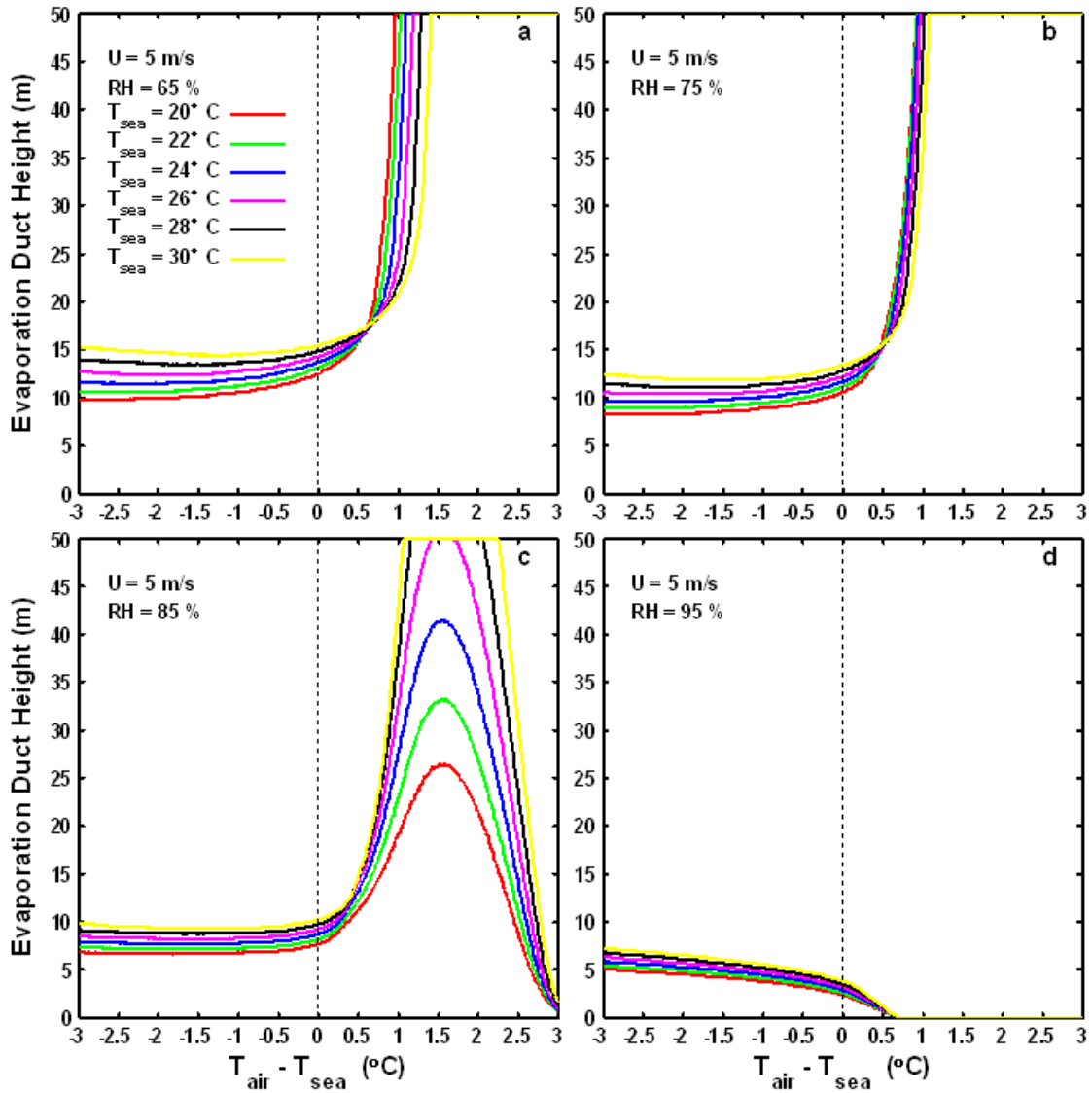


Figure 59. EDH computed by the NPS model versus ASTD for six different SST values (six colored curves in each panel) and four different relative humidity values (four panels). (From: Frederickson (2007)).

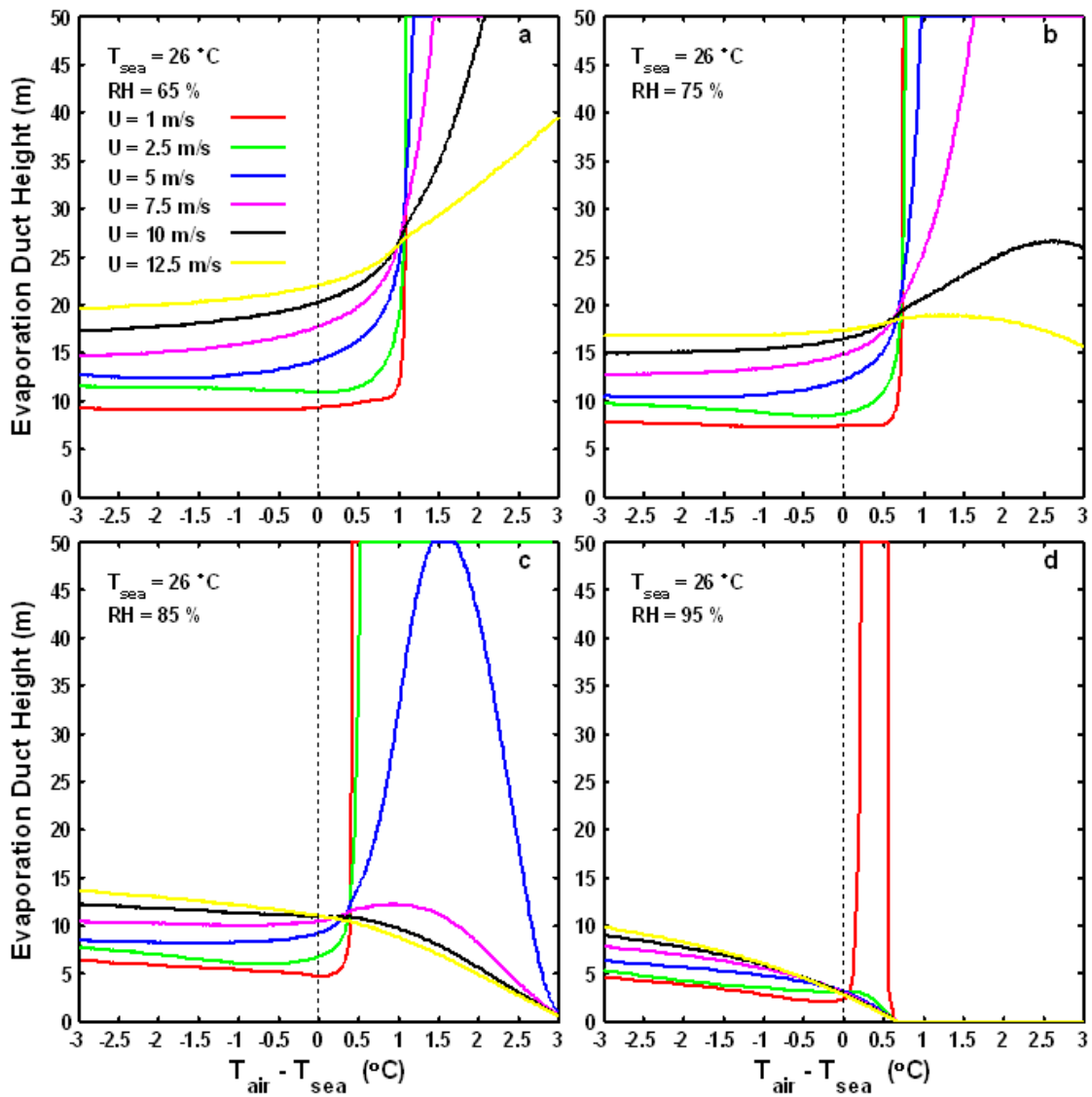


Figure 60. EDH computed by the NPS model versus ASTD for six different wind speed values (six colored curves in each panel) and four different relative humidity values (four panels). (From: Frederickson (2007)).

THIS PAGE INTENTIONALLY LEFT BLANK

APPENDIX B.

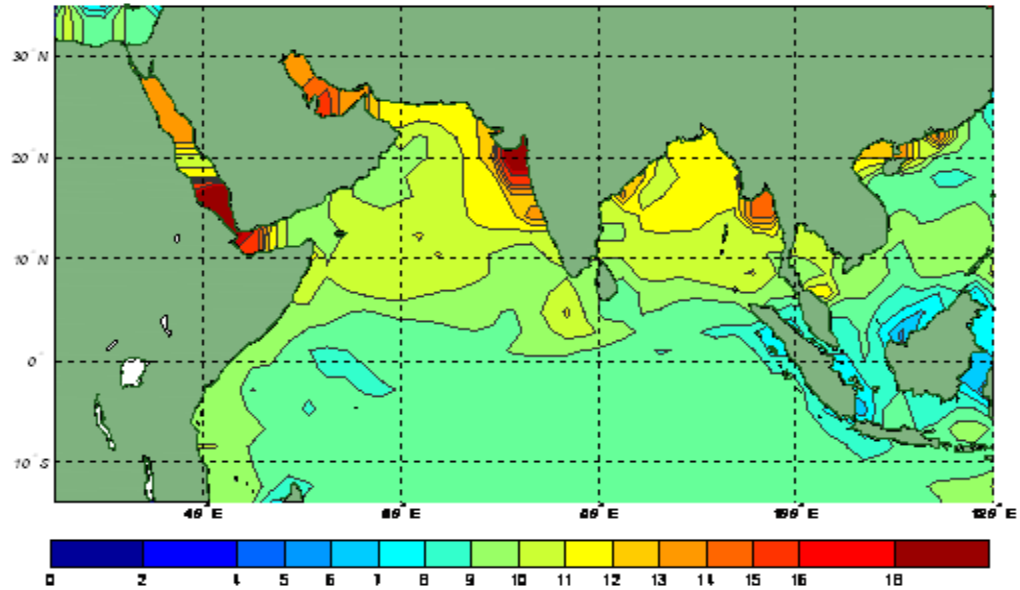


Figure 61. LTM EDH (m) for January. Note coastal caution (Chapter III, section A).

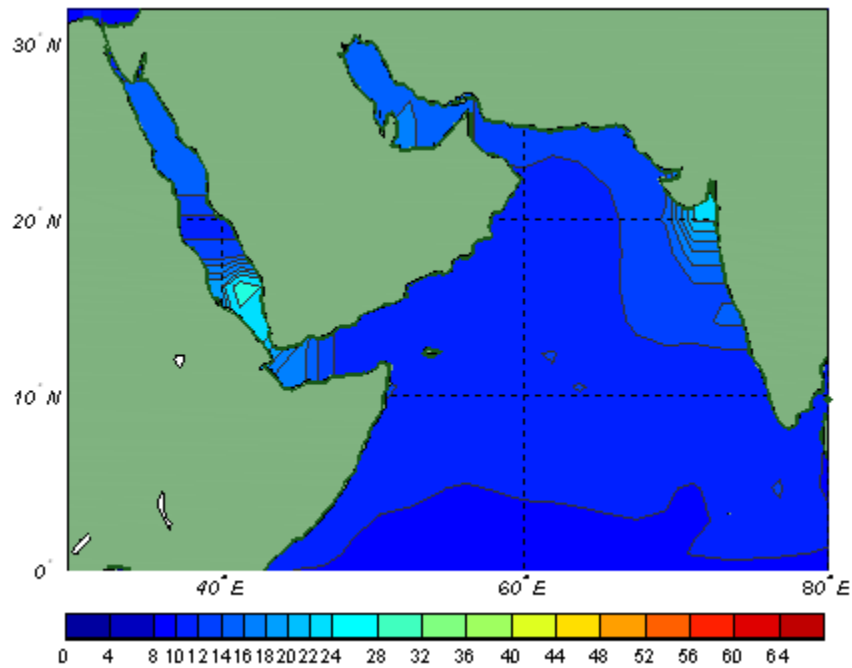


Figure 62. LTM EDH (m) for January for NW IO. Note coastal caution (Chapter III, section A).

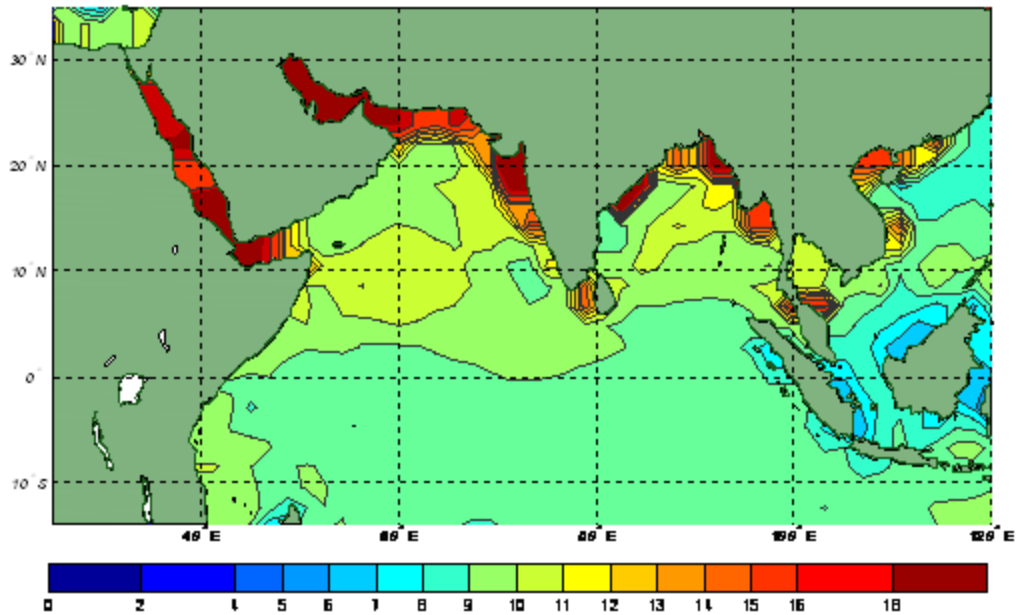


Figure 63. LTM EDH (m) for February. Note coastal caution (Chapter III, section A).

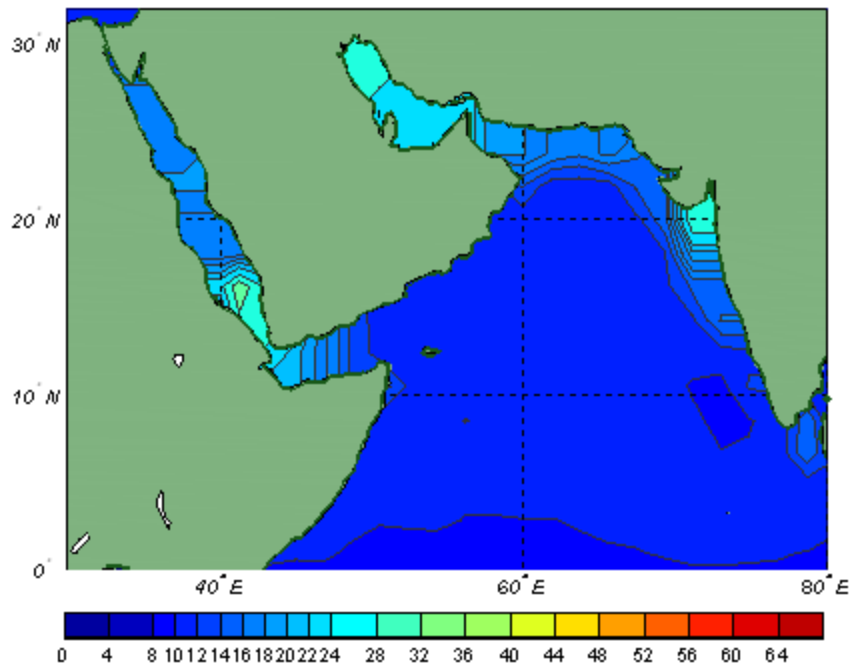


Figure 64. LTM EDH (m) for February for NW IO Note coastal caution (Chapter III, section A).

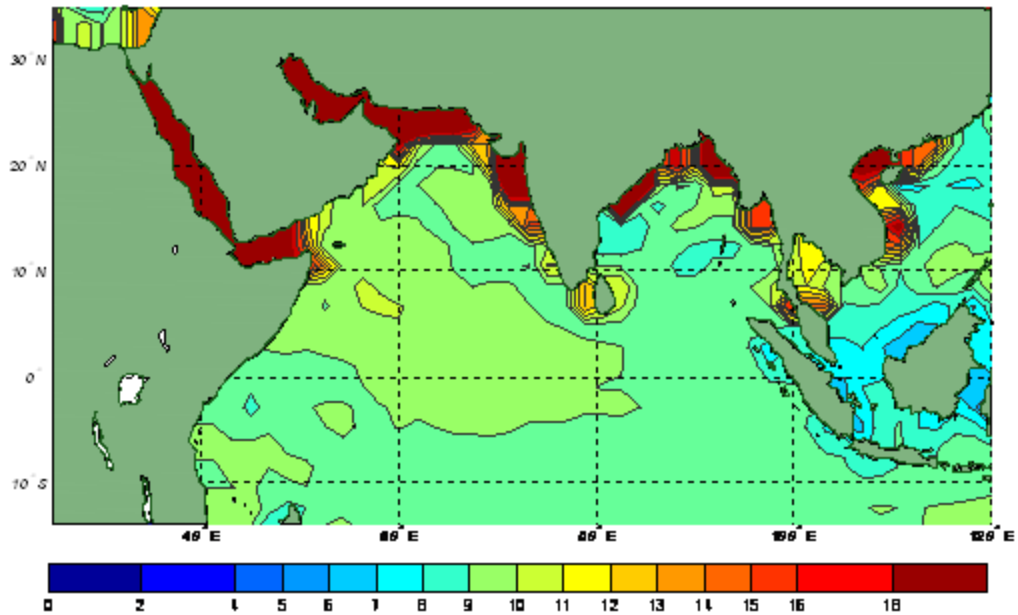


Figure 65. LTM EDH (m) for March. Note coastal cautions (Chapter III, section A).

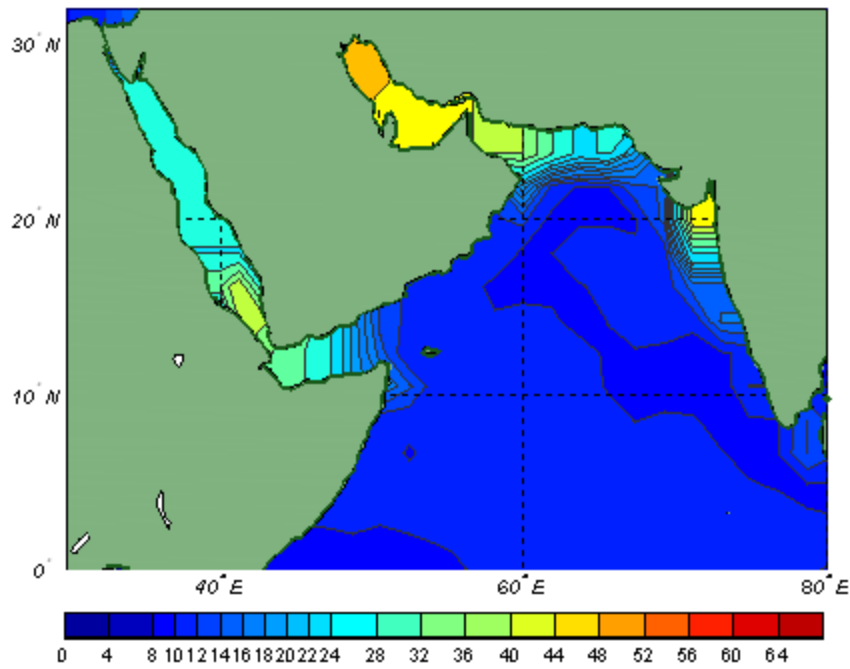


Figure 66. LTM EDH (m) for March for NW IO. Note coastal cautions (Chapter III, section A).

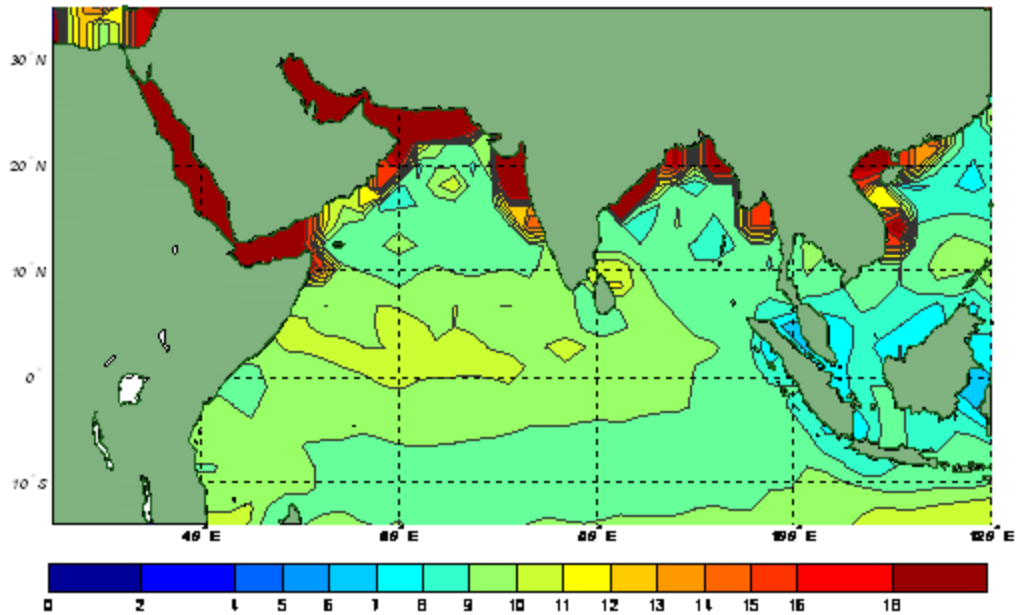


Figure 67. LTM EDH (m) for April. Note coastal caution (Chapter III, section A).

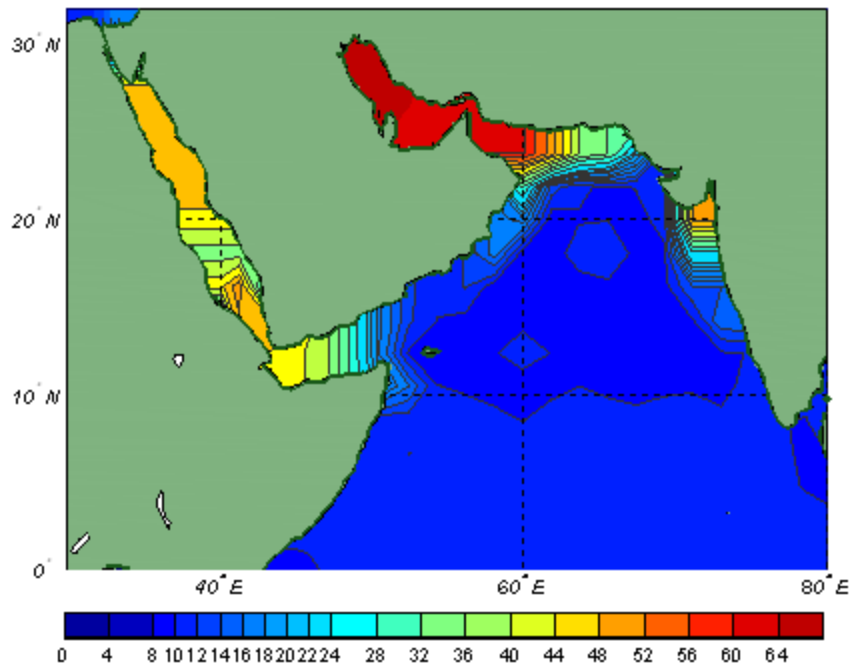


Figure 68. LTM EDH (m) for April for NW IO. Note coastal caution (Chapter III, section A).

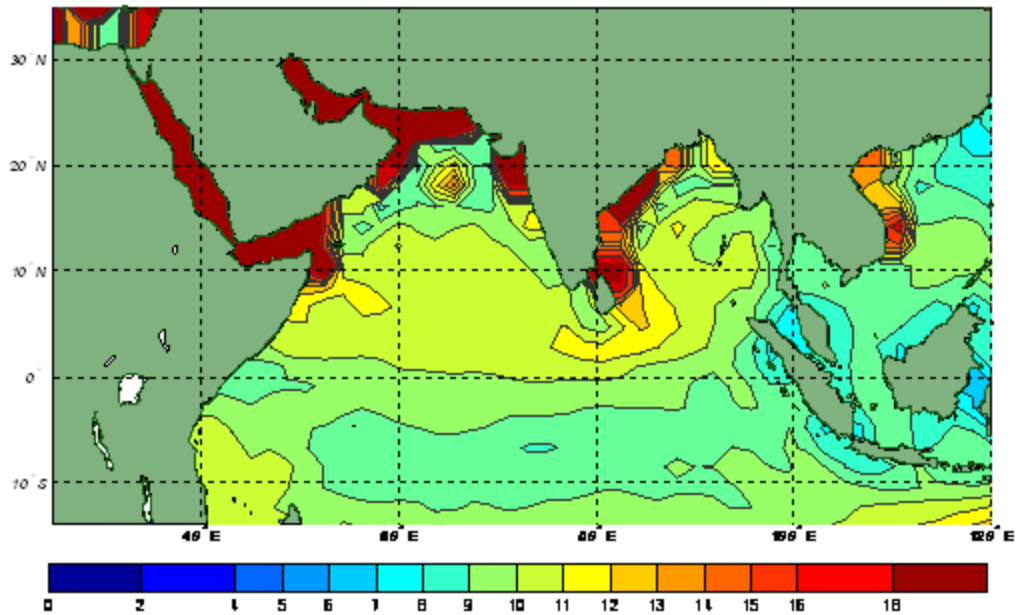


Figure 69. LTM EDH (m) for May. Note coastal caution (Chapter III, section A).

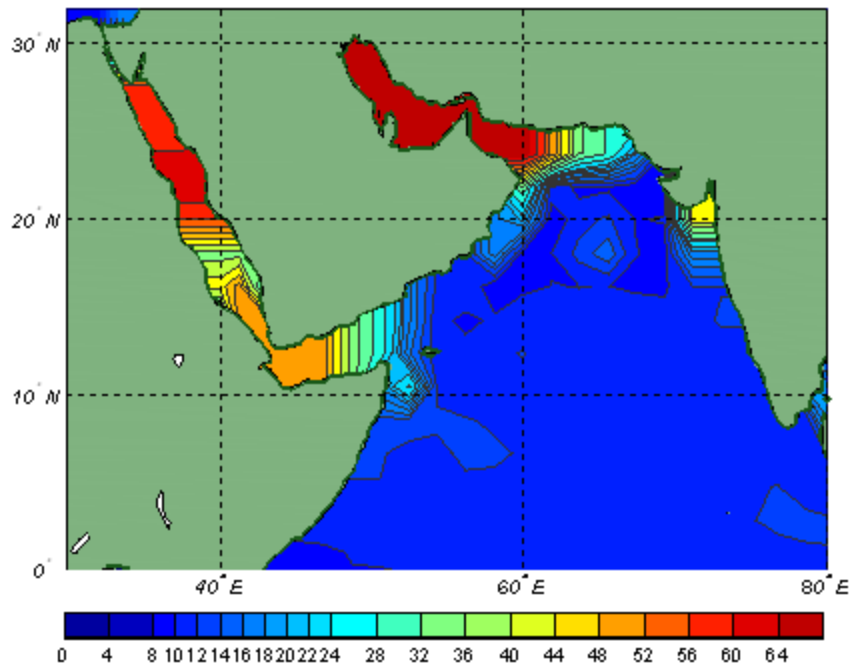


Figure 70. LTM EDH (m) for May for NW IO. Note coastal caution (Chapter III, section A).

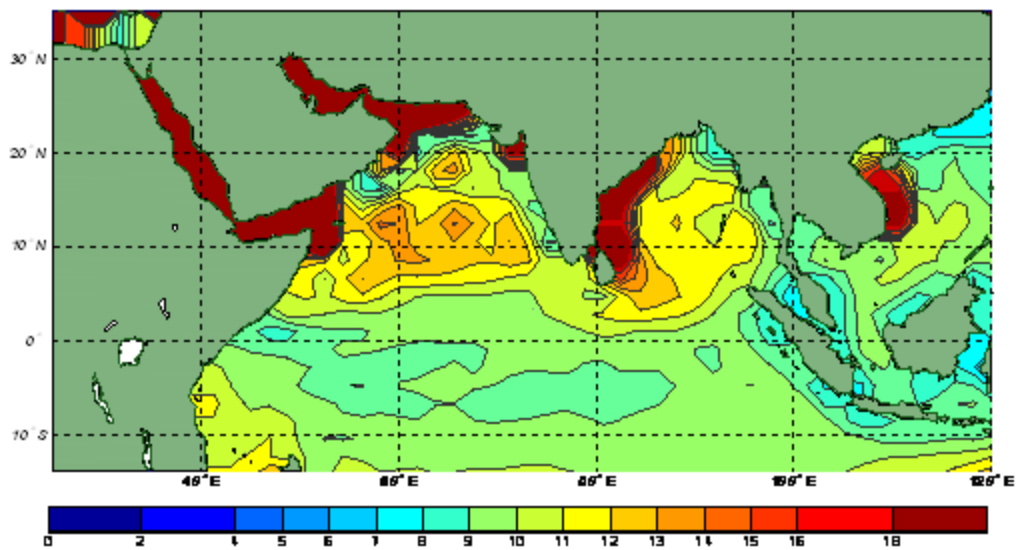


Figure 71. LTM EDH (m) for June. Note coastal caution (Chapter III, section A).

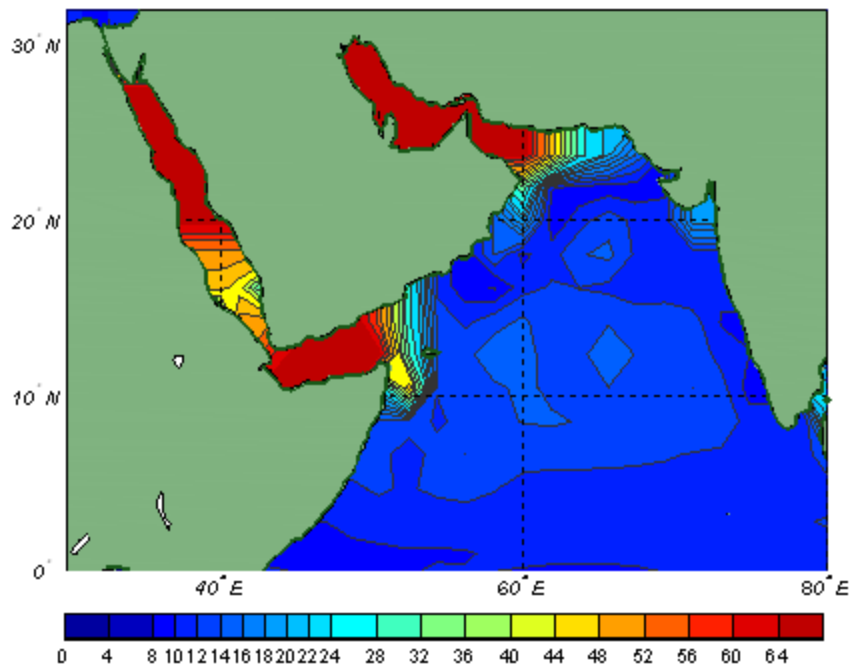


Figure 72. LTM EDH (m) for June for NW IO. Note coastal caution (Chapter III, section A).

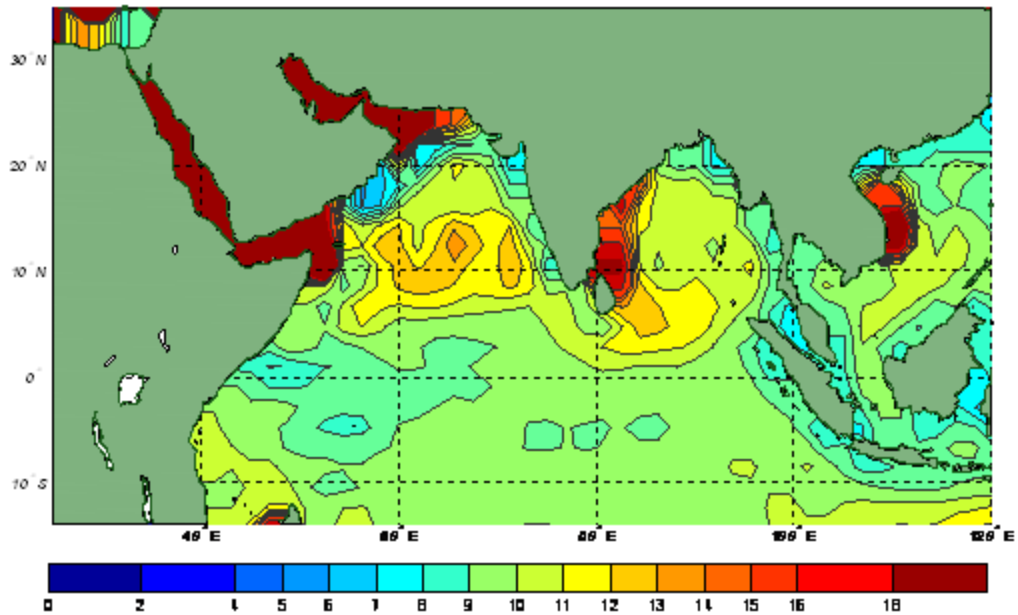


Figure 73. LTM EDH (m) for July. Note coastal caution (Chapter III, section A).

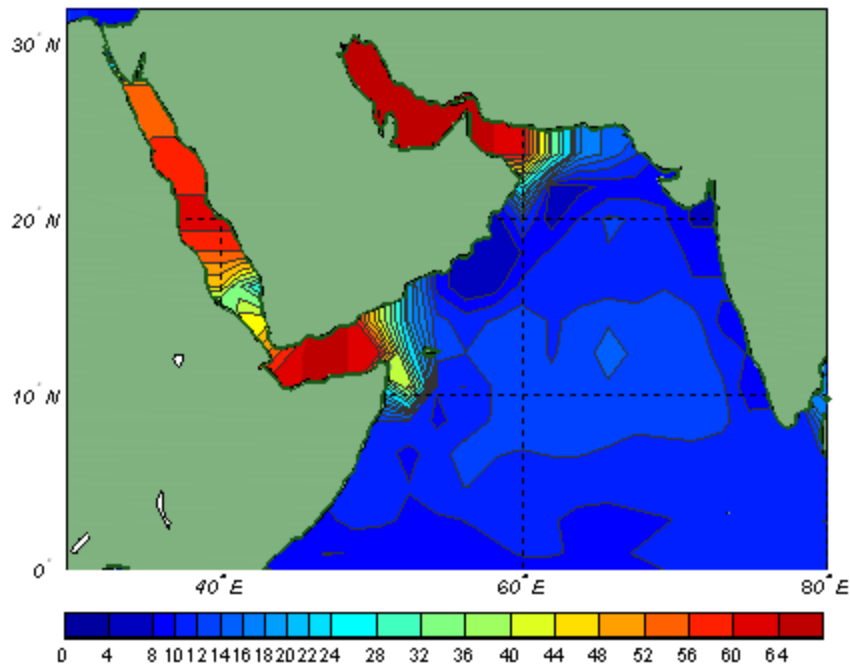


Figure 74. LTM EDH (m) for July for NW IO. Note coastal caution (Chapter III, section A).

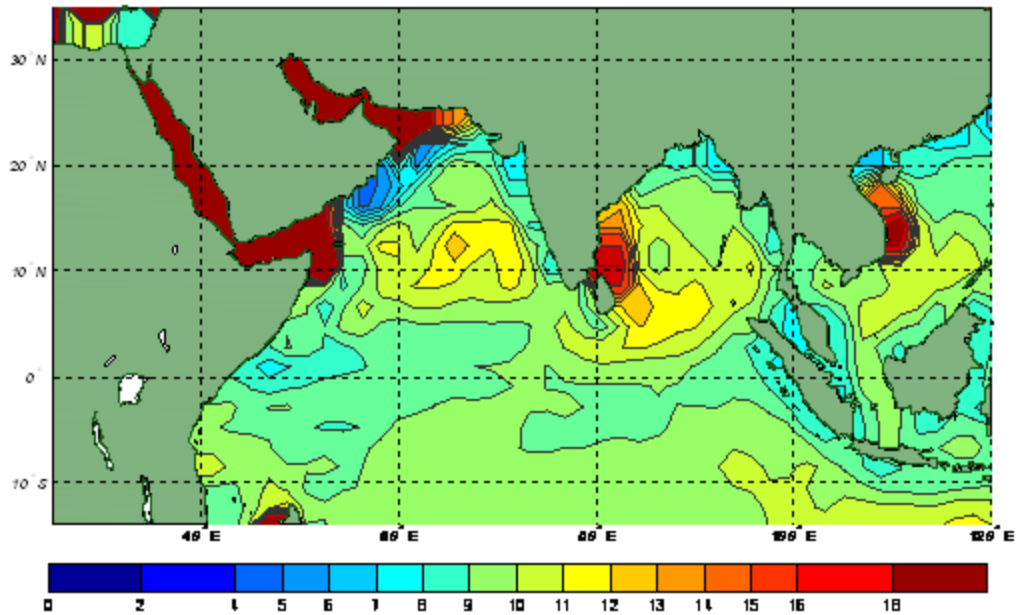


Figure 75. LTM EDH (m) for August. Note coastal caution (Chapter III, section A).

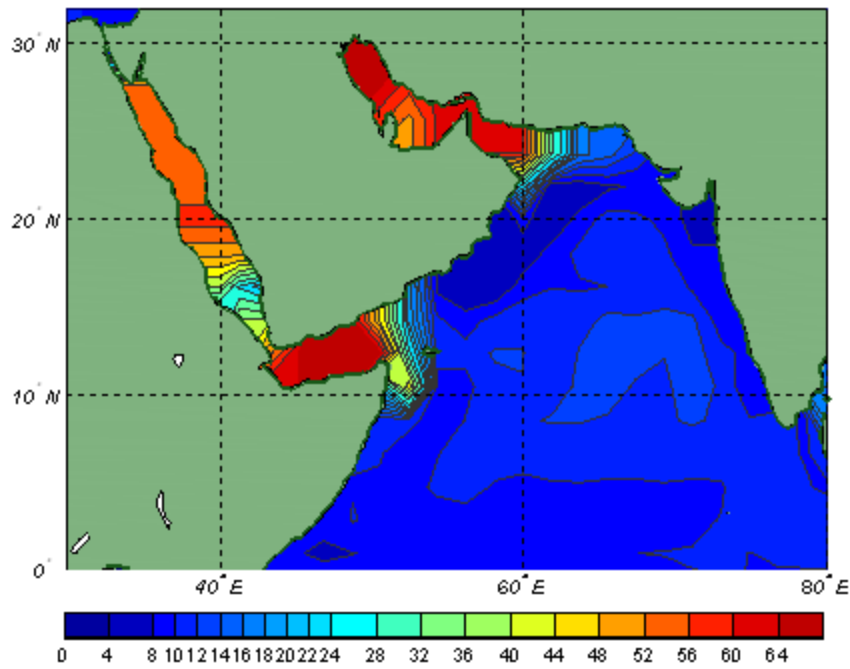


Figure 76. LTM EDH (m) for August for NW IO. Note coastal caution (Chapter III, section A).

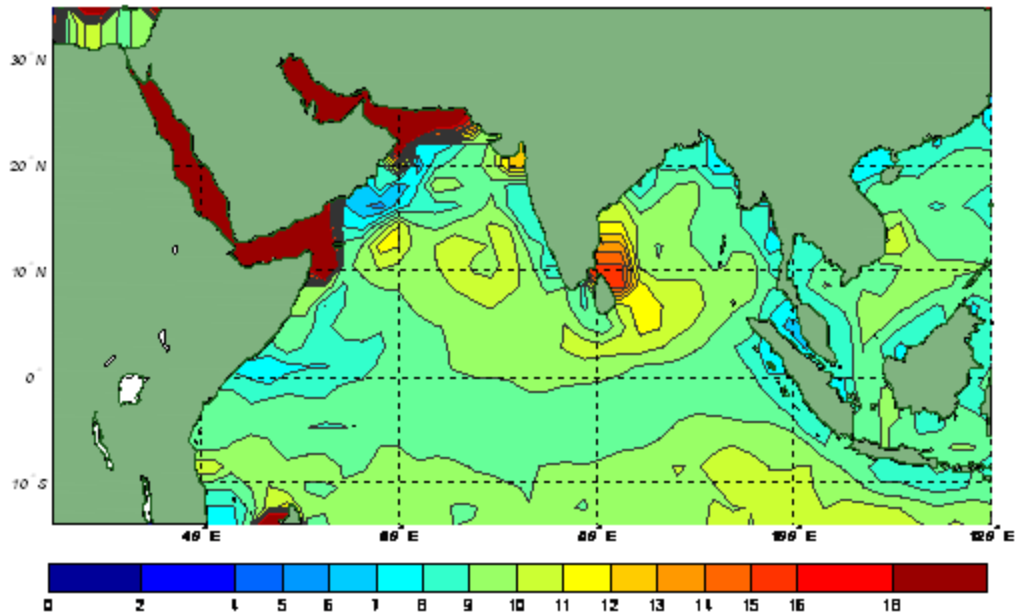


Figure 77. LTM EDH (m) for September. Note coastal caution (Chapter III, section A).

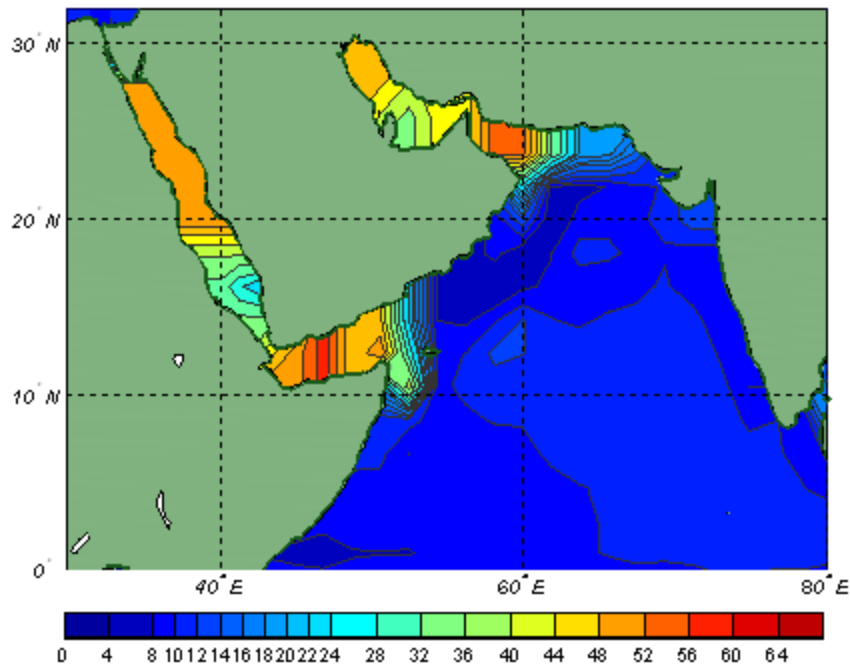


Figure 78. LTM EDH (m) for September for NW IO. Note coastal caution (Chapter III, section A).

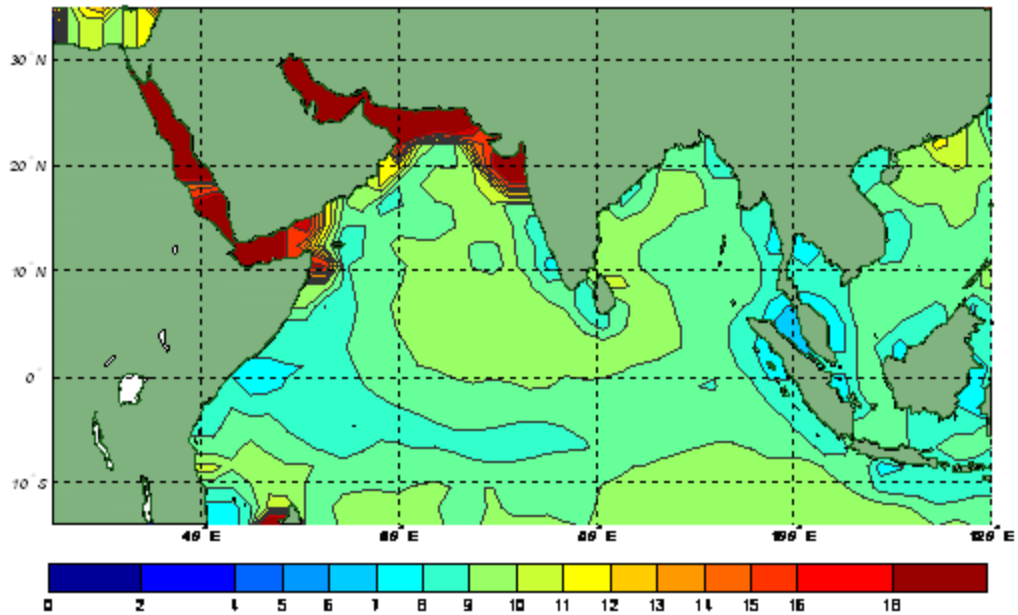


Figure 79. LTM EDH (m) for October. Note coastal caution (Chapter III, section A).

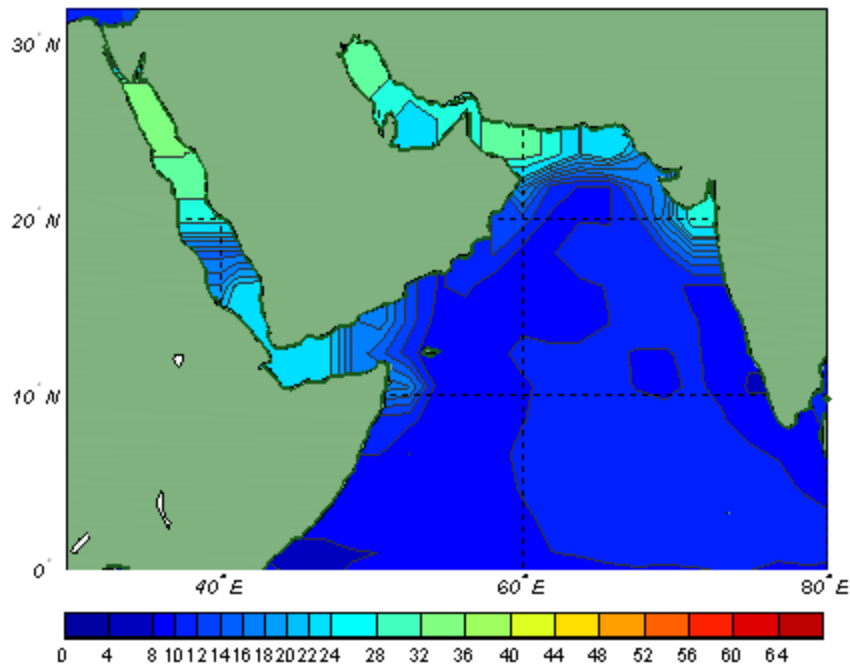


Figure 80. LTM EDH (m) for October for NW IO. Note coastal caution (Chapter III, section A).

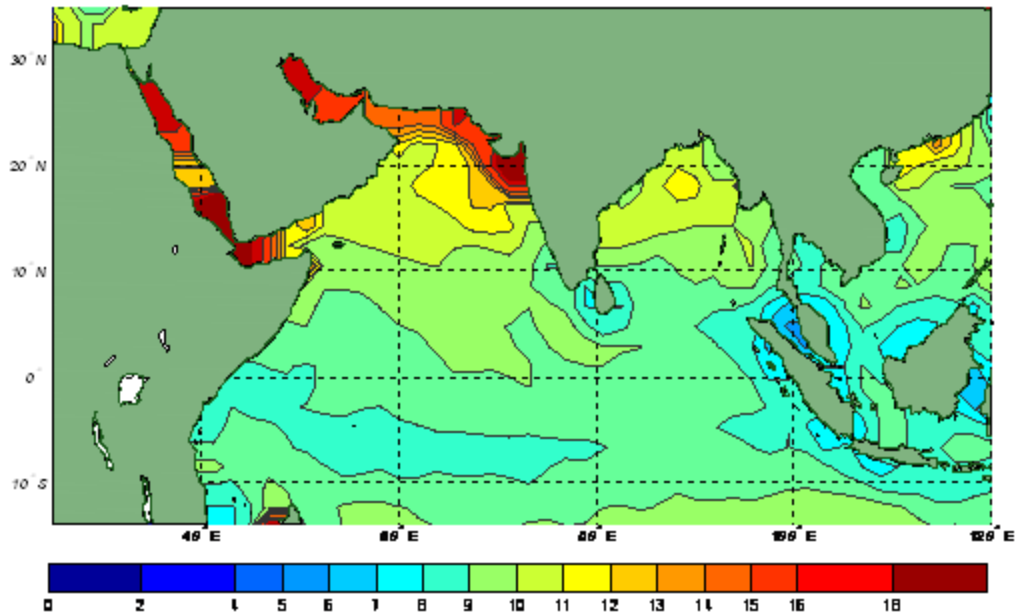


Figure 81. LTM EDH (m) for November. Note coastal caution (Chapter III, section A).

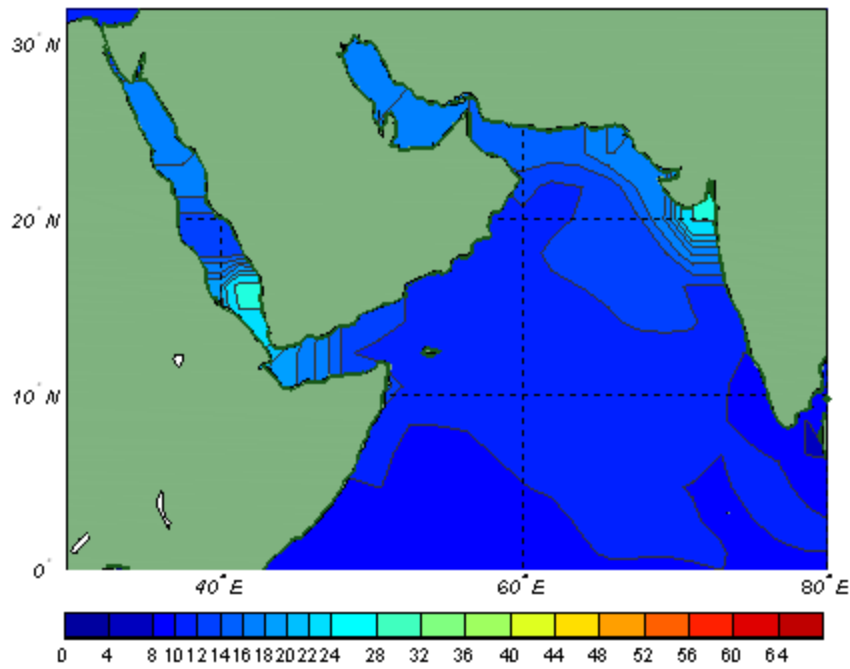


Figure 82. LTM EDH (m) for November for NW IO. Note coastal caution (Chapter III, section A).

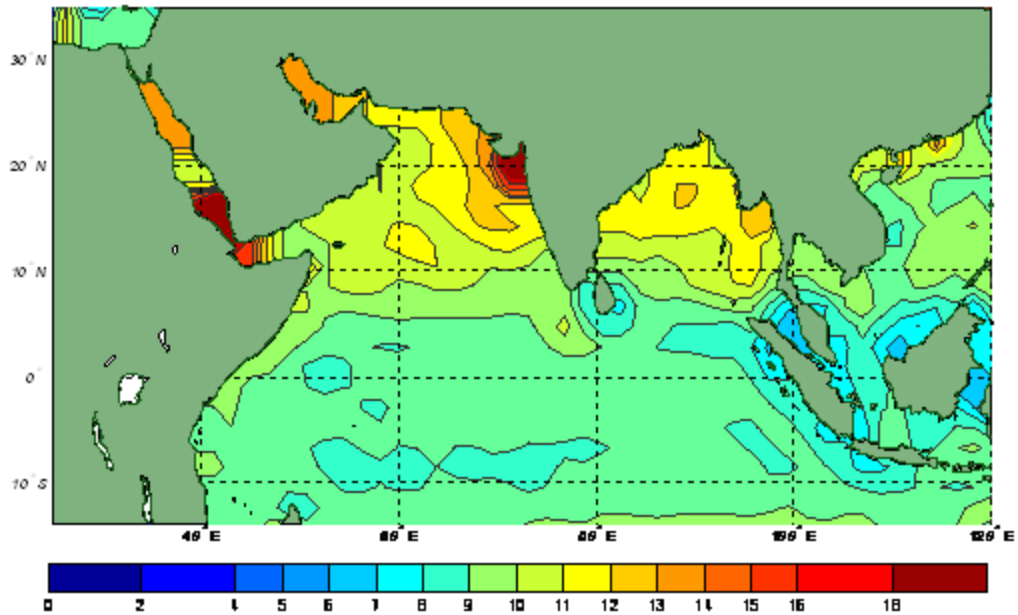


Figure 83. LTM EDH (m) for December. Note coastal caution (Chapter III, section A).

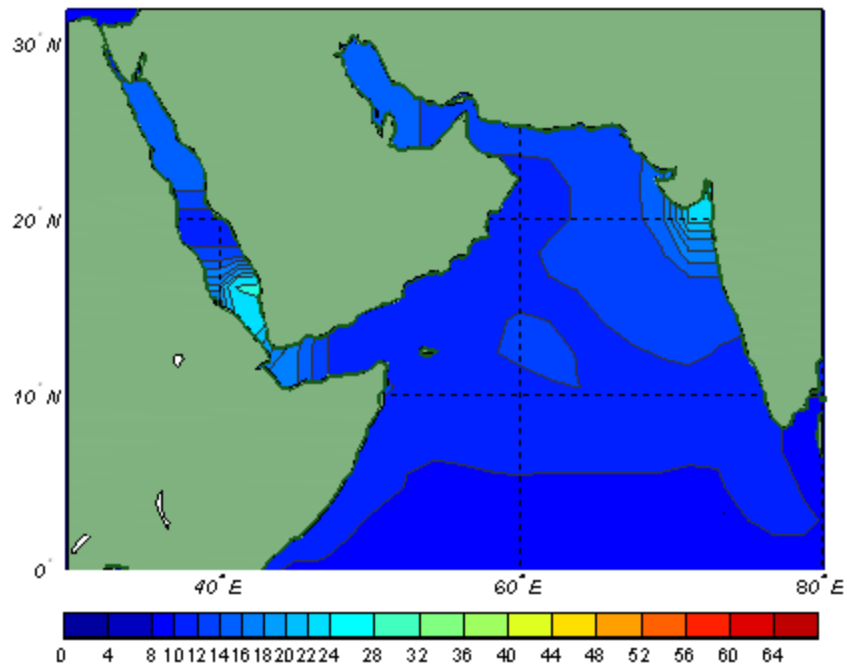


Figure 84. LTM EDH (m) for December for NW IO Note coastal caution (Chapter III, section A).

APPENDIX C.

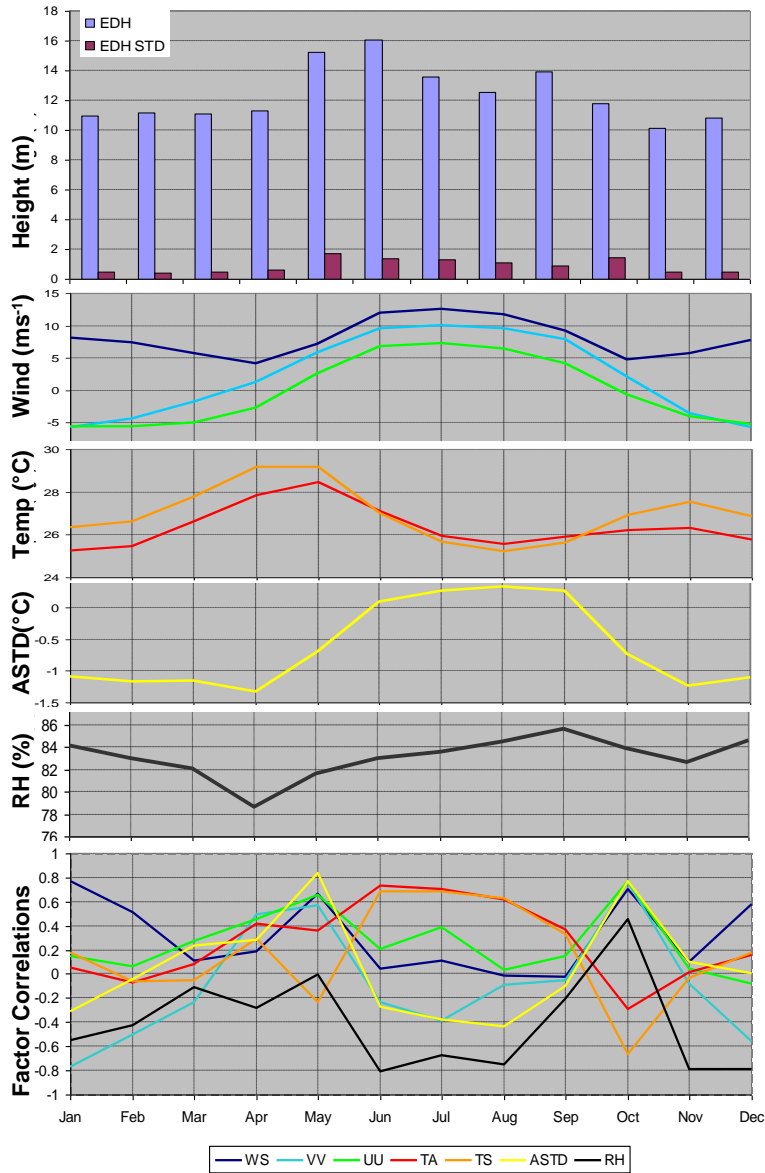


Figure 85. Seasonal cycle of monthly LTM EDH and EDH factor values (panels a-e) and correlations of EDH with EDH factors (panel f) for Somali Coast region (see Figure 20). (a) EDH and EDH standard deviation; (b) wind speed, u and v components of wind; (c) SST and Ta; (d) ASTD; (e) RH; (f) zero lag correlation for each month of EDH (panel a) with each of the factors (panels b-e), with the color of the correlation curves indicating the factor for which the correlation was calculated (see color code).

THIS PAGE INTENTIONALLY LEFT BLANK

LIST OF REFERENCES

- American Meteorological Society, Glossary of Meteorology, <http://amsglossary.allenpress.com/glossary> accessed September 2007.
- Ashok, K., Z. Guan, N. H. Saji, and T. Yamagata, 2004: Individual and Combined Influences of ENSO and the Indian Ocean Dipole on the Indian Summer Monsoon. *J.Clim.*, **17**, 3141-3155, doi:10.1175/1520-0442(2004)017(3141:IACIOE)2.0.CO;2.
- Ashok, K., Z. Guan, and T. Yamagata, 2003: A Look at the Relationship between the ENSO and the Indian Ocean Dipole. *J.Meteorol.Soc.Japan*, **81**, 41-56, doi:JST.JSTAGE/jmsj/81.41.
- Ashok, K., Z. Guan, and T. Yamagata, 2001: Impact of the Indian Ocean Dipole on the Relationship between the Indian Monsoon Rainfall and ENSO. *Geophys.Res.Lett.*, **28**, 4499-4502.
- Atkinson, B. W., M. Zhu, 2005: Radar-duct and boundary-layer characteristics over the area of The Gulf. *Q.J.R.Meteorol.Soc.*, **131**, 1923-1953.
- _____, 2006: Coastal effects on radar propagation in atmospheric ducting conditions. *Meteorol.Appl.*, **13**, 53-62, doi:10.1017/S1350482705001970.
- Babin, S. M., G. S. Young, and J. A. Carton, 1997: A new model of the oceanic evaporation duct. *Journal of Applied Meteorology, Boston, MA*, **36**, 193-204.
- Barnston, A. G., and R. E. Livezey, 1987: Classification, seasonality and persistence of low-frequency atmospheric circulation patterns. *Mon. Wea. Rev.*, **115**, 1083-1126.
- Behera, S. K., J. J. Luo, S. Masson, and S. A. Rao, 2006: A CGCM Study on the Interaction between IOD and ENSO. *Journal of Climate*, **19**, 1688.
- Chiang, J. C. H., A. H. Sobel, 2002: Tropical Tropospheric Temperature Variations Caused by ENSO and Their Influence on the Remote Tropical Climate. *J.Clim.*, **15**, 2616-2631, doi:10.1175/1520-0442(2002)015(2616:TTVCB)2.0.CO;2.
- Ford, B., 2000: *El Nino and La Nina events, and Tropical Cyclones: Impacts and Mechanisms*. Master's Thesis, Department of Meteorology, Naval Postgraduate School, 120 pp.

Frederickson, P. A., K. L. Davidson, and A. K. Goroch, 2000: *Operational bulk evaporation duct model for MORIAH, Version 1.2*. Naval Postgraduate School, 70 pp. (Available from P. A. Frederickson, Naval Postgraduate School, 589 Dyer Road, Monterey, CA 93943-5114).

Frederickson, P., K. Davidson, J. Stapleton, D. Shanklin, R. Wiss, T. Nguyen, E. Burgess III, C. Weeks, W. Thornton, and T. Brown, 2001: "Validation of AREPS Propagation Assessments Using Different Evaporation Duct Models," *Battlespace Atmospheric and Cloud Impacts on Military Operations (BACIMO 2001) Conference*, Fort Collins, Colorado, 10-12 July 2001. (Army Research Laboratory CD-ROM ARL-SR-01126, October 2001).

Frederickson, P. A., K. L. Davidson, K. D. Anderson, S. M. Doss-Hammel, and D. Tsintikidis, 2003: Air-sea interaction processes observed from buoy and propagation measurements during the RED Experiment. *Preprints, 12th Conf. on Interactions of the Sea and Atmosphere*, Long Beach, CA, Amer. Meteor. Soc., 9-13 February 2003 (83rd AMS Annual Meeting, Combined Preprints CD-ROM).

Frederickson, P.A. and K. L. Davidson, 2004: Brief: *Potential Propagation Products: Radar Detection of Small Surface & Low-Altitude Targets Workshop on Propagation in Littoral Circulations*, Naval Surface Warfare Center, Dahlgren Division (Available from P. A. Frederickson, Naval Postgraduate School, 589 Dyer Road, Monterey, CA 93943-5114).

Frederickson, P. A., 2007: Personal communication.

Geernaert, G. L., 2007: On the Evaporation Duct for Inhomogeneous Conditions in Coastal Regions. *Journal of Applied Meteorology and Climatology*, **46**, 538.

Gill, A. E., 1980: Some simple solutions for heat induced tropical circulation. *Q. J. Roy. Met. Soc.*, **106**, 447-462.

Gill, A. E., 1983: *Atmosphere-Ocean Dynamics*. International Geophysics Series, Academic Press, 662 pp.

Great Britain Ministry of Defence, 2004: *British Maritime Doctrine*. 3rd ed. Stationery Office Books, 323 pp.

Hanson, C. M., 2007: *Long-Range Operational Military Forecasts for Iraq*. Department of Meteorology, Naval Postgraduate School, Monterey, California.

Hildebrand, P., 2001: *El Nino and La Nina events and North Atlantic Tropical Cyclones*. Master's Thesis, Department of Meteorology, Naval Postgraduate School, 98 pp.

Hurrell, J. W., Y. Kushnir, G. Ottersen, and M. Visbeck, 2003: An overview of the North Atlantic Oscillation. The North Atlantic Oscillation: Climatic Significance and Environmental Impact. *Geophys. Monogr.*, **134**, Amer. Geophys. Union, 1-34.

LaJoie, M., 2006: *The impact of climate variations on military operations in the Horn of Africa*. M.S. Thesis, Dept. of Meteorology, Naval Postgraduate School, Joint Staff, 1999: Joint Publication 3-59: Joint Doctrine Tactics, Techniques, and Procedures for Meteorological and Oceanographic Support. U.S. Joint Chiefs of Staff, 23 March 99, 208 pp.

Kalnay, E., M. Kanamitsu, R. Kistler, W. Collins, D. Deaven, L. Gandin, M. Iredell, S. Saha, G. White, J. Woollen, Y. Zhu, M. Chelliah, W. Ebisuzaki, W. Higgins, J. Janowiak, K. C. Mo, C. Ropelewski, J. Wang, A. Leetmaa, R. Reynolds, R. Jenne, and D. Joseph, 1996: The NCEP/NCAR 40-year reanalysis project. *Bulletin of the American Meteorological Society, Boston, MA*, **77**, 437-471.

Krishnamurthy, V., B. P. Kirtman, 2003: Variability of the Indian Ocean: Relation to monsoon and ENSO. *Q.J.R.Meteorol.Soc.*, **129**, 1623-1646, doi:10.1256/qj.01.166.

Liebmann, Brant, and Catherine A. Smith, 1996: Description of a Complete (Interpolated) Outgoing Long wave Radiation Dataset. *Bulletin of the American Meteorological Society*, **77**, 1275-1277.

Loschnigg, J., G. A. Meehl, P. J. Webster, J. M. Arblaster, and G. P. Compo, 2003: The Asian Monsoon, the Tropospheric Biennial Oscillation, and the Indian Ocean Zonal Mode in the NCAR CSM. *J.Clim.*, **16**, 1617-1642, doi:10.1175/1520-0442(2003)016(1617:TAMTTB)2.0.CO;2.

Lutgens Frederick K., and E. J. Tarbuck, 2001: *The Atmosphere*. 8th edition. Prentice Hall; Upper Saddle River, New Jersey, 336 pp.

Madden, R. A., and P. R. Julian, 1994: Observations of the 40-50 day tropical oscillation: a review. *Mon. Wea. Rev.*, **122**, 814-837.

Matsuno, T. (1966): Quasi-Geostrophic Motions in the Equatorial Area: *J. Meteorol. Soc. Japan*, **44**, 1, 25-42.

McGee, T., 2006. *Battlespace on Demand: Commander's Intent*, Commander Naval Meteorology and Oceanography Command Memorandum, 14 pp.

Meyers, G., P. McIntosh, L. Pigot, and M. Pook, 2007: The Years of El Niño, La Niña, and Interactions with the Tropical Indian Ocean. *Journal of Climate*, **20**, 2872.

Moss, S. M., 2007: Long-Range Operational Military Forecasts for Afghanistan. Department of Meteorology, Naval Postgraduate School, Monterey, California.

Murphree, T., 2006a: *MR3610 Course Module 16: El Nino La Nina Southern Oscillation Part 1*. Department of Meteorology, Naval Postgraduate School, Monterey, California, 25 pp.

_____, 2006b: *MR3610 Course Module 22: North Atlantic Oscillation Arctic Oscillation*. Department of Meteorology, Naval Postgraduate School, Monterey, California, 42 pp.

_____, 2006c: *MR3610 Course Module 6: Smart Climatology: Concepts and Products*. Department of Meteorology, Naval Postgraduate School, Monterey, California, 46 pp.

_____, 2006d: *MR3610 Course Module 5: Introduction to Climate Science*. Department of Meteorology, Naval Postgraduate School, Monterey, California.

_____, 2007a: *Applications of Smart Climatology to Naval Warfare*. Department of Meteorology, Naval Postgraduate School, Monterey, California.
<http://wx.met.nps.navy.mil/smart-climo/reports.php> (accessed September 2007).

_____, 2007b: Personal communication.

_____ and Ford, B. W., 2007, *Smart Climatology for ASW: Initial Assessments and Recommendations*. Department of Meteorology, Naval Postgraduate School, Monterey, California, <http://wx.met.nps.navy.mil/smart-climo/reports.php> (accessed September 2007).

Patterson, W. L., 1987: Historical Electromagnetic Propagation Condition Database Description, Naval Oceans Systems Center, San Diego, California.
NOSC TD 1149.

Peixoto, J. P., and A. H. Oort, 1992: *Physics of Climate*. American Institute of Physics, New York, 520 pp.

Philander, G. S., 1990: *El Nino, La Nina, and the Southern Oscillation*. Academic Press, San Diego.

Ropelewski, F., and M. S. Halpert, 1987: Global and regional scale precipitation patterns associated with the El Niño/Southern Oscillation. *Mon. Wea. Rev.*, **115**, 1602-1626.

_____, and _____, 1989: Precipitation patterns associated with the high index phase of the Southern Oscillation. *J. Clim.*, **2**, No. 3, 268–284.

_____ and _____, 1995. Quantifying Southern Oscillation-Precipitation Relationships. *J. Clim.*, **9**, No. 5, pp. 1043–1059.

Reynolds, R. W., T. M. Smith, 1994: Improved Global Sea Surface Temperature Analyses Using Optimum Interpolation. *Journal of Climate*, **7**, 929-948.

Saji, N. H., B. N. Goswami, P. N. Vinayachandran, and T. Yamagata, 1999: A dipole mode in the tropical Indian Ocean. *Nature, London, England*, **401**, 360-363.

Saji, N. H., T. Yamagata, 2003: Possible impacts of Indian Ocean Dipole mode events on global climate. *Clim.Res.*, **25**, 151-169.

Sean Chamberlin, W., T. D. Dickey, 2007: *Exploring the world ocean*. McGraw-Hill Science/Engineering/Math, 394 pages pp.

Smith, T. M., R. W. Reynolds, 2003: Extended reconstruction of global sea surface temperatures based on COADS data (1854-1997). *Journal of Climate*, **16**, 1495.

Syed, F. S., F. Giorgi, J. S. Pal, and M. P. King, 2006: Effect of remote forcings on the winter precipitation of central southwest Asia part 1: observations. *Theoretical and Applied Climatology*, **86**, 147.

United Kingdom Hydrographic Office, 2007: *UK Handbook for AML*. 2nd ed. UK MOD Defence Intelligence, 72 pp.

Van den Dool, H., 2007. *Empirical Methods in Short-Term Climate Prediction*, Oxford University Press, 215 pp.

Vorhees, D., 2006. *The Impacts of Global Scale Climate Variations on Southwest Asia*. Master's Thesis, Department of Meteorology, Naval Postgraduate School.

Wainer, I., P. J. Webster, 1996: Monsoon/El Nino-Southern Oscillation relationships in a simple coupled ocean-atmosphere model. *Journal of Geophysical Research, Washington, DC*, **101**, 25599-25614.

Webster, P. J., V. O. Magana, T. N. Palmer, J. Shukla, R. A. Tomas, M. Yanai, and T. Yasunari, 1998: Monsoons: processes, predictability, and the prospects for prediction. *Journal of Geophysical Research, Washington, DC*, **103**, 14451-14510.

Webster, P. J., A. M. Moore, J. P. Loschnigg, and R. R. Leben, 1999: Coupled ocean-atmosphere dynamics in the Indian Ocean during 1997-98. *Nature, London, England*, **401**, 356-360.

Weller, R. A., M. F. Baumgartner, S. A. Josey, D. L. Frischer, and J. C. Kindle, 1998: Atmospheric forcing in the Arabian Sea during 1994-1996: observations and comparisons with climatology and models. *Deep-Sea Research (Part II, Topical Studies in Oceanography)*, **45**, 1961-1999.

Weller, R. A., A. S. Fischer, D. L. Rudnick, C. C. Eriksen, T. D. Dickey, J. Marra, C. Fox, and R. Leben, 2002: Moored observations of upper-ocean response to the monsoons in the Arabian Sea during 1994-1995. *Deep-Sea Res. (II Top. Stud. Oceanogr.)*, **49**, 2195-2230.

Wolter, K., 1987: The Southern Oscillation in surface circulation and climate over the tropical Atlantic, Eastern Pacific, and Indian Oceans as captured by cluster analysis. *J. Climate Appl. Meteor.*, **26**, 540-558.

Wolter, K., and M.S. Timlin, 1993: Monitoring ENSO in COADS with a seasonally adjusted principal component index. *Proc. of the 17th Climate Diagnostics Workshop*, Norman, OK, NOAA/N MC/CAC, NSSL, Oklahoma Clim. Survey, CIMMS and the School of Meteor., Univ. of Oklahoma, 52-57.

INITIAL DISTRIBUTION LIST

1. Defense Technical Information Center
Ft. Belvoir, Virginia
2. Dudley Knox Library
Naval Postgraduate School
Monterey, California
3. Physical Sciences Division: Data Management
Boulder, Colorado
4. Defence Intelligence, Intelligence Collection Strategy and Plans
MINISTRY OF DEFENCE
Northumberland Avenue, LONDON. WC2N 5BP
United Kingdom
5. Maritime Warfare Centre
Room F190, Marlborough Building
HMS COLLINGWOOD
Newgate Lane, FAREHAM
Hampshire PO14 1AS
United Kingdom
FAO: ESO TD
6. Dr. Tom Murphree
Meteorology Department, Code MR/Me
Naval Postgraduate School
Monterey, California
7. Mr. Paul Frederickson
Meteorology Department, Code MR/Fd
Naval Postgraduate School
Monterey, California